

Thesis

# Meson correlations and spectral functions in the deconfined phase

A systematic analysis in quenched lattice QCD

Marcel Müller

November 2013

Dissertation  
Fakultät für Physik  
Universität Bielefeld



# Contents

<b>Introduction and Motivation</b>	<b>11</b>
<b>1 Lattice QCD</b>	<b>17</b>
1.1 Path integrals and observables in QCD	17
1.2 Lattice gauge action	19
1.3 Lattice Fermion actions	20
1.3.1 The fermion doubler problem	20
1.3.2 Dealing with fermion doublers	21
1.3.3 The Wilson action and clover improvement	22
1.3.4 The staggered action	24
1.4 The partition function and the quenched approximation	25
1.4.1 The heat bath algorithm	26
1.4.2 Work flow of gauge configuration generation	26
1.5 Meson correlators	27
1.5.1 Inverting the fermion matrix	28
1.5.2 Meson correlators on the lattice	29
1.6 Spectral functions	31
1.7 Summary	32
<b>2 Parallel Lattice Code</b>	<b>33</b>
2.1 Starting point and general decisions	33
2.2 C++ as programming language and git for versioning	34
2.3 Modular and layered design	35
2.3.1 Fundamental data types on single sites and links	35
2.3.2 Lattice-wide containers	37
2.3.3 Memory layout management through the lattice class	38
2.3.4 Positions on and iterations over the lattice	40
2.3.5 Communication abstraction and parallelism	41
2.3.6 High level functions	42
2.4 Automated unit tests	43
2.5 Current state	46
2.6 Outlook, planned features	46
<b>3 Scale setting</b>	<b>49</b>
3.1 Determining lattice spacing	49
3.2 Critical temperature and temperature scale	50

## Contents

3.3	Setting the quark mass . . . . .	54
3.3.1	Quark masses for clover-improved Wilson fermions . . . . .	55
3.3.2	Quark masses for staggered fermions . . . . .	57
3.4	Non-perturbative renormalization for the vector current . . . . .	57
<b>4</b>	<b>Meson screening masses</b>	<b>59</b>
4.1	Extracting meson masses on finite size lattices . . . . .	59
4.1.1	Effective meson masses . . . . .	60
4.1.2	Masses extracted through a fit . . . . .	61
4.1.3	Extracting the ground state mass by fitting multiple states . . . . .	63
4.2	A study at $1.5 T_c$ and $3.0 T_c$ . . . . .	65
4.2.1	The thermodynamic limit . . . . .	67
4.2.2	Ground state extracted from multiple state fits on finite lattices . . . . .	68
4.2.3	The continuum limit . . . . .	71
4.2.4	Interchanging thermodynamic and continuum limit . . . . .	71
4.2.5	Results at $3.0 T_c$ . . . . .	73
4.3	Final results and conclusion . . . . .	73
<b>5</b>	<b>Thermal dilepton rates</b>	<b>79</b>
5.1	Heavy ion collisions and thermal dileptons . . . . .	79
5.2	Dilepton rates and the vector spectral function . . . . .	81
5.2.1	Bayesian techniques: Maximum entropy method . . . . .	82
5.2.2	Model-based ansatz . . . . .	83
5.3	Ansatz for the vector spectral function . . . . .	83
5.4	Setup of a temperature dependence study . . . . .	84
5.5	Continuum correlators from the lattice . . . . .	86
5.5.1	Ratios to free continuum and lattice correlators . . . . .	86
5.5.2	A summary of the extrapolation procedure . . . . .	88
5.5.3	Error estimate of the continuum extrapolation . . . . .	90
5.6	Spectral function fit procedure . . . . .	91
5.6.1	Thermal moments . . . . .	92
5.6.2	Systematic error estimates . . . . .	94
5.7	Fit of the spectral function ansatz . . . . .	94
5.7.1	Systematic error estimation . . . . .	99
5.7.2	Results . . . . .	99
5.7.3	Fit without thermal moments . . . . .	101
5.7.4	Modified ansatz for the spectral function . . . . .	101
5.8	Continuum extrapolated correlators at finite momenta . . . . .	103
5.8.1	A momentum-dependent spectral function . . . . .	103
5.8.2	Finite momentum correlators . . . . .	103
5.8.3	Continuum extrapolation at non-vanishing momentum . . . . .	104
5.9	Conclusion . . . . .	105

<b>6 Conclusion</b>	<b>111</b>
6.1 Parallel Lattice Code . . . . .	111
6.2 Scale setting . . . . .	111
6.3 Meson screening masses . . . . .	112
6.4 Thermal dilepton rates . . . . .	112
<b>Bibliography</b>	<b>115</b>
<b>Acknowledgements</b>	<b>121</b>
<b>Declaration of Originality / Eigenständigkeitserklärung</b>	<b>123</b>



# List of Figures

1	The QCD Phase diagram . . . . .	12
1.1	Visualisation of the plaquette . . . . .	19
1.2	Sketch of the fermion doubler problem . . . . .	21
1.3	The clover-term in one $\mu\nu$ -plane . . . . .	23
2.1	An illustrative snapshot of the git history . . . . .	36
2.2	Memory mapping of the cartesian indexer . . . . .	39
2.3	Memory mapping of the linear indexer . . . . .	40
2.4	A code fragment demonstrating the use of lattice iterators . . . . .	41
2.5	Schematic diagram of the initialization phase and main components . . . . .	43
2.6	Schematic diagram of the Wilson/clover fermion matrix inverter . . . . .	44
2.7	Schematic diagram of the quenched gauge configuration generation . . . . .	45
3.1	Lattice spacing: Plot of $\ln(r_0/a)$ against $\beta$ . . . . .	51
3.2	Lattice temperature: Plot of $T_c \cdot r_0$ against $(a/r_0)^2$ . . . . .	54
4.1	Effective PS screening masses, $1.5 T_c$ , $N_\tau = 16$ , different $N_\sigma$ . . . . .	61
4.2	Effective screening masses, $1.5 T_c$ , $64^3 \times 16$ , demonstrating the oscillation in staggered channels . . . . .	62
4.3	One-state fit of the V correlator, $1.5 T_c$ , $32^3 \times 16$ . . . . .	64
4.4	Two-state fit of the V correlator, $1.5 T_c$ , $64^3 \times 16$ . . . . .	65
4.5	Quark mass dependence of PS staggered screening masses . . . . .	66
4.6	Fit range dependence of PS screening masses, $1.5 T_c$ , $64^3 \times 16$ . . . . .	69
4.7	Thermodynamic limit of the PS, at $1.5 T_c$ . . . . .	70
4.8	Ground state of the PS found by two-state fits, at tcl . . . . .	70
4.9	Continuum extrapolation of PS, S, V, AV, at $1.5 T_c$ . . . . .	72
4.10	Interchanged thermodynamic and continuum limit for PS, at $1.5 T_c$ . . . . .	73
4.11	PS screening mass combined fits at $3.0 T_c$ . . . . .	74
4.12	Meson screening masses final dataset . . . . .	77
4.13	Sketch of the screening mass temperature dependence . . . . .	78
5.1	Sketch of heavy ion collision and dilepton production processes . . . . .	80
5.2	Direct photons at RHIC and LHC . . . . .	80
5.3	Dilepton rates measured by PHENIX and STAR . . . . .	81
5.4	Extrapolation $a \rightarrow 0$ of $G_V$ at diff. distances $\tau T$ , at $1.1 T_c$ . . . . .	87

List of Figures

5.5	$G_V(\tau T)/G_V^{\text{free,lat.}}(\tau T)$ and $G_{ii}(\tau T)/G_V^{\text{free,lat.}}(\tau T)$ , on finite lattices and continuum extrapolated . . . . .	89
5.6	Resampling error estimation of extrapolated correlators . . . . .	91
5.7	Midpoint subtracted correlator $\Delta_V(\tau T)$ at $1.1 T_c$ , $1.2 T_c$ . . . . .	93
5.8	Contributions to the SPF for diff. values of $\omega_0$ , $\delta_\omega$ , at $1.1 T_c$ . . . . .	95
5.9	Similarities of correlators that enter the $\rho_{ii}$ fit. . . . .	96
5.10	Spectral functions and correlators, $1.1 T_c$ and $1.2 T_c$ . . . . .	97
5.11	Spectral functions and correlators, at $1.4 T_c$ . . . . .	98
5.12	Example of spectral functions and correlators from bad fit . . . . .	98
5.13	SPF and dilepton rates as obtained from the fit . . . . .	100
5.14	Fit without thermal moments, $1.1 T_c$ . . . . .	102
5.15	Fit of the OPE modified spectral function ansatz, $1.1 T_c$ . . . . .	102
5.16	Leading order log Boltzmann calculation of the momentum-dependent spectral function . . . . .	105
5.17	Finite momentum $V_L$ and $V_T$ correlators . . . . .	106
5.18	$V_L$ and $V_T$ continuum extrapolation for different momenta . . . . .	107
5.19	Results for the electrical conductivity . . . . .	108

# List of Tables

1.1	Quantum numbers for correlation functions . . . . .	30
1.2	Quantum numbers associated with different staggered phase factors . . . . .	30
3.1	Summary of lattice spacings and temperatures . . . . .	53
3.2	Summary of Wilson quark masses . . . . .	55
3.3	Summary of staggered quark masses . . . . .	58
4.1	Screening mass simulation parameters at $1.5 T_c$ . . . . .	66
4.2	Screening mass simulation parameters at $3.0 T_c$ . . . . .	67
4.3	PS fit results for the $c$ parameter . . . . .	67
4.4	$1.5 T_c$ final extrapolation results . . . . .	75
4.5	$3.0 T_c$ final extrapolation results . . . . .	76
5.1	Thermal dilepton simulation parameters, $1.1 T_c$ and $1.2 T_c$ . . . . .	85
5.2	Thermal dilepton simulation parameters, $1.4 T_c$ . . . . .	85
5.3	Values of $G_{00} = \chi_q/T$ and $Z_V(\beta)$ , on finite lattices and in the continuum . . . . .	90
5.4	Results for the thermal moments . . . . .	93
5.5	Results for spectral function fit parameters $1.1 T_c$ . . . . .	100
5.6	Results for spectral function fit parameters $1.2 T_c$ . . . . .	101
5.7	Momenta $ p/T  =  \vec{k}  \cdot 2\pi \cdot N_\tau/N_\sigma$ accessible at $N_\sigma/N_\tau = 3$ . . . . .	104



# Introduction and Motivation

Quantum chromodynamics, QCD, is the theory of the strong interaction. To our current knowledge, the strong interaction is one of the fundamental forces in nature. It complements gravity and the electromagnetic and weak force, where the latter two are joined in the unified theory of electro-weak interaction.

Gell-Mann's eight-fold way[1] started out in 1961 as a phenomenological model to structure the large amount of new hadrons found in early high energy physics experiments. Over the next decade, Quantum Chromodynamics evolved from it, introducing the concept of quarks as the basic constituents of the hadrons, and later the color degrees of freedom.

Quantum Chromodynamics is a non-abelian  $SU(3)$  gauge theory, the elementary particles are called *quarks* and the gauge bosons that mediate their interaction are called *gluons*, which both carry color charge.

At low temperatures and densities, quarks are not found as free particles, but only in bound, colorless states, called hadrons. When separating two quarks, the force between them rises until the creation of a new quark-antiquark pair becomes energetically favoured. This property is called confinement and is – in nature – only observed for the strong interactions. Confinement is presumably tightly linked to the non-abelian structure of QCD, which allows for self-interaction between the gluons. However, a rigorous proof of confinement is outstanding and considered a Millennium Problem[2].

In the high energy limit, perturbative calculations are applicable. Here the  $\beta$ -function, which links the running coupling  $\alpha_s(E)$  of QCD to the energy scale  $E$  the theory is probed at, can be calculated and is found to be negative[3]. Thus, the coupling decreases with rising energy and the theory moves towards the free limit. This effect is called asymptotic freedom and in a way complements confinement.

## Phases of QCD

QCD shows a rich phase structure, one of the well-known sketches of the QCD phase diagram being given in fig. 1. The phase of quarks and gluons found at high temperatures is called the quark-gluon plasma, the phase of bound states is referred to as the hadronic phase. The details of the phase diagram are a broad subject of current research, with experimental studies and various theoretical techniques employed. For example, the nature of the phase transition or crossover is a matter of ongoing scientific study and discourse.

Experimentally, the transition from bound states to a deconfined quark gluon plasma (QGP) is achieved in heavy ion collisions. At present, two heavy ion colliders are in operation: The RHIC collider at BNL, with the experiments PHENIX and STAR attached,

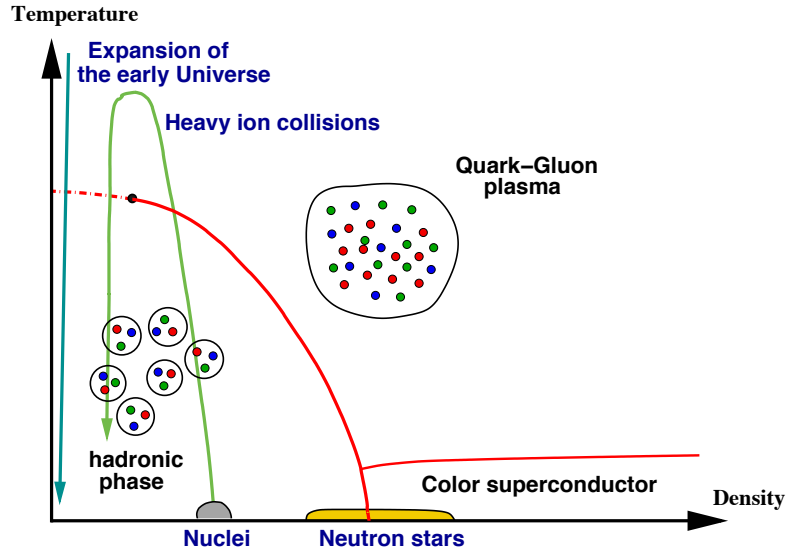


Figure 1: Sketch of the QCD phase diagram in temperature and chemical potential, cited from [4].

and the LHC collider at CERN. While the LHC is arguably most famous for its role in the Higgs search, which is predominantly conducted with proton - proton collisions, it is also used as a heavy ion collider with lead - lead collisions. The ALICE experiment at the LHC is specifically designed for the detection of heavy ion collisions. The dilepton measurements performed by these experiments are a main motivation for the thermal dilepton rate study presented in chapter 5, where an overview of the experimental status can be found.

For theoretical predictions from first principles, QCD calculations can be carried out in two ways: In the limit of high energy, analytical calculations are possible, as the small coupling allows for perturbative approaches. However, these approaches become invalid in the region of stronger couplings, when moving towards the confined phase. Here, lattice QCD is currently the only technique that allows to perform ab-initio calculations at zero and finite temperature.

## QCD on the lattice

In 1974, Kenneth G. Wilson introduced a space-time lattice as a regulator to find this non-perturbative approach to QCD[5]: Discretizing space-time to a lattice with a fixed, finite spacing between points regulates the UV-behaviour of the theory. Today lattice QCD arguably is the most successful non-perturbative approach to QCD.

The discretization introduced also quite naturally maps to a numerical implementation, by not only setting a fixed spacing between lattice points, but also setting a finite lattice extent. This effectively puts the system in a finite box, and directly yields a problem very accessible to numerical methods.

Care has to be taken when extracting physical observables from such a discretized theory in a finite volume: As a rough comparison, the systems studied in lattice QCD resemble a finite crystal structure, while nature offers a continuum of infinite size. The systematic errors introduced by this discretization thus have to be well understood and compensated for.

Lattice QCD calculation can be carried out at temperatures in the confined as well as in the deconfined phase, which makes them a very suited tool to study the QCD phase transition. As a caveat, the fermion sign problem limits these studies to vanishing chemical potential: For finite chemical potential, the Boltzmann-weight in the path integral becomes complex, the integrand starts to oscillate, and thus the Monte-Carlo techniques employed to solve the integral break down.

Finite temperature lattice QCD calculations focus on studying temperature-dependent effects in QCD and thus provide a powerful theoretical framework to study the phase transition. A comprehensive review of the current understanding and results obtained in the field can be found in [6].

## Outline of the work at hand

This work focuses on two lattice QCD studies that have been conducted over the last years: The thermodynamic and continuum limit of meson screening masses, and the determination of thermal dilepton rates from lattice QCD. The studies differ in their objectives, but share a lot of common means:

Both are carried out in the deconfined phase of QCD. Both use the quenched approximation, which greatly reduces the numerical effort, so large lattices are possible. This allows for small lattice spacings while maintaining large enough physical volumes. Most importantly, both rely on meson correlation functions as the main observable, which are extrapolated to the continuum limit, compensating lattice cut-off effects.

Another focus point in the course of this work is lattice QCD software development, which provides the tools and means to carry out the calculations.

A short motivation for each part follows here, while a more thorough introduction is provided in each corresponding chapter.

### Meson screening masses

The discretized version of the QCD action is not unique, and different actions with the correct continuum limit can be employed in the calculation. For the fermionic part of the action, this freedom of choice is widely used to find different compensations for the well-known fermion doubler problem.

Observables calculated on finite lattices are subject to discretization effects, stemming both from the finite lattice spacing and the finite lattice volume. Employing two popular fermion actions – the Wilson action with clover improvement and the standard staggered action – to calculate observables, it is known that the results obtained on finite lattices differ between both actions.

As the discretization effects between both actions may also differ, they might cause this deviation in the results. In this case, the differences must vanish when compensating for discretization effects by taking the thermodynamic (infinite lattice size) and continuum (zero lattice spacing) limit.

The study at hand sets out to answer this question. Full continuum results are obtained, allowing for the above mentioned comparison of both actions. Meson screening masses have been selected as a suitable observable for a systematic study of the discretization effects of clover-improved Wilson and standard staggered fermion, with thermodynamic and continuum limits carried out at two temperatures in the deconfined phase of QCD.

Meson screening also serves as an important observable for the study of the QCD phase transition, so the insight gained into the behavior of discretization effects is valuable for future studies, as it helps in finding more effective ways to obtain continuum extrapolations.

### Thermal dilepton rates

Thermal dileptons are produced in the QGP that is created in heavy ion collisions at RHIC and LHC. They serve as an important experimentally measured quantity to study the plasma. Most theoretical predictions for the rates of thermally produced dileptons and photons rely on input from truncated effective model calculations. In this work, a lattice QCD approach is used to carry out calculations close to the phase transition, where these effective models break down.

The study contributes to a long ongoing research effort. It uses an ansatz to extract the spectral function from lattice QCD observables that was developed as well as thoroughly tested and documented in a directly preceding work [7]. This work extends the above mentioned results by providing calculations at two more temperatures in the deconfined phase near the phase transition. A more detailed introduction, linking this research to current theoretical and experimental results, can be found at the beginning of the corresponding chapter 5 on thermal dilepton rates.

Preliminary results of this study have been presented in [8, 9].

### Software development

Lattice QCD simulations are numerical calculations that – historically and currently – require supercomputing resources and tailored software implementations. For some time the high and specific demand in computing power even drove the development of computing hardware that is specifically tailored to the demands of QCD simulations.

The adjoint software development is a very technical, but nonetheless important component in lattice QCD research. In the course of this work, a parallel lattice QCD software suite was developed, gradually replacing legacy codes with a structured, shared new code base. Of course, software development is a means to an end: It does not provide new scientific insight in itself, but enables or speeds up the research that has to

be performed. It is the equivalent of the machinery and tools an experimental physicist might have to design to be able to obtain measurements.

The software is currently in productive use for ongoing research projects and under constant, active development.

## **Structure of the thesis**

The layout of the thesis at hand is intended to represent the structure motivated above. A brief, general introduction to lattice QCD, motivating the concepts that are needed in this work, is given first. Another chapter lays out the scale setting calculations that were performed and which are a prerequisite for especially the dilepton study.

Three chapters follow, where each chapter focuses on one of the three main research matters laid out above. Each chapter features a short introduction, a discussion of the specific results and concluding remarks on its matter. This makes each chapter mostly self-contained, allowing them to be read independently of one another.

A conclusion that complements this introduction, providing a global summary of results and a general outlook, is given at the end.



# 1 Lattice QCD

The calculation of meson correlation functions in finite temperature quenched lattice QCD is the basis for all results presented in this work. In the following, an overview of the relevant theoretical foundation, quoting its fundamental equations and pointing to the numerical methods involved, is given. Introductions to lattice QCD are available in various textbooks[10, 11, 12]. This short overview especially follows the lecture notes of Gattringer/Lang [10], in employing the same notation for most quantities.

As a starting point, the path integral and QCD observables are discussed. Afterwards, the lattice discretization of fermion and gluon actions is laid out, introducing the two widely used fermion actions that are employed for this work. Finally, definitions of meson correlation functions on the lattice and their numerical implementation are given.

## 1.1 Path integrals and observables in QCD

The goal of lattice QCD calculations is to compute the thermal expectation value  $\langle \mathcal{O} \rangle$  of a physical observable  $\mathcal{O}$ . The most central is the QCD action  $S_{\text{QCD}}$ . Notations and conventions chosen here and in the following are heavily tailored towards a lattice discretization of the theory:  $S_{\text{QCD}}$  is given in euclidean metric, by working in euclidean space-time via  $t \rightarrow -i\tau$ . All subsequent equations are also assumed to be in euclidean time if not stated otherwise. The action splits into the gluonic part  $S_G$  and the fermionic part  $S_F$  of the interaction and reads

$$\begin{aligned} S_{\text{QCD}} &= S_F + S_G \\ S_F &= \int_0^{1/T} d\tau \int_V d^3\vec{x} \sum_{f=1}^{N_f} \bar{\psi}^{(f)}(x) D(x) \psi^{(f)}(x) \\ S_G &= -\frac{1}{2g^2} \int_0^{1/T} d\tau \int_V d^3\vec{x} \text{Tr}[F_{\mu\nu}(x)F_{\mu\nu}(x)]. \end{aligned} \quad (1.1)$$

The integral over space-time has been separated into its spatial component  $\int_V$  and the time direction  $\int_0^{1/T}$ . The time direction plays a distinct role in finite temperature calculations, as the temporal extent  $1/T$  in the integration sets the temperature of the system.

The quarks as massive fermions are given as Dirac 4-spinors

$$\psi^{(f)}(x)_{\alpha,c} \quad , \quad \bar{\psi}^{(f)}(x)_{\alpha,c} \quad (1.2)$$

and the gluonic fields  $A_\mu(x)$  define the field strength tensor

$$F_{\mu\nu}(x) = \partial_\mu A_\nu(x) - \partial_\nu A_\mu(x) + i[A_\mu(x), A_\nu(x)] \quad (1.3)$$

## 1 Lattice QCD

The  $x$  labels a space-time position, with  $x = (\vec{x}, t)$ , and the Dirac index is denoted by Greek letters as  $\alpha, \beta$ . The fermion fields carry an additional flavour index ( $f$ ), while the gluonic fields carry a Lorentz index  $\mu$  indicating their space-time direction.

In this commutator notation of the field strength tensor,  $A_\mu(x)$  are  $3 \times 3$  matrices generated by

$$A_\mu(x) = \frac{\lambda^a}{2} \mathcal{A}_\mu^a(x), \quad (1.4)$$

where  $\lambda^a$  are the Gell-Mann matrices and  $\mathcal{A}_\mu^a(x)$  for  $a = 1 \dots 8$  are real-valued fields, the color components. The non-vanishing commutator  $[A_\mu(x), A_\nu(x)]$  in eq. (1.3) gives rise to the gluon self-interaction, a prominent feature of the non-abelian nature of QCD.

The gauge coupling  $g$  is given as a global prefactor to the gauge action in eq. (1.1), by this convention and subsequent scaling of  $A_\mu(x)$ , it does not explicitly enter into, for example, the Dirac operator.

The full Dirac operator, denoted  $D(x)$  and including the covariant derivative, the  $\gamma$ -matrix contraction and the mass term, reads

$$D(x) = \sum_\mu (\gamma_\mu (\partial_\mu + iA_\mu(x)) + m) \quad (1.5)$$

Within the strong interaction of QCD, there is no coupling between the flavours, they only enter through different masses  $m^{(f)}$  and as a sum  $\sum^{N_f}$  in the action. Thus the flavour index is dropped for most of the following equations.

With  $A_\mu(x)$  entering into  $D(x)$ , the fermion action depends on the fermion fields  $\psi(x)$  as well as the gluonic fields. However, the gluonic part  $S_G$  of the action does not depend on the fermion fields. This becomes important for purely gluonic observables in so-called pure gauge calculations.

With the action in place, the partition function of QCD can be given by

$$Z(T, V) = \int \prod_\mu \mathcal{D}A_\mu \mathcal{D}\bar{\psi} \mathcal{D}\psi \exp(-S_{\text{QCD}}) \quad (1.6)$$

and the thermal expectation value of an observable  $\mathcal{O}$  can be calculated as

$$\langle \mathcal{O} \rangle = \frac{\int \prod_\mu \mathcal{D}A_\mu \mathcal{D}\bar{\psi} \mathcal{D}\psi \mathcal{O} \exp(-S_{\text{QCD}})}{Z(T, V)}. \quad (1.7)$$

With these preparations, discretized lattice versions of the actions in eq. (1.1) and the Monte-Carlo approach to solve eqs. (1.6) and (1.7) can be introduced in the following.

Space-time is discretised to a lattice with finite spacing  $a$ , where positions are denoted by vectors of integer numbers  $n$

$$n = (n_x, n_y, n_z, n_t) \quad (1.8)$$

so a position in physical units is found by

$$x = (n_x \cdot a, n_y \cdot a, n_z \cdot a, n_t \cdot a). \quad (1.9)$$

For finite size lattices, the spatial extent of the lattice is given by  $N_\sigma$ , the temporal extent is given by  $N_\tau$ , so

$$n_x, n_y, n_z \in [0, N_\sigma - 1] \quad n_t \in [0, N_\tau - 1]. \quad (1.10)$$

For isotropic lattices, the spacing  $a$  does not differ for the spatial and temporal direction. The temporal extent  $N_\tau \cdot a$  fixes the temperature of the system to  $T = \frac{1}{N_\tau \cdot a}$ .

## 1.2 Lattice gauge action

It is useful to discuss a discretized lattice version of the gluonic part  $S_G$  in the action  $S_{\text{QCD}}$  first, since it only depends on the gauge fields  $A_\mu(x)$  and not on the fermion fields.

The gauge fields  $A_\mu(x)$  are represented on the lattice as links  $U_\mu(x)$ , connecting a lattice site  $n$  to  $n + \hat{\mu}$ . Here  $\hat{\mu}$  is the unit vector in direction  $\mu$ , used to move between next-neighbour lattice sites. The links are defined as

$$U_\mu(n) = \mathcal{P} \exp \left( ia \int_{n \cdot a}^{(n+\hat{\mu}) \cdot a} dx A_\mu(x) \right) \quad (1.11)$$

where  $\mathcal{P}$  denotes the path ordering of the integral. The links  $U_\mu(n)$  are SU(3)-matrices, elements of the non-abelian SU(3) group, while  $A_\mu(x)$  are generators of these SU(3)-matrices. To reverse a link, so it connects  $n + \hat{\mu}$  to  $n$ , it is transposed and conjugated, so

$$U_{-\mu}(n + \hat{\mu}) = U_\mu^\dagger(n) = \mathcal{P} \exp \left( ia \int_{(n+\hat{\mu}) \cdot a}^{n \cdot a} dx A_\mu(x) \right) \quad (1.12)$$

Now an action  $S_G$  for the gauge fields, mapped to the lattice and thus constructed from the discrete set of link matrices  $U_\mu(n)$ , has to be found.

In general, given a closed path  $\mathcal{P}$  on the lattice, the trace over the product of link variables along such a path,

$$L_{\mathcal{P}}[U] = \text{Tr} \left[ \prod_{n, \mu \in \mathcal{P}} U_\mu(n) \right], \quad (1.13)$$

is a gauge-invariant object. Combinations of closed link loops can be used to construct gauge actions and also serve as important physical observables.

The most simple object is a closed loop of four links in two directions  $\mu, \nu$  with  $\mu \neq \nu$ . It is called the plaquette  $\square_{\mu\nu}$ , has an intuitive graphical representation (see fig. 1.1) and is given as

$$\begin{aligned} \square_{\mu\nu}(n) &= U_\mu(n) U_\nu(n + \hat{\mu}) U_{-\mu}(n + \hat{\mu} + \hat{\nu}) U_{-\nu}(n + \hat{\nu}) \\ &= U_\mu(n) U_\nu(n + \hat{\mu}) U_\mu^\dagger(n + \hat{\nu}) U_\nu^\dagger(n) \end{aligned} \quad (1.14)$$

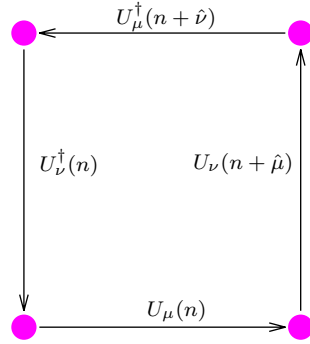


Figure 1.1: Visualisation of the plaquette used in eq. (1.14).

The plaquette is used in the construction of the first and arguably the simplest formulation of a lattice gauge action, the Wilson gauge action. It is used to discretize the field strength tensor from eq. (1.3), see also eq. (1.31) below, and with  $\beta = 6/g^2$  as the inverse coupling, the lattice action  $S_G[U]$  reads

$$\begin{aligned} S_G[U] &= \frac{\beta}{3} \sum_{n \in \Lambda} \sum_{\mu < \nu} \text{Re Tr} [\mathbb{1} - \square_{\mu\nu}(n)] \\ &= \frac{a^4}{2g^2} \sum_{n \in \Lambda} \sum_{\mu, \nu} \text{Tr} [F_{\mu\nu}(n)^2] + \mathcal{O}(a^6). \end{aligned} \quad (1.15)$$

### 1.3 Lattice Fermion actions

With a lattice formulation of the gauge action in place, now lattice discretizations of the fermion action  $S_F$  are discussed. In contrast to the gauge action, where –for this work– no modification or improvement of the Wilson gauge action is used, the choice of a fermion action is more involved:

Directly rewriting  $S_F$  in eq. (1.1), employing a symmetric first-order derivative for  $D_\mu(x)$  from eq. (1.5) and transforming  $A_\mu$  to link variables  $U_\mu(n)$  via eq. (1.11) yields the so-called naive discretization of the fermion action

$$S_F^{\text{naive}}[\psi, \bar{\psi}, U] = a^4 \sum_n \bar{\psi}(n) \left( \sum_{\mu=1}^4 \gamma_\mu \frac{U_\mu(n)\psi(n + \hat{\mu}) - U_{-\mu}(n)\psi(n - \hat{\mu})}{2} + m\psi(n) \right) \quad (1.16)$$

Note that in the free, non-interacting case the link variables become unit matrices and eq. (1.16) becomes

$$S_F^{\text{free}}[\psi, \bar{\psi}] = a^4 \sum_n \bar{\psi}(n) \left( \sum_{\mu=1}^4 \gamma_\mu \frac{\psi(n + \hat{\mu}) - \psi(n - \hat{\mu})}{2} + m\psi(n) \right) \quad (1.17)$$

#### 1.3.1 The fermion doubler problem

The main drawback of the naive fermion action is the well-known fermion doubler problem. In the notion of the lattice as a crystal structure, the doublers arise at the edges of the Brillouin zone. The naively discretized version of the Dirac operator in eq. (1.5), corresponding to the naive fermion action above, reads

$$D(n|m) = \sum_{\mu} (\gamma_\mu) \frac{U_\mu(n)\delta_{n+\hat{\mu}} - U_{-\mu}(n)\delta_{n-\hat{\mu}}}{2a} + m\delta_{m,n} \quad (1.18)$$

and, in the free case, found by setting  $U_\mu$  to unity matrices, becomes

$$D(n|m)^{\text{free}} = \sum_{\mu} (\gamma_\mu) \frac{\delta_{n+\hat{\mu}} - \delta_{n-\hat{\mu}}}{2a} + m\delta_{m,n} \quad (1.19)$$

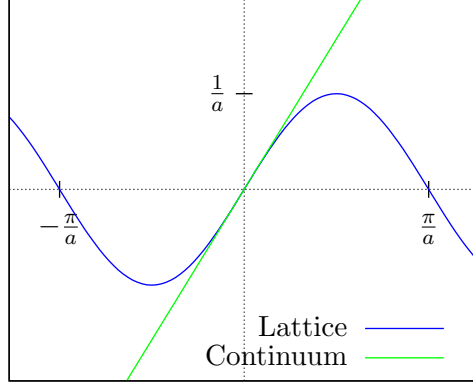


Figure 1.2: Sketch of the fermion doubler problem, massless lattice eq. (1.22) and continuum eq. (1.23) quark propagator contribution.

The lattice Fourier transformation of the free Dirac operator is given by

$$\tilde{D}(p|q) = \frac{1}{|\Lambda|} \sum_{n,m \in \Lambda} e^{-ip \cdot na} D(n|m) e^{iq \cdot ma} = \delta(p - q) \tilde{D}(p) \quad (1.20)$$

where

$$\tilde{D}(p) = m\mathbb{1} + \frac{i}{a} \sum_{\mu} \gamma_{\mu} \sin(p_{\mu}a). \quad (1.21)$$

The inverse, the so-called quark propagator, can be given in the free case as

$$\tilde{D}(p)^{-1} = \frac{m\mathbb{1} - ia^{-1} \sum_{\mu} \gamma_{\mu} \sin(p_{\mu}a)}{m^2 + a^{-2} \sum_{\mu} \sin(p_{\mu}a)^2}. \quad (1.22)$$

For the massless case  $m = 0$  the operator becomes

$$\tilde{D}(p)^{-1}|_{m=0} = \frac{-ia^{-1} \sum_{\mu} \gamma_{\mu} \sin(p_{\mu}a)}{a^{-2} \sum_{\mu} \sin(p_{\mu}a)^2} \quad (1.23)$$

This propagator has a pole for  $p = (0, 0, 0, 0)$  that corresponds to the fermion particle state in the continuum. On a lattice with finite spacing however, eq. (1.22) gives rise to additional poles at  $p = (\pi/a, 0, 0, 0)$ ,  $(0, \pi/a, 0, 0), \dots$ , introducing 15 additional, unphysical particle states, called fermion doublers.

### 1.3.2 Dealing with fermion doublers

The fermion doubler problem arises in the naive discretization of the fermion action. Since the action can be varied as long as the correct continuum limit  $a \rightarrow 0$  is maintained,

different modifications of the action can be used to tackle the doubler problem. However no complete solution is possible: The so-called No-Go theorem [13] proves that, under a set of assumptions that generally holds for lattice QCD formulations, an action either has to give rise to some kind of fermion doublers or it has to explicitly break the chiral symmetry  $\{D, \gamma_5\} = 0$ .

The two widely used actions employed in this thesis also have different effects on the doublers: The Wilson fermion action avoids doublers completely, thus breaking chiral symmetry. The staggered action reduces the doublers from 16 to 4, keeping a residual  $U(1)$  chiral symmetry.

### 1.3.3 The Wilson action and clover improvement

The Wilson fermion action is a quite direct approach to the doubler problem. An additional term, the so-called Wilson term, is introduced into the action to remove all unphysical poles in (1.22). The term resembles a mass, thus it breaks chiral symmetry explicitly. The term enters into the free Dirac operator in momentum space

$$\tilde{D}_{\text{Wilson}}^{\text{free}}(p) = m\mathbb{1} + \frac{i}{a} \sum_{\mu} \gamma_{\mu} \sin(p_{\mu}a) + \underbrace{\mathbb{1} \frac{1}{a} \sum_{\mu} (1 - \cos(p_{\mu}a))}_{\text{Wilson term}} \quad (1.24)$$

The operator is transformed back and interactions are reintroduced, so

$$D_{\text{Wilson}}(n|m) = \left(m + \frac{4}{a}\right) \delta_{n,m} - \frac{1}{2a} \sum_{\pm\mu} (\mathbb{1} - \gamma_{\mu}) U_{\mu}(n) \delta_{n+\hat{\mu},m} \quad (1.25)$$

which defines the Wilson fermion action as

$$\begin{aligned} S_F^{\text{Wilson}}[\psi, \bar{\psi}, U] &= a^4 \sum_{n,m} \bar{\psi}(n) D_{\text{Wilson}}(n|m) \psi(m) \\ &= a^4 \sum_n \bar{\psi}(n) \left[ \left(m + \frac{4}{a}\right) \psi(n) \right. \\ &\quad \left. - \frac{1}{2a} \sum_{\mu} [(\mathbb{1} - \gamma_{\mu}) U_{\mu}(n) \psi(n + \hat{\mu}) + (\mathbb{1} + \gamma_{\mu}) U_{-\mu}(n) \psi(n - \hat{\mu})] \right] \end{aligned} \quad (1.26)$$

Setting  $\psi' = \sqrt{m + 4/a} \psi$  and introducing the hopping parameter  $\kappa = 1/(2m \cdot a + 8)$  the action is rewritten to the final form

$$\begin{aligned} S_F^{\text{Wilson}}[\psi', \bar{\psi}', U] &= a^4 \sum_n [\bar{\psi}'(n) \psi'(n)] \quad (1.27) \\ &\quad - \kappa \sum_{\mu} \bar{\psi}'(n) [(\mathbb{1} - \gamma_{\mu}) U_{\mu}(n) \psi'(n + \hat{\mu}) + (\mathbb{1} + \gamma_{\mu}) U_{-\mu}(n) \psi'(n - \hat{\mu})] \end{aligned} \quad (1.28)$$

Aside from breaking chiral symmetry the Wilson action has another drawback: Discretization errors introduced by the finite lattice spacing  $a$  scale with leading order  $O(a^2)$

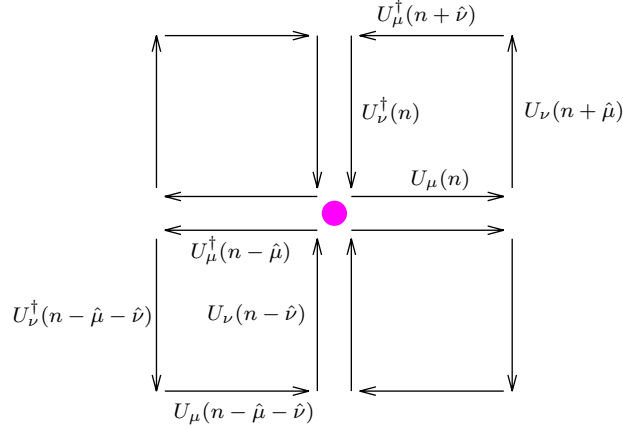


Figure 1.3: The clover-term in one  $\mu\nu$ -plane, made up from four plaquettes.

for the naive fermion action. The additional Wilson term introduces errors of  $O(a)$  into the action, so the leading order discretization effects become linear instead of quadratic in the lattice spacing.

While breaking chiral symmetry is inevitable, the discretization errors can be compensated for. For this purpose, the action in eq. (1.28) is complemented by a term compensating the  $O(a)$  effects

$$S^{\text{Wilson, clover}} = S^{\text{Wilson}} + c_{\text{SW}} a^5 \sum_{n \in \Lambda} \sum_{\mu < \nu} \bar{\psi}(n) \frac{1}{2} \sigma_{\mu\nu} F_{\mu\nu}(n) \psi(n). \quad (1.29)$$

Here a discretized lattice version of the field strength tensor is needed, which is found by introducing a sum of plaquettes, see eq. (1.14), as

$$Q_{\mu\nu}(n) = \square_{\mu,\nu}(n) + \square_{-\mu,\nu}(n) + \square_{\mu,-\nu}(n) + \square_{-\mu,-\nu}(n) \quad (1.30)$$

and

$$F_{\mu\nu} = \frac{-i}{8a^2} (Q_{\mu\nu}(n) - Q_{\nu\mu}(n)) \quad (1.31)$$

Since a graphical representation of the term  $Q_{\mu\nu}(n)$ , see fig. 1.3, resembles a four-leaf clover, the term is referred to as *clover-term* and the full action is usually denoted *clover-improved Wilson action*.

The index in  $c_{\text{SW}}$  refers to *Sheikholeslami-Wohlert*[14] and the coefficient can be tuned:  $c = 1$  yields leading order  $O(ag^2)$  discretization effects,  $c$  obtained from perturbative approaches will yield  $O(ag^n)$ , where  $n$  depends on the order of perturbation theory, and non-perturbative calculations can give  $O(a^2)$ . In this work,  $c_{\text{SW}}$  is set by the fully non-perturbative results for quenched QCD [15], parameterized in terms of the coupling as

$$c_{\text{SW}} = \frac{1 - 0.656 g^2 - 0.152 g^4 - 0.054 g^6}{1 - 0.922 g^2} \quad \text{with } 0 \leq g \leq 1. \quad (1.32)$$

### 1.3.4 The staggered action

Staggered fermions, or Kogut-Susskind fermions, are another widely used approach to the doubling problem. The 16-fold degeneracy of the naive action is reduced to four quarks, allowing a remnant of the chiral symmetry to be maintained.

This is achieved by decoupling next-neighbour interactions, introducing a lattice structure mixing spinor and space-time indices. The naive action (1.16) is transformed to a new set of field variables  $\psi'$

$$\psi(n) = \gamma_1^{n_x} \gamma_2^{n_y} \gamma_3^{n_z} \gamma_4^{n_t} \psi(n)' \quad \bar{\psi}(n) = \bar{\psi}(n)' \gamma_1^{n_x} \gamma_2^{n_y} \gamma_3^{n_z} \gamma_4^{n_t} \quad (1.33)$$

where each  $\gamma$ -matrix is raised to an integer power given by the position  $n$ . Rewriting the action in terms of  $\psi'$  and  $\bar{\psi}'$ , it becomes

$$\begin{aligned} S_F^{\text{stagg.}}[\psi, \bar{\psi}, U] &= a^4 \sum_{n,m} \bar{\psi}(n) D_{\text{stagg.}}(n|m) \psi(m) \\ &= a^4 \sum_{n \in \Lambda} \bar{\psi}(n)' \mathbb{1} \left( m \psi(n)' \right. \\ &\quad \left. + \sum_{\mu} \eta_{\mu}(n) \frac{U_{\mu}(n) \psi(n + \hat{\mu})' - U_{\mu}^{\dagger}(n - \hat{\mu}) \psi(n - \hat{\mu})'}{2a} \right) \end{aligned} \quad (1.34)$$

where the staggered sign functions, which set the staggered phases, are given by

$$\eta_1(n) = 1, \quad \eta_2(n) = (-1)^{n_x}, \quad \eta_3(n) = (-1)^{n_x + n_y}, \quad \eta_4(n) = (-1)^{n_x + n_y + n_z} \quad (1.35)$$

Since the action is diagonal in Dirac-space, only one of the now identical four components of  $\psi'(n)$  is kept and denoted, by convention,  $\chi(n)$ . For completeness and later reference, the staggered action then reads

$$\begin{aligned} S_F[\chi, \bar{\chi}, U] &= a^4 \sum_{n \in \Lambda} \bar{\chi}(n) \left( m \chi(n) \right. \\ &\quad \left. + \sum_{\nu} \eta_{\nu}(n) \frac{U_{\nu} \chi(n + \hat{\nu}) - U_{\nu}^{\dagger}(n - \hat{\nu}) \chi(n - \hat{\nu})}{2a} \right) \end{aligned} \quad (1.36)$$

To demonstrate that chiral symmetry is partially preserved by the staggered fermion action, it is useful to take a look at the bilinear  $\bar{\psi}(n) \gamma_5 \psi(n)$  that represents the pseudo-scalar. For the staggered action, it transforms to  $\eta_5(n) \bar{\chi}(n) \mathbb{1} \chi(n)$  where  $\eta_5(n) = (-1)^{n_x + n_y + n_z + n_t}$  gives the corresponding phase. Here

$$\chi(n) \rightarrow e^{i\alpha\eta_5(n)} \chi(n) \quad \bar{\chi}(n) \rightarrow \bar{\chi}(n) e^{i\alpha\eta_5(n)}$$

can be found as the remnant  $U(1)$  symmetry. The staggered actions shows leading order discretization effects  $O(a^2)$ . Thus with the non-perturbative clover-improvement for the Wilson action discussed above, both actions used in this work share the same leading order of discretization effects.

## 1.4 The partition function and the quenched approximation

A lattice version of the partition function can be obtained by using the lattice gauge and a lattice fermion action in eq. (1.6), which yields a partition function  $Z(U, \bar{\psi}, \psi)$  that formally depends on the fermion fields. However, as the fermion actions are bilinear, the fields can be integrated out.

As Grassmann valued fields, the fermionic part of the partition function is then given by

$$\int \mathcal{D}\bar{\psi}\mathcal{D}\psi \exp\left(\sum_{n,m} \bar{\psi}(n)D(n|m)\psi(m)\right) = \det[D] \quad (1.37)$$

which in turn allows to write the partition function as

$$Z_{\text{QCD}}(U) = \int \mathcal{D}U \det[D(U)] \exp(-S_G(U)). \quad (1.38)$$

Seen as a matrix,  $D$  is sparsely populated. Its structure is defined by the derivatives in the fermion action and the matrix coefficients are given by the gauge field  $U_\mu(n)$ . Numerically evaluating  $\det[D]$  directly is prohibitively expensive. The so-called quenched approximation is used to avoid calculating  $\det[D]$ , by setting  $\det[D] = 1$ . It is found by introducing a hopping parameter  $\kappa$ , rewriting  $D$  as  $D'(n|m) = \mathbb{1} - \kappa D(n, m)$ , see e.g. eqs. (1.26) and (1.28), and taking the limit  $\kappa \rightarrow 0$ .

The physical effect of this simplification is that the quark mass, linked to the hopping parameter as  $m \sim \frac{1}{\kappa \cdot a}$ , is sent to infinity. Thus, the Dirac sea quarks become infinitely heavy. In principle, the errors introduced by the quenched approximation are uncontrolled systematic errors. For the relevant observables in this work, the meson correlation functions with light quark masses, it has however been shown that the systematic errors of the quenched approximation are below 5% to 10% [16].

The partition function in the quenched approximation reads

$$Z_{\text{QCD}}^{\text{quenched}}(U) = \int \mathcal{D}U \exp(-S_G(U)). \quad (1.39)$$

so now only the gauge action  $S_G$  has to be taken into account for  $Z_{\text{QCD}}^{\text{quenched}}$ . To evaluate a high dimensional integral as in eq. (1.39), a Monte-Carlo approach is the only viable option: In general, a set of random gauge configuration  $U_\mu(n)$  would be generated and their weight  $\exp(-S_G(U))$  summed up. However, using fully random, evenly distributed configurations would be highly inefficient, as most of them would have a very low weight  $\exp(-S_G(U))$ .

### 1.4.1 The heat bath algorithm

A Markov-chain process is used to make this process efficient. It starts from an initial configuration, e.g. a random set of links (zero temperature) or a set of unit matrices (infinite temperature). In each step of the process, a new set of links, a new configuration is generated. The process ensures that the distribution of these configurations follows the probability weight given by  $\exp(-S_G(U))$ . As a Markov-chain process, two additional important properties are ensured: Firstly, each configuration  $U_\mu(n)$  with  $\exp(-S_G(U)) > 0$  will eventually be reached by the process, even if it takes an unfeasible high number of iterations for configurations with  $\exp(-S_G(U)) \gtrsim 0$ . Secondly, the process only needs a fixed, finite number of previous configurations to work, usually only the last configuration. It should be kept in mind that a Markov-chain process inevitably produces correlated configurations.

For this work, the heatbath algorithm[17, 18] is used to generate gauge configurations, with an additional improvement through intermediate overrelaxation[19, 20] steps. The heatbath itself changes the action  $S_G(U)$  of a configuration, implementing the importance sampling. The overrelaxation steps leave  $S_G(U)$  invariant, but gauge transforms the links so they move to a different position in configuration space. Overrelaxation greatly reduces the correlation between configurations. All configurations used in this work are separated by 500 heatbath updates, with 4 overrelaxation steps per heatbath update.

### 1.4.2 Work flow of gauge configuration generation

To set up the generation of new gauge configurations, a few parameters have to be set: The coupling  $\beta$  fixes the lattice spacing  $a$ , together with the temporal extent  $N_\tau$  the temperature of the system is set as  $1/T = a \cdot N_\tau$ . In chapter 3, it is laid out how these parameters can be related to a physical scale. The lattice volume  $N_\sigma$  is also set, and fixes the spatial volume of the lattice as  $V_{\text{phys.}}^{(3)} = (N_\sigma \cdot a)^3$ . Depending on the specific Markov-chain algorithm, further parameters can or have to be tuned. For the heat bath, the number of heat bath updates separating two configurations has to be set. If overrelaxation is used, also the number of overrelaxation steps per heat bath update has to be fixed. The configurations used in this work have been generated with 400 to 500 heat bath updates per configuration, 4 overrelaxation steps per heat bath update. For temperatures in the deconfined phase, this choice is found to be high enough to suppress autocorrelations, tested for e.g. the vector current correlator in [7].

When the heat bath algorithm is initially started, it also needs a way to initialize the first gauge configuration, where links are either set randomly (corresponding to a low temperature) or set to unit matrices (corresponding to infinite temperature). As a side note, this initialization is opposite to the one needed when simulating spin system, where an ordered configuration ensures a cold start. As Markov chain methods are often introduced by their application in spin system like the Ising model, this often leads to some confusion. When writing codes or documenting results, it is advisable to always state if a configuration is random or ordered, instead of only referring to the temperature

limit.

Starting from a freshly initialized gauge configuration, a certain amount of configuration updates is needed to thermalize the system. These configurations do not enter into the importance sampling, but are discarded. For configurations in the deconfined phase as used in this work, it is found that 5000 heat bath updates ensure a thermalized configuration.

Without modifying the process, the generation of gauge configurations is a serial<sup>1</sup> process: To start the calculation of configuration  $m$ , configuration  $m - 1$  has to be finished first. When using large lattices, it can be necessary to speed up the process by using multiple streams. At some configuration  $m$ , two processes  $a$  and  $b$  are started with  $m$  as their base configuration, but different states of their pseudo random number generators. Thus, successive configurations  $(m + i)_a$  and  $(m + i)_b$  will differ, and after a number of heat bath updates needed to decorrelate, two independent streams  $a$  and  $b$  allow to double the output of configurations.

In terms of the computational effort to generate a new configuration, the heat bath algorithm and similar processes scale deterministically linear with the lattice volume  $N_\sigma^3 \cdot N_\tau$ , since for each update the same constant number of numerical operation per lattice site is needed.

## 1.5 Meson correlators

An important aspect of lattice QCD in general, and the use of lattice QCD in this work in particular, is the study of the meson spectrum by calculating meson correlation functions on the lattice.

A meson operator  $O(x)$  is defined in terms of the quark fields  $\psi(x)$  as

$$O_\Gamma(x) = \bar{\psi}(x)_\alpha \Gamma_{\alpha\beta} \psi(x)_\beta \quad (1.40)$$

where the matrix  $\Gamma$  sets the quantum numbers of the operator and thereby fixes the particle the operator relates to. Possible choices for  $\Gamma$  and their realization in the staggered action are discussed below. Using  $O_\Gamma(x)$ , a meson correlator,

$$\begin{aligned} G_\Gamma(x) &= \langle O_\Gamma(x) O_\Gamma^\dagger(0) \rangle \\ &= \langle (\bar{\psi}(x)_\alpha \Gamma_{\alpha\beta} \psi(x)_\beta) (\bar{\psi}(0)_\xi \Gamma_{\xi\zeta}^\dagger \psi(0)_\zeta) \rangle \end{aligned} \quad (1.41)$$

is obtained as a four-point function in terms of the quark fields  $\psi(x)$ . Choosing 0 as one fixed point of the correlator is by convention, since translational invariance of the lattice allows any choice here.

---

<sup>1</sup> Here 'serial' does not refer to the capabilities of a specific software implementation (which of course can and often will be parallelized), but to the process itself.

## 1 Lattice QCD

The correlation function is evaluated by integrating out the fermion fields

$$\begin{aligned}
G_\Gamma(x) &= \frac{1}{Z} \int \mathcal{D}U \mathcal{D}\bar{\psi} \mathcal{D}\psi \left( \bar{\psi}(x)_\alpha \Gamma_{\alpha\beta} \psi(0)_\beta \right) \left( \bar{\psi}(x)_\xi \Gamma_{\xi\zeta}^\dagger \psi(0)_\zeta \right) \exp(-S_{\text{QCD}}) \\
&= \frac{1}{Z} \int \mathcal{D}U \det[D] \exp(-S_G[U]) \\
&\quad \times \left( \underbrace{\text{Tr} \left[ D^{-1}(x|0) \Gamma D^{-1}(0|x) \Gamma^\dagger \right]}_{\text{connected}} - \underbrace{\text{Tr} \left[ \Gamma^\dagger D^{-1}(0|0) \right] \text{Tr} \left[ \Gamma D^{-1}(n|n) \right]}_{\text{disconnected}} \right) \quad (1.42)
\end{aligned}$$

where in the quenched approximation again  $\det[D] = 1$ .

In eq. (1.42), the correlator splits into quark line *connected* and *disconnected* contributions. Evaluating the disconnected on the lattice is possible, but numerically it is quite costly.

For the meson screening mass analysis carried out in chapter 4, only flavor non-singlets are considered, where the disconnected part is zero. For the dilepton rate study, the quark line disconnected contributions to the vector current are neglected.

Solving eq. (1.42) yields the meson correlator for every point  $x$ . Usually the meson correlation function along the temporal or one of the spatial axis ( $z$  by convention) is of interest, where the three other dimensions are integrated up as

$$\begin{aligned}
G_\Gamma^{\text{temporal}}(\tau) &= \int_{V_3} d^3x G_\Gamma(\vec{x}) \\
G_\Gamma^{\text{screening}}(z) &= \int_\tau \int_{x,y} d\tau dx dy G_\Gamma(x, y, \tau). \quad (1.43)
\end{aligned}$$

The correlation function along the  $z$ -axis is often denoted the screening correlator, as it describes the screening of the meson by the surrounding medium.

### 1.5.1 Inverting the fermion matrix

With the definition of the meson correlator in eq. (1.42), it can be obtained from a lattice QCD calculation: The integral over the gauge configuration space  $\int \mathcal{D}U$ , the weight factor  $\exp(-S_{\text{QCD}})$  and the normalization by the partition function is taken care of by the importance sampling in the Markov chain process generating the configurations. As laid out above, in the quenched approximation these configuration do not depend on the fermion action and the weight is given by  $\exp(-S_G)$ .

Given an ensemble of  $N$  configurations, on each configuration  $i$  the observable  $O_i$  has to be calculated, and the sum  $\frac{1}{N} \sum_{i=1}^N O_i$  is an approximation of the thermal average  $\langle O \rangle$  in eq. (1.7). Therefore, to obtain meson correlators,

$$\text{Tr} \left[ D^{-1}(n|0) \Gamma D^{-1}(0|n) \Gamma^\dagger \right] \quad (1.44)$$

has to be evaluated for an ensemble of gauge configuration. This step is called the fermion matrix inversion, as  $D^{-1}$  has to be found for every gauge configuration.

The fermion matrix  $D$  is sparsely populated and large, so an actual inversion of the full matrix to find  $D^{-1}(n|m)$  is not feasible for even modest lattice sizes. However, to calculate eq. (1.44), only the inverse  $D^{-1}(n|0)$ , with respect to a source at  $m = 0$  is needed, which can be found by solving the corresponding system of linear equations. Taking into account the translational invariance, where  $m = 0$  is only chosen by convention and any other source position does not change the thermal average, finding the solution of  $D^{-1}(n|0)$  is mostly equivalent to inverting the full matrix.

Different numerical techniques are available to solve a system of linear equations, where for lattice QCD problems Krylov subspace solvers are widely established. A good overview is found in [21]. For this work, where calculations in the deconfined phase of QCD are carried out, the conjugate gradient algorithm is used.

To sample the path integral, the fermion matrices of an ensemble of gauge configurations have to be inverted, where a typical ensemble used in this work contains 100 to 400 configurations. In contrast to generating gauge configurations, there are no dependencies involved: Every configuration is inverted individually, so the speed of the process is only limited by the available computing resources.

The computational effort is harder to estimate and less deterministic: The solvers repeatedly have to apply  $D(n|m)$  to  $\psi(n)$ . The computational effort<sup>2</sup> to apply  $D(n|m)$  once scales linear with the lattice volume  $N_\sigma^3 \cdot N_\tau$ . However, the convergence behaviour of the solver is less predictable: With larger lattice volumes, usually a more exact solution is needed, so a lower residual has to be reached by the solver, increasing the number of needed  $D(n|m)$ -applications. Also, the over all convergence of a smaller system is often faster than on a large system. Both effects lead to a computational effort scaling worse than linear with the lattice volume.

The quark mass also has a profound effect on the convergence behaviour of the solver. It is related to the condition number of the matrix, where lower quark masses lead to higher condition numbers and thus to larger numbers of iterations needed to reach a given precision in the solver.

### 1.5.2 Meson correlators on the lattice

On the lattice, the integrals in eq. (1.43) turn into summations over lattice coordinates. The correlator can be projected onto finite momenta, which on the lattice are given by  $\vec{p} = 2\pi\vec{k}/(N_\sigma \cdot a)$  with integer values  $k_i$ . The momentum-projected correlator reads

$$\begin{aligned} G_\Gamma^{\text{temporal}}(n_t, p) &= \sum_{n_x, n_y, n_z} \exp\left(i \sum_{i=x,y,z} 2\pi k_i n_i / N_\sigma\right) G_\Gamma(\vec{n}, n_t) \\ G_\Gamma^{\text{screening}}(n_z, p) &= \sum_{n_x, n_y, n_t} \exp\left(i \sum_{i=x,y,t} 2\pi k_i n_i / N_i\right) G_\Gamma(n_x, n_y, n_z, n_t). \end{aligned} \quad (1.45)$$

with  $N_{x,y,z} = N_\sigma$ ,  $N_t = N_\tau$ .

---

<sup>2</sup>The computational effort is given by the number of operations (additions, multiplications, ...) needed for a certain computation.

State	Channel	$J^{PC}$	$\Gamma$	Particle
Scalar	S	$0^{++}$	$\mathbb{1}$	$a_0$
Pseudoscalar	PS	$0^{-+}$	$\gamma_5$	$\pi$
Vector	$V1 \dots V4$	$1^{--}$	$\gamma_1 \dots \gamma_4$	$\rho_1 \dots \rho_4$
Axialvector	$AV1 \dots AV4$	$1^{+-}$	$\gamma_1 \gamma_5 \dots \gamma_4 \gamma_5$	$a_1 \dots a_4$

Table 1.1: Quantum numbers for correlation functions in the form eq. (1.41), especially used for the Wilson fermion action. Abbreviations of the vector channel as  $V$  and the axial-vector as  $AV$  imply a summation of  $V1 \dots V4$  or  $AV1 \dots AV4$ .

Phasefactor $\zeta$	$\Gamma$		$J^{PC}$		Particles		Channel
	non-osc.	osc.	non-osc.	osc.	non-osc.	osc.	
$(-)^{n_x+n_y+n_t}$	$\gamma_3 \gamma_5$	$\mathbb{1}$	$0^{-+}$	$0^{++}$	$\pi_2$	$a_0$	$M_1$
$(-)^0 = 1$	$\gamma_5$	$\gamma_3$	$0^{-+}$	$0^{+-}$	$\pi$	—	$M_2$
$(-)^{n_y+n_t}$	$\gamma_1 \gamma_3$	$\gamma_1 \gamma_5$	$1^{--}$	$1^{++}$	$\rho_{2,T}$	$a_{1,T}$	$M_3$
$(-)^{n_x+n_t}$	$\gamma_2 \gamma_3$	$\gamma_2 \gamma_5$	$1^{--}$	$1^{++}$	$\rho_{2,T}$	$a_{1,T}$	$M_4$
$(-)^{n_x+n_y}$	$\gamma_4 \gamma_3$	$\gamma_4 \gamma_5$	$1^{--}$	$1^{++}$	$\rho_{2,L}$	$a_{1,L}$	$M_5$
$(-)^{n_x}$	$\gamma_1$	$\gamma_2 \gamma_4$	$1^{--}$	$1^{+-}$	$\rho_{1,T}$	$b_{1,T}$	$M_6$
$(-)^{n_y}$	$\gamma_2$	$\gamma_1 \gamma_4$	$1^{--}$	$1^{+-}$	$\rho_{1,T}$	$b_{1,T}$	$M_7$
$(-)^{n_t}$	$\gamma_4$	$\gamma_1 \gamma_2$	$1^{--}$	$1^{+-}$	$\rho_{1,L}$	$b_{1,L}$	$M_8$

Table 1.2: Quantum numbers associated with different staggered phase factors, for the oscillating and non-oscillating parity partner in the meson correlator channel of the staggered action, for screening correlators evaluated along  $n_z$  as used to calculate meson screening masses.

As a last component, the quantum numbers for the meson correlators have to be given. They correspond to the particle state and set by the matrix  $\Gamma$  in  $G_\Gamma$ .

Here the two fermion actions differ. For the Wilson action, this is easy, as  $\Gamma$  only has to be set to e.g.  $\mathbb{1}, \gamma_5, \gamma_1, \dots$ . The corresponding particle states with quantum numbers and abbreviations used in this work can be found in table 1.1.

For the staggered action, the situation is more involved: The quantum number given by  $\Gamma = \mathbb{1}, \gamma_5, \gamma_1, \dots$  can be translated to staggered phases  $\xi(n) \in -1, 1$ , entering into the correlator summation in place of  $\gamma$ -matrices in eq. (1.42). However, as a consequence of the rotation to obtain an action that is diagonal in Dirac space, the states mix. Along the  $t$ - or  $z$ -axis of the correlator, two particle states are found, where one state enters with an oscillating phase  $-1^{n_t}$  (for temporal correlators) or  $-1^{n_z}$  (for screening correlators), while the other does not oscillate.

Overall staggered phase factors  $\zeta$  for the meson correlation function and the resulting particle states for both the oscillating and the non-oscillating contribution are given in table 1.2, together with abbreviations used in this work.

## 1.6 Spectral functions

The spectral function  $\rho(\omega)$  describes the spectral composition of a correlation function. Physical properties such as transport coefficient of the medium and the presence of bound or unbound states of particles can directly be linked to spectral functions. Also, correlation functions in real time and in imaginary time can be obtained from  $\rho(\omega)$ . Thus the spectral function can be seen as the fundamental description of the underlying system, making it worthwhile to extract it from lattice data.

The vector meson spectral function plays an important role for the determination of thermal dilepton rates and the associated transport property, i.e. the electrical conductivity, on the lattice. A portion of this work deals with extending a study of thermal dilepton rates from lattice QCD. The ansatz used for the spectral function was developed in the course of the preceding work[7], where it has been motivated and presented in detail. The ansatz and a summary outlining its motivation can be found in the corresponding chapter on dilepton rates. The presentation in [7] also features a thorough description of spectral functions on the lattice and in QCD in general. Thus, the presentation is not repeated here, but only the key features and equations linking spectral functions to the lattice correlation functions are given.

The spectral functions determines the euclidean correlation function by

$$G(\tau) = \int_0^\infty \frac{d\omega}{2\pi} \rho(\omega) K(\tau, \omega) \quad (1.46)$$

with an integration kernel

$$K = \frac{\cosh(\omega(\tau - 1/2T))}{\sinh(\omega/2T)}. \quad (1.47)$$

In two limits, for large frequencies  $\omega \rightarrow \infty$  and for low or zero temperature,  $T \rightarrow 0$ , the kernel becomes  $K^{\text{lim.}} = \exp[-\omega\tau]$ , so

$$G(\tau) = \int_0^\infty \frac{d\omega}{2\pi} \rho(\omega) \exp(-\omega\tau) = \mathcal{F}[\rho](\tau) \quad (1.48)$$

where  $\mathcal{F}$  denotes a Laplace transformation. Ideally, the inverse transformation  $\mathcal{F}^{-1}$  could be carried out, giving direct access to the spectral function as

$$\rho(\omega) = \mathcal{F}^{-1}[G](\omega). \quad (1.49)$$

Unfortunately, finding  $\mathcal{F}^{-1}$  for a lattice correlation function is an ill-posed problem, subject to ongoing research[22].

Two ways to circumvent having to invert  $\mathcal{F}$  are discussed later in this work: Bayesian approaches try to find a most probable solution, by –roughly speaking– iteratively adapting a set of spectral function data points until the transformation through eq. (1.46) best matches a given correlation function. An ansatz-based approach sets a parametrized fixed functional form for  $\rho(\omega)$ , then a fit through eq. (1.46) to a given correlation function is used to fix the parameters. A more detailed description of both approaches is given in the chapter 5, where they are applied to study thermal dilepton rates.

## 1.7 Summary

To sum up, the following steps are taken to obtain meson correlation functions from a quenched lattice QCD calculation:

- Parameters as the desired lattice size  $N_\sigma, N_\tau$ , the lattice spacing  $a$ , the temperature and the coupling  $\beta$  are fixed. Of course not all parameters can be chosen independently, so for a systematic study a concept (e.g. the simulation at a fixed physical volume  $N_\sigma \cdot a$  and a set of spacings and temperatures) should be laid out first. Details on the relation between the coupling that is the input parameter to the Markov chain process and the physical scale  $a$  are found in chapter 3.
- As the first computationally expensive step, gauge configurations to sample the path integral in eq. (1.7) are generated. In the quenched approximation, these configurations only depend on the gauge action, so only the weight  $\exp(-S_G(U))$  is relevant in the Markov chain process. Thus, the configurations can later be used with any fermion action. Configurations are usually generated once and stored for later analysis.
- In the next step, the fermion matrix  $D(n|m)$  is inverted to  $D^{-1}(n|0)$ , by solving a variation of  $D\psi = \chi$ , where  $\chi$  is a point source. The structure of the fermion matrix is defined by the fermion action, see eqs. (1.28) and (1.36) and the coefficients are given by the gauge fields generated in the previous step. The inversion step has to be repeated for a number of gauge configuration to sample the path integral. Krylov subspace solvers are generally used for this step, in this work a preconditioned conjugate gradient solver is employed.
- By inverting the fermion matrix, the quark propagator is obtained. It is contracted to meson correlation functions through the summation laid out in eq. (1.42). The inversion of the fermion matrix and the calculation of meson correlation functions from quark propagators is usually joined in one step. The computationally expensive part is the matrix inversion, but quark propagators, especially for the Wilson action, are huge objects to store. It is therefore sensible to calculate all meson channels of interest directly after the matrix has been inverted and the quark propagator is still hold in memory, discarding it afterwards.

After these steps, thermal averages of meson correlation functions, often plainly referred to as *correlators*, have been obtained. Two different analyses, both based on the meson correlation functions, have been carried out in this work.

## 2 Parallel Lattice Code

Lattice QCD studies heavily rely on numerical calculations and advanced, large-scale computing. Over the last decades, the numerical algorithms, their implementation in lattice QCD software packages and the computing hardware to run these calculations got more complex and more sophisticated. An exhaustive overview over the current development in this field is far beyond the scope of this work. Thus, the summary given here focuses on the specific software development linked to this work, hopefully serving as a high level form of documentation for future users and programmers.

In the course of this work, a collection of lattice QCD software solutions has been developed. A common framework was designed and its parts were merged to one package, as of now plainly called the *(Bielefeld) Parallel Lattice Code*.

An overview of the current state of this software project is given. The focus lies on the documentation of general design goals and motivations that went into the project. As the software is currently in constant development by different users and for very different research goals, any state on the current capabilities can only be a snapshot. Probably – and hopefully – this portion of the documentation is outdated rather sooner than later.

### 2.1 Starting point and general decisions

Development started in 2010. At this point, legacy code based on Fortran-70 and MPI provided implementations of the heatbath algorithm (see section 1.4.1) and different Krylov solvers (see section 1.5.1) for parallel CPU systems. Development for this software was started in the mid-90s and constant updates (e.g. the addition of MPI file-IO) still provide a stable codebase. However, additions to the code became more and more difficult, and finally a decision was made to rewrite a CPU-centric lattice QCD framework from scratch.

The following list of goals for and requirements on the development process represent the current state in 2013. Some of the points were discussed and decided on before development started. Others were added and modified as the development process made them necessary or useful.

- Usability: The code base should be small enough, readable and well documented. New users, often students with varying programming experience, should be able to read, understand and extend the existing code quickly.
- Abstraction: High level functions do not depend on the implementation details on lower levels. For example, a routine contracting quark propagators to correlators should neither depend on the memory layout of the spinors nor on details of the communication subsystem like the number of cores the program is run on.

## 2 Parallel Lattice Code

- **Testing:** Tests on lower levels, like the correctness of single matrix multiplication, but especially on high levels are implemented. This allows to quickly check for obvious bugs after modifications and when running in new environments (new clusters, compilers, etc.)
- **Versioning:** The code, together with additional components like compile scripts and test results, is kept in a sourcecode management systems. This vastly simplifies collaborations and concurrent development.
- **Performance:** The code should scale reasonable well on CPU-based cluster systems. While a general software suite cannot reach the speeds of highly optimized QCD software packages, it should not impose performance penalties that are easy to avoid.
- **Interfaces:** It should be easy to interface the code with different storage formats (e.g. for gauge fields) and to interface with external libraries like QUDA[23] and USQCD/SciDAC[24].
- **Universality:** Unnecessary rewrites can be avoided by providing stable interfaces. For example, Krylov-solvers are to be written in a generic way so they are easy to adapt to different fermion matrix multiplication routings corresponding to different actions.

Below, the implementation of these goals is discussed in more detail for a representative subset of design decisions.

### 2.2 C++ as programming language and git for versioning

The software framework is written entirely in C++. For parallel runs, a communication framework (currently MPI) is needed. Otherwise, the code does not rely on external libraries. C++ was chosen as a programming language for a variety of reasons:

- The language is in wide use for numerical simulations, so it is supported by the optimized compilers and frameworks available on compute clusters. This excludes some otherwise promising languages as, for example, D<sup>1</sup>.
- Scripting languages like Python and LUA and (very) high level languages based on virtual machines like Java, impose higher performance penalties in the low level numeric routines. While lattice QCD frameworks in these languages exist<sup>2</sup> and are arguably easy to use, they rely on low level libraries in other languages to effectively manage the numeric workload.

---

<sup>1</sup> D is a successor to the C programming language. In contrast to C++, it trades some backwards compatibility for a cleaner redesign. While in active development, it is not nearly as widely used as C++. Documentation can be found on the official website [dlang.org](http://dlang.org).

<sup>2</sup>For example, QLUA is a framework in the Lua scripting language, providing an interface to SciDACs base libraries[24].

- As a massively parallel software system, MPI[25] has to be supported as a common denominator for interfacing with communication subsystems. With its closeness to C, C++ makes it easy to interface with MPI routines.
- In contrast to plain C, C++ integrated object-oriented features like classes, templates and operator overloading. This helps to keep the source code more readable (`a+=b` instead of `sumSpinor(a,b)`) and helps to avoid certain classes of errors, especially memory leaks and segmentation faults.

It should be noted that current versions of Fortran fulfill all of the above requirements as well, so the reason to choose C++ over Fortran is not so much a technical than a practical: Fortran was designed as a domain-specific language for numerical calculations, where it is still in wide use. C and C++ started out as general purpose languages with a focus on programming "near" to hardware (operating systems, high performance), and their concepts and syntax had a large influence on other programming languages. As a result, students working with software for some month –for example as part of a masters thesis– are more likely to have prior experience with C++ than with Fortran. Also, experience with and knowledge in C++ has broader applications outside of the field of numerics.

GIT was chosen as a source control / versioning system for the development. The distributed layout of Git makes it very suitable for the usual code development style in an academic environment. It is in use for large projects, most prominently the Linux kernel, so it is well established. One often quoted drawback is the rather steep learning curve: Especially when merging two code development branches a somewhat deeper understanding of the process is often necessary to resolve merging conflicts. When starting new projects today, FOSSIL provides an alternative to Git that addresses some of its usability issues. In fig. 2.1 a snapshot (from the graphical interface GITK) gives an impression of the quite active development process in 2013.

## 2.3 Modular and layered design

The Parallel Lattice Code is structured into multiple components, that can roughly be divided into major building blocks providing certain functionalities: Fundamental data types that are entries of single links and lattice sites, lattice-wide container objects for these data types, base classes implementing memory layout and an interface to the communication subsystem, and high level implementation of fermion actions, Krylov solvers and so forth on top of this base. In the following, a short overview with code fragments illustrating the use of these components is given.

### 2.3.1 Fundamental data types on single sites and links

A set of classes provides per-site or per-link objects. For example, `PsiEntry` is made up of  $4 \times 3$  complex numbers and holds the Wilson spinor at one site. The `SU3` class holds an SU3-Matrix and thus implements a link. All these classes define operators to allow

## 2 Parallel Lattice Code



Figure 2.1: An illustrative snapshot of the git history (visualized by the GITK software) in a timeline view, showing the code development in all branches chronologically.

multiplications, additions and so forth between them. They can also be templated, so they allow for different floating point precisions. A fragment of code multiplying a spinor entry `p1` with an SU3-Matrix `link1`, storing the result in `p2`:

```
PsiEntry<double> p1, p2;
SU3<double> link1;

p2 = link1 * p1;
```

While this code fragment compiles, all entries and results would be zero, as `p1`, `p2` and `link1` are initialized to zero by default when created.

### 2.3.2 Lattice-wide containers

Lattice-wide objects like `Spinor` and `Gaugefield` provide containers to the fundamental data types. They provide a set of functions, some of these depending on their per-site / per-link base data type:

Each lattice-wide object manages the allocation of its memory when created and free the memory in its destructor. This greatly helps to avoid memory leaks.

The operator overloading of the base datatype is passed through to the lattice-wide level. Thus, a lattice-wide spinor can be multiplied by a scalar or added to another spinor without explicitly programming a loop over its elements.

```
// 'lat' is a reference to the index management class Lattice
Spinor<double> sp1(lat), sp2(lat);

// initialize the spinors to 1 on every site
sp.setOnes();

// multiply 'sp1' by 4.2
sp1 *= 4.2;

// add 'sp2' to 'sp1'
sp1 += sp2;
```

Currently, this concept has certain limits: While `c=a; c+=b;` is available for lattice-wide objects, a simple `c=a+b;` is not. This is due to the operator overloading mechanism in C++: `a+b` gets executed first and the result would have to be stored in a temporary, lattice-wide object before being assigned to `c`. With spinors easily taking up multiple gigabytes of memory, this is not practical. A solution to this is possible, but rather complex to implement<sup>3</sup>.

Typical contractions like scalar products and norms are implemented, together with lattice-wide initializations (to zero, unity, random numbers, ...). Specific functions, like unitarization and calculation of plaquettes for the gauge fields, are also available.

<sup>3</sup> A way to solve this problem is create a stack of operators that is only executed when the result is assigned: In this way, `a+b` does not create a full temporary spinor, but only an object storing the information that spinors `a` and `b` have to be added. When the `=`-operator is called (or `+=` etc.), the accumulated operators on the stack are executed for each site of the lattice. This concept is implemented in QDP++, part of the SciDAC suite.

## 2 Parallel Lattice Code

The containers provide access functions. Their functionality might not be as clear as for the other, quite self-explaining operators: The pointers and allocated arrays for the fundamental data types are private to the container class, thus they cannot directly be accessed from the outside of the class. This greatly helps to avoid segmentation faults that occur through indexing errors. To access an element stored in the container, access functions are provided, where `get` retrieves an element and `set` sets it.

The position for retrieving and setting elements is not provided as an integer. Instead, an object called `LSite` is passed to every function that requires a position on the lattice. The advantage of this concept is that it decouples the memory layout from computations of coordinates in the code. The user can use different index schemes (e.g. cartesian coordinates  $x, y, z, t$ , a lexical index, etc.) independent of the underlying memory layout. For example:

```
// Retrieve a link in direction mu=1 at position 2,3,4,5
// Retrieve a link in direction mu=0 at lexical index 42
// 'lat' is a reference to the index management class Lattice

Gaugefield<double> gauge(lat);
SU3<double> result;

LSite pos = lat.site(2,3,4,5);

result = gauge.getLink( pos, 1 );
result = gauge.getLink( lat.siteFromLexical( 42 ) , 0 );
```

### 2.3.3 Memory layout management through the lattice class

The handling of memory layout is a basic component in the Parallel Lattice Code. As memory is accessed in a linear way, a four-dimensional position on the lattice has to be mapped to a one-dimensional index or offset. The easiest way is to use a lexical index, where the index  $i$  is given by

$$i_{\text{Lex.}} = n_t \cdot N_\sigma^3 + n_z \cdot N_\sigma^2 + n_y \cdot N_\sigma + n_x. \quad (2.1)$$

with the convention  $n_x, n_y, n_x \in [0, N_\sigma - 1]$  and  $n_t \in [0, N_\tau - 1]$  as already given in eq. (1.10). Influenced by the numerical algorithms, especially the Krylov solvers, often a layout that splits into an even and an odd part is preferred, where

$$i_{\text{E/O}} = (n_t \cdot N_\sigma^3/2 + n_z \cdot N_\sigma^2/2 + n_y \cdot N_\sigma/2 + n_x/2) \\ + (x + y + z + t) \bmod 2 \cdot (N_\tau \cdot N_\sigma^3/2) \quad (2.2)$$

Additionally, so-called halos have to be provided when working with parallel code: Each node holds a part of the global lattice, and since the communication system needs to transfer larger chunks of data to work efficiently, each node keeps copies of the lattice borders of its neighbours that are synchronised if needed.

Two obvious solutions to store these copies exist:

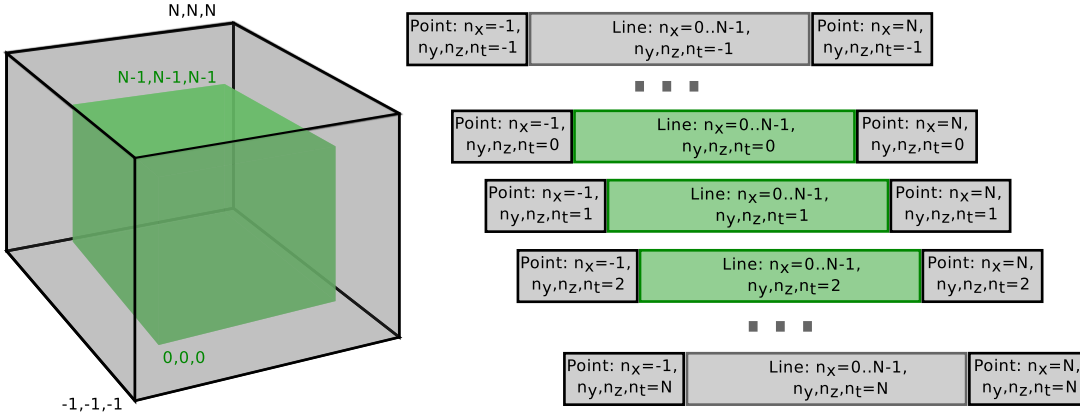


Figure 2.2: Memory mapping of the cartesian indexer. The local lattice ( $n \in [0, N - 1]$ ) and the halos containing next neighbours ( $n = -1, N$ ) are part of one memory block.

1. The halos can be part of the local lattice, enlarging it in every direction. By substituting  $n'_{x,y,z,t} = n_{x,y,z,t} + 1$  and  $N'_{\sigma,\tau} = N_{\sigma,\tau} + 2$  in eqs. (2.1) and (2.2) a new memory position is acquired, where e.g.  $n_z = -1$  and  $n_y = N_\sigma$  can be used to access lattice points of neighbouring nodes. With the substitutions, the resulting index  $i'$  will be within 0 and  $N'^3_{\sigma} \cdot N'_\tau$ . This variant is referred to as the *cartesian* index in the code. A diagram how the lattice is mapped to memory can be found in fig. 2.2. In this index scheme, a loop over the local lattice volume cannot be performed by a simple incrementing memory offset, since it would also access the storage positions for the copies of sites on neighbouring nodes. The `LSiteIter` objects explained below offer an easy solution, independent of the memory layout.
2. An alternative is to not change the mapping of the local lattice coordinates, but to store all halos after the local lattice. The local lattice (from 0 to  $N^3_{\sigma} \cdot N_{\tau}$ ) is followed by two 3-dimensional plane  $n_y, n_z, n_t$  where  $n_x = -1$  and  $n_x = N_{\sigma}$ , followed by two 3-dimensional planes  $n_x, n_z, n_t$  where  $n_y = -1$  and  $n_y = N_{\sigma}$  and so forth. After the 8 3-dimensional planes that make up the surfaces of a 4-dimensional hypercube, 2-dimensional planes with e.g.  $n_x = n_y = -1$  follow. Since the local lattice is not interrupted by stored copies of sites on neighbouring nodes, thus linear in memory, this layout is referred to as the *linear* index in the code. The index calculation  $(n_x, n_y, n_z, n_t) \rightarrow i$  for sites on neighbouring nodes becomes involved in this scheme, but a commented implementation exists in the `lattice_linearOffsets.h` and a graphical representation can be found in fig. 2.3.

Both the cartesian and the linear indexer have been implemented, where for both either an even/odd splitted or a lexical layout can be chosen for the local lattice. Other layouts can easily implemented by providing a function to calculate the index as in eqs. (2.1) and (2.2). The `Lattice`-class, also referred to as *the indexer*, is used as a central interface, allowing to convert between coordinates  $n_x, n_y, n_z, n_t$  and a memory offset  $i$ .

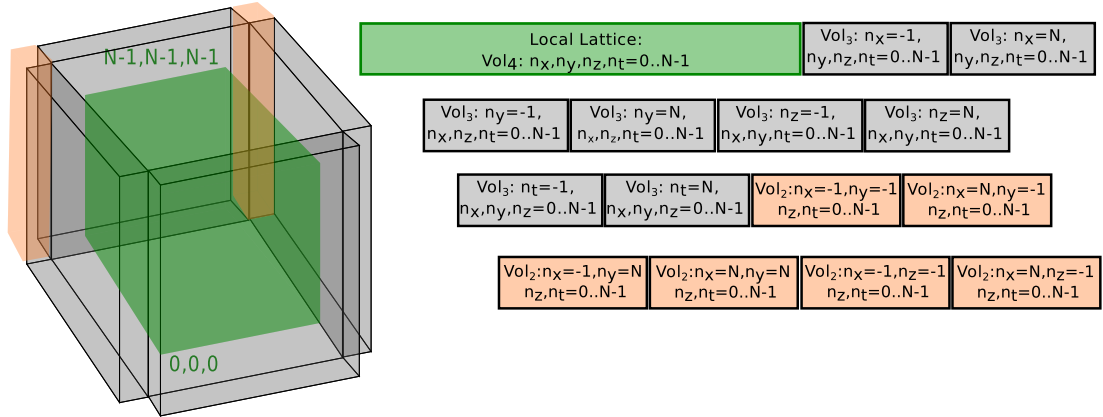


Figure 2.3: Memory mapping of the linear indexer. The local lattice ( $n \in [0, N - 1]$ , denoted  $\text{Vol}_4$ ) is mapped to one linear memory block (hence the name). It is followed by the 8 three-dimensional ( $\text{Vol}_3$ ) planes containing the next neighbours. After these, two-dimensional planes ( $\text{Vol}_2$ ) where e.g.  $n_x = -1$  and  $n_y = N$  are stored.

### 2.3.4 Positions on and iterations over the lattice

Positions returned by the `Lattice`-class are not mere integer numbers for the offset  $i$ , but objects of type `LSite`. An `LSite`-instance can be passed to any function that requires a lattice position as input, especially the `get` and `set`-functions of containers. This abstraction layer offers two main advantages: It discourages index computations in higher level code, so they stay centralized in the `Lattice` class. It also allows to change the storage format for different implementations and to store additional information.

Currently an `LSite` objects offers two memory offset: A call to `fpos()`, denoting a full lattice, returns an offset that allows to store a layer of sites of neighbouring nodes. A call to `ipos()`, denoting the inner lattice, returns an index for objects where only local sites are needed. The clover term provides a typical example where this method saves memory, since in a typical Wilson action no neighbouring clover matrices are needed in the fermion matrix multiplication. The `Lattice` class provides functions to query how many sites have to be stored for both `fpos` and `ipos`.

The `Lattice`-class provides two more important interfaces:

- Neighbours to a site are computed by calls to `site_up` or `site_dn` with an `LSite` for the position and a direction  $\mu = 0, 1, 2, 3$ . The functions return a new `LSite` that obeys boundary conditions. For parallel code, they also check<sup>4</sup> if the new position is still within the limits of the halos.
- Loops over the lattice can be executed by `LSiteIter` objects, an extension to `LSite`. They can run over the whole lattice, only the even or odd numbered sites, or even

<sup>4</sup>For performance reasons, the index checks performed can and should be turned off in production code. A central compile switch is provided for this purpose.

```

Lattice lat( ... );           // init of the lattice class
Gaugefield<double> gauge(lat); // init of a gauge field
SU3<double> tmp;

LSiteIter i;                 // an iterable LSite
LSite     j;                 // an LSite storing a position

// An iteration over the whole lattice
for ( i=lat.iterAll(); i.cont() ; i.iter() ) {
    // i inherits LSite, so it can be used in any function
    // that works with an LSite
    tmp = gauge.getLink(i,3);
}

// An iteration over the even sublattice
for ( i = lat.iterEO(false); i.cont() ; i.iter() ) {
    // get the position of the upper neighbour in dir mu=1
    j = lat.site_up(i,1);
    // use that position to retrieve a link
    tmp = gauge.getLink(j,3);
}

```

Figure 2.4: A code fragment demonstrating the use of lattice iterators and calculation of neighbouring sites through the `Lattice` class.

a 3-dimensional subcube with e.g.  $n_t = 4$  fixed. These *iterators* only guarantee that each site within their scope is set exactly one time, the order is not fixed so it can be changed for optimization. They are especially important when using the cartesian indexer, as they allow to run a loop over (parts of) the lattice without resorting to index calculations through e.g. the `siteFromLexical`-function in the `Lattice` class.

In fig. 2.4 a commented code fragment demonstrating the use of these features is given.

### 2.3.5 Communication abstraction and parallelism

Lattice QCD calculations often run in a parallel environment. The lattice is distributed among a set of machines, where each machine or –more precisely– process only holds a portion of the global lattice, the so-called local lattice. The size of local lattices does not differ between the processes, but while global lattices are usually cubic<sup>5</sup> ( $N_\sigma^3$ ), the local lattices do not have to be and often are not. Communication between the nodes is necessary at the boundaries, where a site  $n + \hat{\mu}$  is stored in the memory of a different process than the site  $n$ .

In its current state, the Parallel Lattice Code offers two modes to run: In *scalar* mode, it runs as a single process. In *parallel* mode, it uses a communication subsystem to run

<sup>5</sup>In its current state, the Parallel Lattice Code generally does not assume a cubic lattice  $N_\sigma^3$ . However, non-cubic lattices have not yet been used or tested.

in parallel on multiple nodes. A compile switch is used to switch between modes at compile time.

Scalar mode has two applications: It can be used for development and testing, e.g. on a laptop or desktop machine, where it does not require the user to install a communication framework like MPI. It can also be used to interface with GPU-assisted computations, where only a single controlling CPU process and no dependence on additional external libraries are desired.

Parallel mode is used to run across multiple instances of the code, usually running on multiple cores and multiple nodes.

The class `CommunicationBase` provides a simple interface to send/receive data between neighbouring nodes and to perform global tasks like sums and averages over values. It currently interfaces with the Message Passing Interface library to interchange data, but it could easily be extended to support other communication frameworks. Through this abstractions, no changes in other parts or higher levels of the code are necessary. `CommunicationBase` and `Lattice` interact closely: In parallel mode, communication buffers for sites on neighbouring nodes are provided by `Lattice` and filled by functions called through `CommunicationBase`. In scalar mode, `Lattice` satisfied the correct boundary conditions, while most operations in `CommunicationBase` return instantly.

### 2.3.6 High level functions

The classes for lattice-wide objects as `Spinor` and `Gaugefield` together with the memory layout management provided by the `Lattice` class make up the base structures for the code. Additional elements currently include the `CommunicationBase`, which is explained in more detail above, and a set of classes for parameter management.

Parameters as lattice size, node layout and  $\beta$ -value are set in human-readable file format. The `ParameterManagement`-class reads this file, checks the values for consistency and provides an interface to retrieve them. Inheritance of this class is used to provide parameters only used for specific calculations, e.g. the stopping residual for the conjugate gradient algorithm. In fig. 2.5 a schematic drawing of the dependency and layout between the base classes can be found. This scheme is simplified, so it does not directly map to class names for all parts used in the code.

Two typical lattice QCD tasks have been implemented together with the base architecture to test the code and provide a foundation to start further development from: A Wilson/clover fermion matrix inverter using an conjugate gradient inverter and a heatbath / overrelaxation code to generate quenched gauge configurations.

The schematic diagram of the inverter is given in fig. 2.6. Besides using the base functions, classes providing the `aslash` operations, applying the clover matrix and running the conjugate gradient inverter have been added. Additionally, some structure to store the inverter results and to contract the quark propagators to (meson) correlators was needed and implemented. Of course inverter, fermion action and correlator computation are independent and can be swapped out for different implementations.

An overview of the heatbath / overrelaxation code can be found in fig. 2.7. This code is not as complex as the inverter, as it only needs the gauge field as a lattice-wide

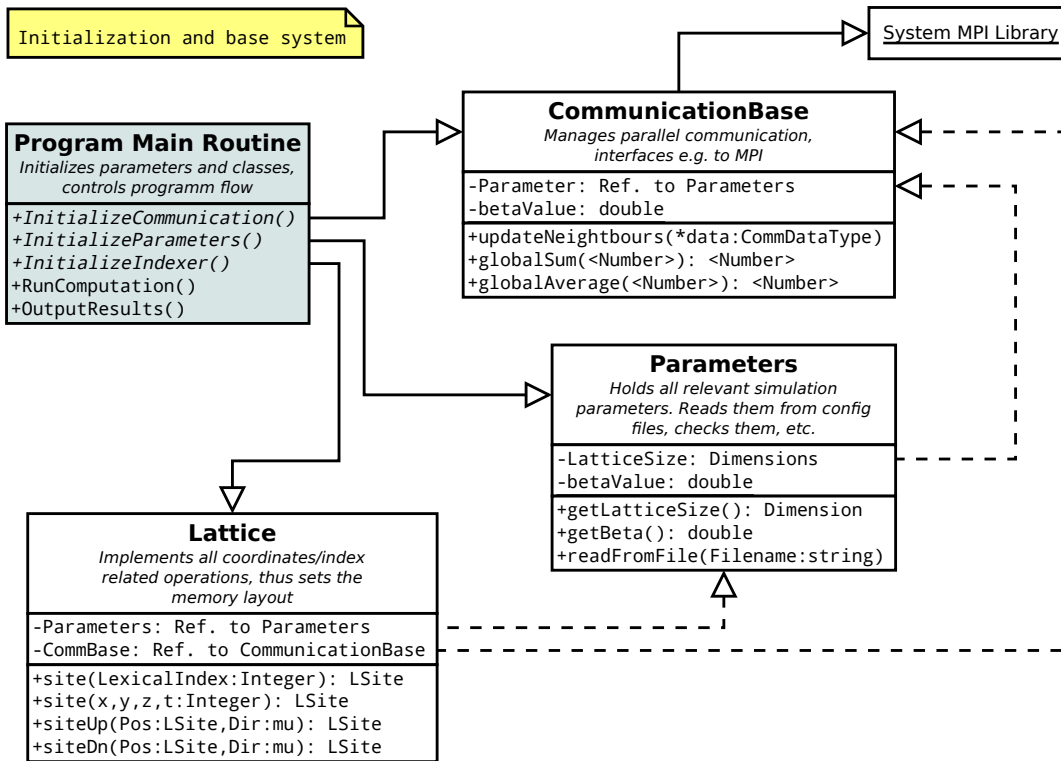


Figure 2.5: A schematic diagram of the Parallel Lattice Code initialization phase and main components. The lattice class controls the per-node memory layout, the Communication class abstracts the communication layer and interfaces to MPI. This scheme is simplified, so not all class and method names map one to one to the actual implementation.

object. It however motivated the implementation of another important component, a parallel pseudo random number generator. This generator keeps a separate state for each lattice site. It can be initialized from one global seed and makes the generation of random numbers independent of the parallelization: Using the same initial seed or reading the same initial state from disk, the random numbers retrieved at a specific site do not depend on the number of nodes or if the code is run in parallel at all. This greatly simplified searching for errors in code depending on random numbers.

## 2.4 Automated unit tests

An important part of software development is testing. In a complex project, structured testing of code components greatly reduces the amount of time needed to locate an error and to fix it. In its current state, the Parallel Lattice Code offers two sets of tests:

A package of tests checks the memory layout and communication subsystem. It fills a

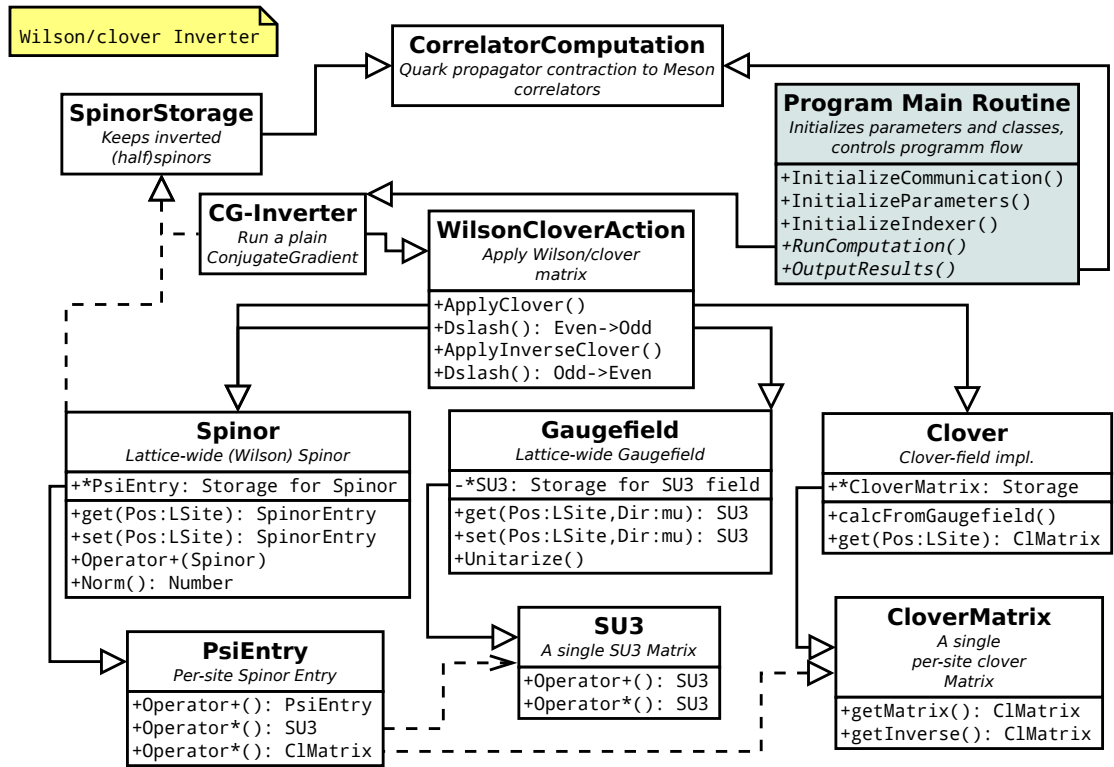


Figure 2.6: A schematic diagram of a Wilson/clover fermion matrix inverter implemented in the Parallel Lattice Code. See fig. 2.5 for the initialization phase.

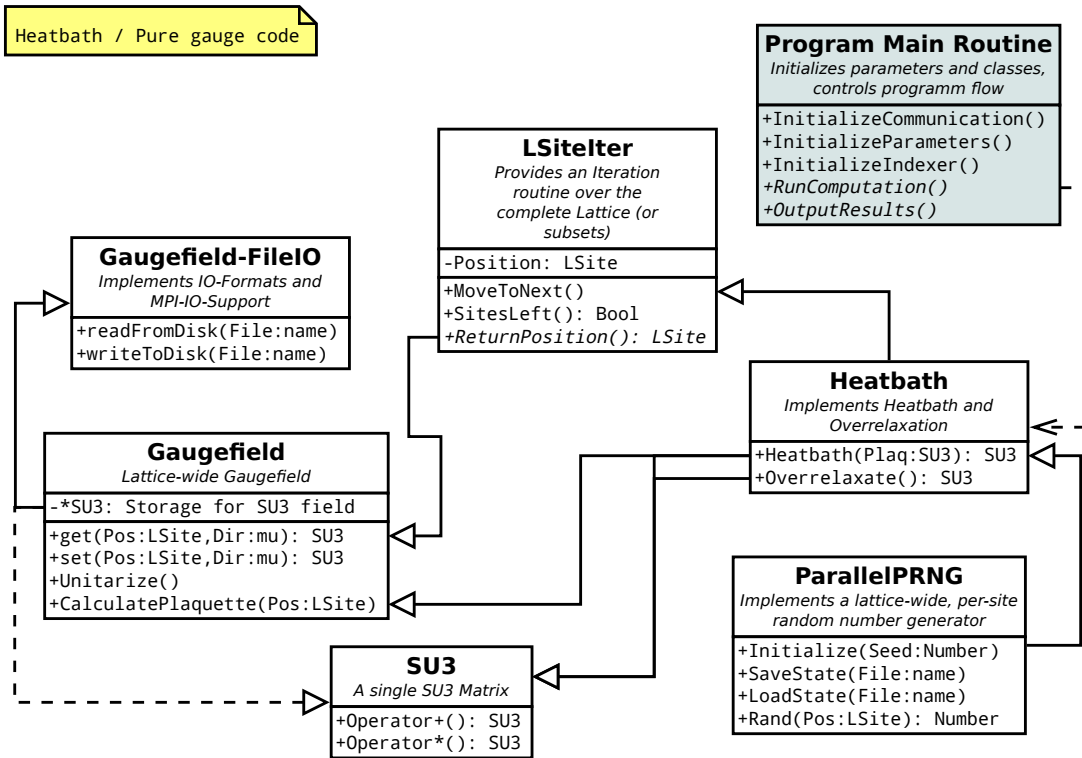


Figure 2.7: A schematic diagram of a quenched gauge configuration generation program implemented in the Parallel Lattice Code. See fig. 2.5 for the initialization phase.

## 2 Parallel Lattice Code

lattice-wide structure with coordinates, repeatedly uses the `site_up`- and `site_dn` functions to retrieve neighbours and checks if these results are correct. It also checks if an update written on neighbouring nodes correctly propagates through the communication system.

On a high level, automated tests of whole computation steps are provided: For example, the inverter test reads a small lattice configuration, computes a fixed number of 5 conjugate gradient steps and compares the resulting quark propagator as well as the meson correlators with files stored on disk. In between, also the clover matrices and the dslash operation are tested against stored results. Error messages allow to check which part of the calculation causes errors. The code for quenched gauge field generation tests its components in a similar manner.

The high level tests also have been automated: A simple set of scripts compiles and runs the testers with different settings and logs the output. This checks if all algorithms run correctly in scalar / parallel mode and with different indexers. If new algorithms are added, it is highly advisable to add corresponding test routines.

### 2.5 Current state

As of writing this work, the code is in active use and development by different users and in different projects, so this status summary can only provide a snapshot of the development state.

Following the initial design phase, the first part that was fully tested and working was a Wilson/clover fermion matrix inverter using an even/odd preconditioned conjugate gradient solver. The legacy Fortran code provided the same functionality and was used for extensive testing, down to per-site comparison of results. Its output has also been used to provide the known-good results now checked by the automated testing routines.

Complementing the inverter, a heatbath / overrelaxation code was added and tested. This part motivated the implementation of the parallel pseudo random number generator. It also completed the code base, as now generation as well as analysis of quenched gauge configuration is implemented. The implementation is based on a scalar C code that has been in constant use and thus thoroughly tested.

With this code base in place, different new projects have been realized: The calculating of Wilson loops and a multi-shift inverter have been implemented. An algorithm to calculate diffusion coefficients has been ported, where first results have already been presented[26].

The code has also been extended to allow overlap calculations, where in this process interface classes to the QUDA software package[23] have been implemented. First results from these calculations are also available[27].

### 2.6 Outlook, planned features

The Parallel Lattice Code currently is in active development. A set of extensions and new features that would benefit projects based on the code have already been considered:

The core dslash routines, implementing the fermion action, undergo constant performance tuning.

An interface to the QUDA software suite is currently in productive use and might be extended to allow a more general interface to QUDA. Also, core routines as a Wilson dslash and linear algebra for spinors exists in NVIDIAs CUDA language, allowing to use GPU systems without relying on external libraries.

An interface to the SciDAC software suite would open up the possibility to use highly and machine-specificly optimized codes provided with these packages. The necessary adjustments would be more extensive than only writing an interface class, as the QDP-libraries needed for SciDAC do not allow a low-level, per-site access to lattice-wide objects. Thus, modifying the code to interface with SciDAC is a larger task.



## 3 Scale setting

Scale setting and renormalization are important prerequisites in lattice QCD calculations. In contrast to other fields where complex computer simulations are employed (for example finite element analyses in engineering), scales in lattice QCD are not merely an input parameter to the model. They have to be extracted from suitable observables and often have to be tuned and (re)checked.

When generating quenched gauge configurations, see section 1.4.1, only three parameters set the physical<sup>1</sup> properties of the ensemble: The spatial ( $N_\sigma$ ) and temporal ( $N_\tau$ ) extent of the lattice and, most importantly, the coupling as  $\beta = 6/g^2$ . These parameters are dimensionless in nature and have to be linked to physical scales of temperature and lattice spacing.

When calculating the standard point-to-point meson correlators that are the basis for most analysis performed for this thesis, only one further parameter setting the quark mass has to be fixed. For standard staggered fermions, a bare quark mass enters into eq. (1.34) which has to be renormalized and quoted in a certain scheme, e.g.  $m_{\overline{MS}}$ . For clover-improved Wilson fermions, the quark mass cannot directly be set, but the  $\kappa$  parameter that enters into the action in eq. (1.28) has to be tuned, usually by measuring a suitable physical observable that relates to the quark mass. Again this mass has to be renormalized and converted to a scheme like  $m_{\overline{MS}}$ .

Finally, correlation functions of local currents –like  $G_V(\tau T)$ – have to be renormalized by a matching constant  $Z_V(g^2)$  after determining them on the lattice.

### 3.1 Determining lattice spacing

The most important step in fixing scales on the lattice is to assess how the scale, represented by the lattice spacing  $a$ , relates to the coupling  $g$ .

For this work, the SOMMER-scale is employed[28]. The dimensionfull observable  $r_0$  relates to the force between static quarks at intermediate distance, the dimensionless ratio  $a/r_0$  can be measured with high precision in pure lattice gauge theory.

The ratio  $a/r_0$  can be parameterized for a range of couplings  $\beta = 6/g^2$ , and via  $r_0$  the lattice spacing  $a$  is fixed for these couplings.

A rational approximation

$$\ln(r_0/a) = \ln(1/R(\beta)) \frac{1 + c_1/\beta + c_2/\beta^2}{1 + c_3/\beta + c_4/\beta^2} \quad (3.1)$$

---

<sup>1</sup>Other parameters, namely the number of configurations per ensemble, the number of updates between configurations and overrelaxation steps per update influence mostly autocorrelation, but not physical properties.

### 3 Scale setting

is chosen to relate  $a/r_0$  to the coupling  $\beta$ . In quenched lattice QCD,  $r_0 = 0.5$  fm is often quoted from the original analysis [28]. This is consistent with  $r_0 = 0.49(2)$  fm, which is used in this work and found in [29], where a summary of different currently available analyses is carried out.

In eq. (3.1),  $R(\beta)$  is the universal two-loop scaling function of  $SU(3)$  gauge theory. It enters to address the running coupling effecting  $a$  in  $a/r_0$  and is given by

$$\begin{aligned} R(\beta) &= \left(\frac{6b_0}{\beta}\right)^{-\frac{b_1}{2b_0^2}} \exp\left(-\frac{\beta}{12b_0}\right), \\ b_0 &\equiv \frac{11}{(4\pi)^2}, \quad b_1 \equiv \frac{102}{(4\pi)^4}. \end{aligned} \quad (3.2)$$

In the weak interaction limit  $\beta \rightarrow \infty$  of eq. (3.1), the factor entering through the rational approximation becomes 1, so

$$\ln(r_0/a) = \ln(1/R(\beta)) = \frac{4\pi}{33} \cdot \beta \quad (3.3)$$

is obtained. Thus, with  $a \cdot \Lambda = R(\beta)$ , it would follow that  $r_0 \cdot \Lambda = 1$ . This motivates to test an over all multiplicative factor to this relation, i.e.  $r_0/a = c_0/R(\beta)$ . The initial guess of  $c_0 = 1$  is not disfavoured by the fit, but the current precision of the data set does not allow to clearly constrain  $c_0$ .

Quenched lattice calculations for the results presented in this thesis are carried out at rather large extents  $N_\sigma, N_\tau$ , with small lattice spacings  $a$ . The corresponding couplings employed in this work range from  $\beta \approx 6.3$  up to  $\beta \approx 7.8$ .

Currently, the scale for couplings  $\beta > 6.9$  is known by extrapolation through eq. (3.1). A study extending the measurement of  $r_0/a$  towards higher values of  $\beta$  is in progress [26], but proves difficult: With smaller lattice spacings, high statistic and maybe more suitable observables are needed to obtain a clear signal.

As a part of this new analysis, new and precise data-points  $r_0/a$  were generated for couplings  $\beta < 7$ , serving as a crosscheck against and extend the results from [30, 31]. These points were used to fit eq. (3.1), fixing  $c_1, \dots, c_4$  to

$$c_1 = -7.36084, \quad c_2 = 10.6168, \quad c_3 = -2.64823, \quad c_4 = -11.2686 \quad (3.4)$$

A plot of the resulting function can be found in fig. 3.1, a summary of derived parameters for all couplings relevant in this thesis is given in table 3.1. While the new data points slightly change and improve the fit, the result are over all compatible with [29].

## 3.2 Critical temperature and temperature scale

The critical temperature  $T_c$  is a second important parameter in lattice QCD calculation. It is not a priori known, but has to be found by analysing a suitable order parameter for the phase transition. The analysis yields critical couplings  $\beta_c$  for values of  $N_\tau$  as  $\beta_c(N_\tau)$ . From these, a dimensionfull value  $T_c^{\text{quenched}} = \frac{1}{a(\beta_c) \cdot N_\tau}$  can be obtained.

### 3.2 Critical temperature and temperature scale

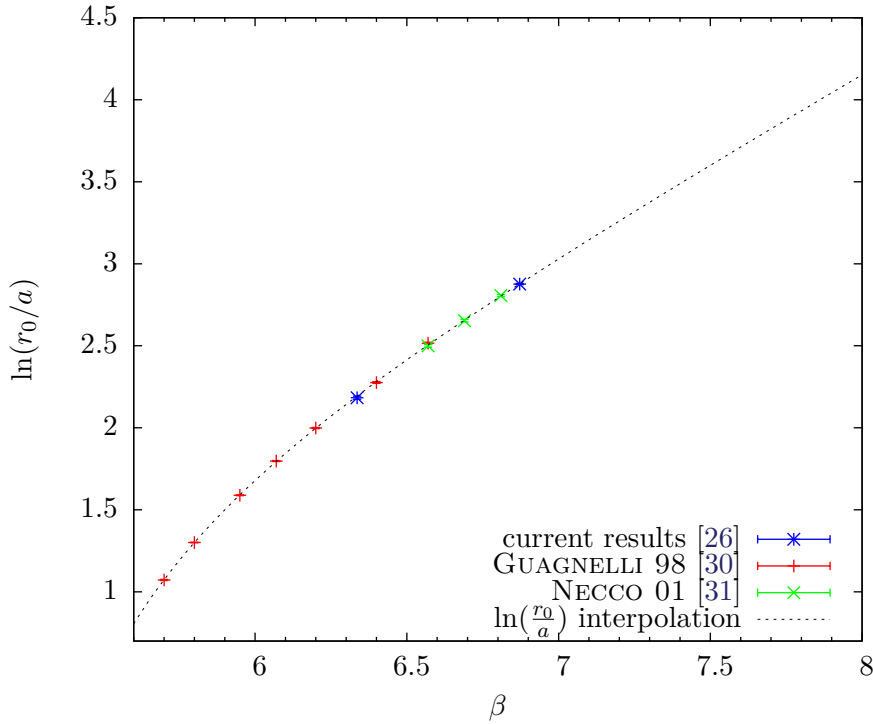


Figure 3.1: Ratio  $\ln(r_0/a)$  with data points from [30, 31], current results [26] and rational interpolation as given by eq. (3.1) with values  $c_1, \dots, c_4$  in eq. (3.4).

It is customary to quote the temperature  $T$  of quenched calculations as a ratio  $T/T_c$ , as the critical temperatures differ significantly between quenched and unquenched lattice QCD. Thus, quoting a temperature ratio is in almost all cases more meaningful than giving an absolute value  $T = \frac{1}{a \cdot N_\tau}$  obtained from the lattice length scale.

The following procedure is carried out to set the temperature scale:

- On a set of lattices with fixed temporal extent  $N_\tau$  and varying volumes  $N_\sigma = 2 \dots 4 \cdot N_\tau$  the Polyakov loop susceptibility is measured as an order parameter. By scanning a range of couplings  $\beta$ , the critical coupling  $\beta_c(N_\tau)$  is determined.
- With  $\beta_c(N_\tau)$  known for a set of  $N_\tau$ , a fit to obtain a continuum extrapolation fixing  $T_c \cdot r_0$  can be performed. Here, a quadratic dependence in the lattice spacing is assumed due to the  $O(a^2)$  discretization errors in pure gauge theory. The lattice spacing for each  $\beta_c(N_\tau)$  is obtained by eq. (3.1).

Currently new datasets for  $N_\tau = 8, 12, 14, 16$  have been analysed, were  $T_c \cdot r_0 = 0.7497(1)$  is found as the continuum result of the extrapolation and  $-0.221(7)$  is the slope of the extrapolation [26]. With these results,  $T_c \cdot r_0$  can be given as a function of  $a/r_0$ , which corresponds to the lattice spacing since  $r_0$  is fixed. A plot

### 3 Scale setting

is found in fig. 3.2, the relation is

$$[T_0 \cdot r_0](a/r_0) = 0.7497(1) - 0.221(7) \cdot (a/r_0)^2 \quad (3.5)$$

Using  $r_0 = 0.49(2)$  fm, this yields a critical temperature  $T_c^{\text{quenched}} = 301(12)$  MeV in the continuum limit  $(a/r_0) = 0$ . This value of  $T_c$  is slightly higher than  $T_c = 270(3)$  MeV, which was obtained from the string tension  $\sqrt{\sigma} = 428$  MeV and the relation  $T_c/\sqrt{\sigma} = 0.630(5)$  measured in [32].

- With  $\frac{a}{r_0}(\beta)$  known from eq. (3.1) and  $[T_c r_0](a/r_0)$  known from the extrapolation eq. (3.5), the temperature  $T$  in relation to  $T_c$  of a given lattice ensemble  $(\beta, N_\tau)$  can be determined. In general, (any) two temperatures  $T$  and  $T_c$  relate

$$\frac{T}{T_c} = \frac{(r_0/a)(\beta)}{(r_0/a)(\beta_c)} \cdot \frac{N_{\tau,c}}{N_\tau}. \quad (3.6)$$

Three slightly different methods to determine  $T/T_c$  can be set up. In table 3.1 results of all three are summarized for the lattice parameters  $(\beta, N_\tau)$  relevant in this work.

- $T/T_c$  can be calculated with the continuum extrapolated value for  $T_c \cdot r_0$  as

$$\frac{T}{T_c^{\text{cont.}}} = \frac{(r_0/a)(\beta)}{0.7497(1)} \cdot \frac{1}{N_\tau}. \quad (3.7)$$

- Alternatively,  $[T_c r_0](a/r_0)$  can be obtained at the same lattice spacing  $a/r_0$ , thereby the same couplings  $\beta = \beta_c$ , so effects by the finite lattice spacing enter into both  $T$  and  $T_c$ . This yields

$$\frac{T}{T_c^{\text{lat.}}} = \frac{(r_0/a)(\beta)}{0.7497(1) - 0.221(7) ([r_0/a](\beta_c))^{-2}} \cdot \frac{1}{N_\tau}. \quad (3.8)$$

- Finally, a standard way to determine  $T/T_c$  is to find the critical coupling  $\beta_c$  at the given  $N_\tau$ , so  $N_\tau = N_{\tau,c}$ , then using the ratios of lattice spacings to determine the temperature. If for a given  $N_\tau$  a data point  $\beta_c(N_\tau)$  is available, the temperature is

$$\frac{T}{T_c^{N_\tau}} = \frac{(r_0/a)(\beta)}{(r_0/a)(\beta_c^{N_\tau})}. \quad (3.9)$$

It should be noted that all three methods currently yield compatible results, so while it is easy to compensate for finite spacing effects, it does not seem necessary.

### 3.2 Critical temperature and temperature scale

$\beta$	$\frac{r_0}{a}$	$a[\text{fm}]$	$a^{-1}[\text{GeV}]$	$N_\tau$	$\frac{T}{T_c^{\text{cont.}}}$	$\frac{T}{T_c^{\text{lat.}}}$	$\frac{T}{T_c^{N_\tau}}$
6.338	8.99	0.05452	3.61946	8	1.499	1.504	1.511
6.503	11.22	0.04365	4.52025	10	1.497	1.501	-
6.640	13.38	0.03663	5.38738	12	1.487	1.489	1.493
6.768	15.67	0.03126	6.31236	14	1.493	1.495	1.497
6.872	17.77	0.02757	7.15751	8	2.963	2.966	2.987
				16	1.482	1.483	1.482
7.192	25.84	0.01896	10.40482	12	2.872	2.873	2.883
				24	1.436	1.437	-
				28	1.231	1.231	-
				32	1.077	1.077	-
7.458	34.92	0.01403	14.06233	16	2.911	2.912	2.913
				32	1.456	1.456	-
7.544	38.44	0.01275	15.48087	36	1.424	1.425	-
				42	1.221	1.221	-
				48	1.068	1.068	-
7.792	50.59	0.00969	20.37309	48	1.406	1.406	-
				56	1.205	1.205	-
				64	1.054	1.054	-

Table 3.1: Summary of lattice spacings and temperatures calculated for all lattice ensembles  $\beta, N_\tau$  relevant and used in this work. Lattice spacings  $a$  and inverse spacings  $a^{-1}$  are given by eqs. (3.1) and (3.4) with  $r_0 = 0.49\text{fm}$  (and  $1\text{ fm} = 1/197.33\text{ MeV}$ ),  $\frac{T}{T_c^{\text{cont.}}}$  from eq. (3.7), and  $\frac{T}{T_c^{\text{lat.}}}$  from eq. (3.7).  $\frac{T}{T_c^{N_\tau}}$  from eq. (3.9) is only calculated for  $N_\tau = 8, 12, 14, 16$  where data points  $\beta_c(N_\tau)$  are available.

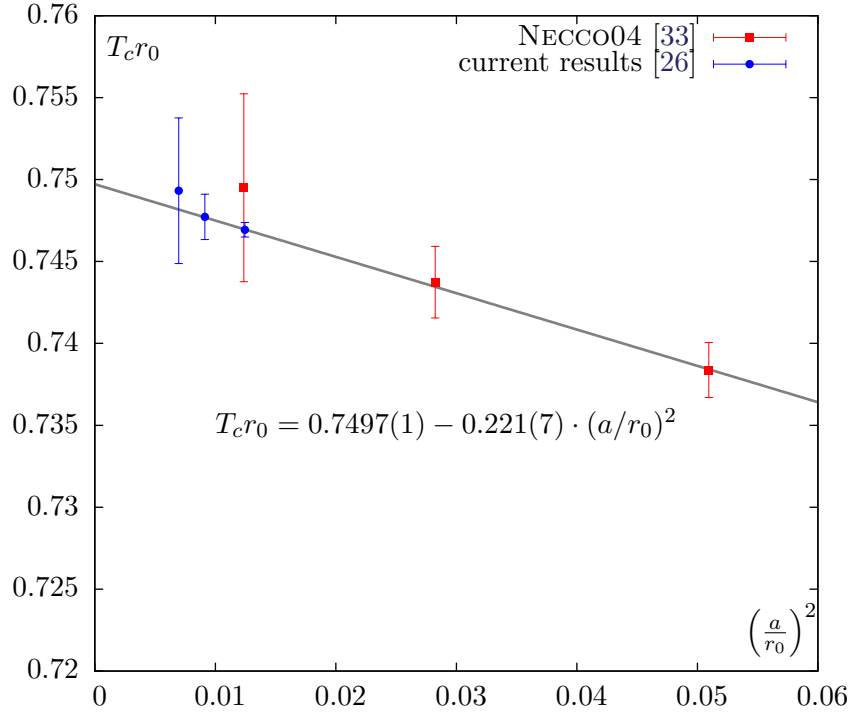


Figure 3.2: Plot of  $T_c \cdot r_0$  versus a representation of the squared lattice spacing through  $(a/r_0)^2$ , with data points and the continuum extrapolation fit.

### 3.3 Setting the quark mass

After the parameters controlling temperature and volume have been fixed when generating the gauge configurations, the quark mass has to be set when inverting the fermion matrix.

Quark masses are set or measured in bare lattice units. To compare and connect them to other QCD calculations, a suitable renormalization scheme has to be employed. It is customary to quote quark masses in the *modified minimal subtraction* scheme, denoted  $\overline{MS}$ , with the reference scale set to  $\mu = 2 \text{ GeV}$ . All quark masses used throughout this work are tuned to be in the light range, aiming at 5 to 20 MeV in  $\overline{MS}(\mu = 2 \text{ GeV})$ .

The procedure to determine the quark mass differs between the Wilson and the staggered action, so two summaries, one for each action, are given below. These are kept quite brief, because the methods are well established. They have been presented self-contained and in detail in previous works, matching citations are given.

The main goal here is to update the quark masses for all datasets relevant in this work, taking into account the new scales set above. All relevant parameters have been recalculated for all couplings, so minor differences emerge between the values given here and cited in previous works. Results are given in table 3.2 for the Wilson and in table 3.3

$\beta$	$\kappa$	$\kappa_c$	$u_0$	$g_{\overline{MS}}^2(\mu = 1/a)$	$m_{\text{AWI}}$	$m_{\text{RGI}}$	$m_{\overline{MS}}$
6.338	0.13572	0.13576	0.625696	2.088210	8.10	14.87	10.63
6.503	0.13550	0.13561	0.638617	1.948050	9.52	17.69	12.64
6.640	0.13536	0.13540	0.648507	1.847770	5.75	10.73	7.67
6.872	0.13495	0.13500	0.663786	1.703310	8.87	16.53	11.82
7.192	0.13440	0.13437	0.682457	1.541790	7.48	13.63	9.74
7.457	0.13390	0.13398	0.696209	1.431960	23.32	40.86	29.21
7.544	0.13382	0.13384	0.700439	1.399580	10.48	18.07	12.91
	0.13383		0.700439	1.399580	5.99	10.33	7.38
7.793	0.13340	0.133467	0.711851	1.315240	41.32	66.95	47.85
	0.13345		0.711851	1.315240	9.69	15.69	11.21

Table 3.2: Summary of Wilson quark masses determined for all combinations  $\beta$  and  $\kappa$  relevant to this work. All masses are given in units of MeV, where  $m_{\text{AWI}}$  is the AWI mass from eq. (3.11),  $m_{\text{RGI}}$  the RGI mass through eq. (3.14) and  $m_{\overline{MS}}$  the mass in the  $\overline{MS}$ -scheme at  $\mu = 2 \text{ GeV}$ .

for the staggered action.

### 3.3.1 Quark masses for clover-improved Wilson fermions

The clover-improvement of Wilson fermions has a profound effect on the quark mass determinations. In contrast to staggered fermions or Wilson fermions without improvement, the quark mass no longer is a direct input parameter. Instead, the hopping parameter  $\kappa$  in eq. (1.28) controls the quark mass and has to be tuned by extracting the mass through a suitable observable. A detailed presentation of the steps involved in this determination can be found in [7, 34], which should be used as a starting point if the process has to be reimplemented.

As a first step, a suitable observable to extract the quark mass is selected. For temperatures above the phase transition, as in this work, chiral symmetry is restored. The pion mass, a typical observable to tune quark masses, thus cannot be used. Instead, the axial Ward identity (AWI) [35]

$$Z_A \partial_\mu A_\mu^I = 2m_q Z_{\text{PS}} \text{PS}, \quad (3.10)$$

is employed, which can be rewritten in terms of 2-point functions as

$$\frac{Z_A \langle \partial_\mu A_\mu^I(\tau) \text{PS}(0) \rangle}{Z_{\text{PS}} \langle \text{PS}(\tau) \text{PS}(0) \rangle} = 2m_{\text{AWI}}. \quad (3.11)$$

Here  $A$  denotes the axial vector current, and  $\text{PS}$  denotes the pseudo-scalar density. The direction  $\mu$  is set to the time-like direction  $\mu = 4$  in the analysis, as here the

### 3 Scale setting

axial-vector current has the largest overlap with the pion state.

The index  $I$  in  $A_\mu^I$  denotes an improved current, that is defined as

$$A_\mu^I = A_\mu + ac_A \nabla_\mu \text{PS} \quad (3.12)$$

with the operator  $\nabla_\mu$  given as a combination of lattice forward  $\Delta^f$  and backward  $\Delta^b$  derivatives,  $\nabla = \frac{1}{2}(\Delta^b + \Delta^f)$ .  $Z_A$  and  $Z_{\text{PS}}$  are the renormalization constants of the corresponding currents, for which the currently known two-loop order results[36] are used in the analysis. The improvement coefficient  $c_A$  has been calculated non-perturbatively and parametrized [15] as

$$c_A = -0.00756 \frac{1 - 0.748 g_0^2}{1 - 0.977 g_0^2} g_0^2 \quad \text{for } 0 \leq g_0 \leq 1. \quad (3.13)$$

Here the index 0 has been added to  $g_0^2 = 6/\beta$ , to clearly distinguish  $g_0^2$  as the bare coupling.

In calculations to obtain sets of meson correlation functions, evaluating eq. (3.11) does not generate any considerable overhead, since almost all computing time is spend obtaining the quark propagators. However, in most cases a value for  $\kappa$  that corresponds to the desired quark mass has to be found first. For this tuning, eq. (3.11) is evaluated on a subset with lower statistics (10 to 20 configurations usually suffice) and, if available, on a set of lattices with lower  $N_\sigma$  (to reduce computing costs). From these data points, a matching  $\kappa$  is estimated and is rechecked while the final set of configurations is inverted.

From the AWI mass in eq. (3.11), the quark mass in the  $\overline{MS}$  scheme is computed in a two-step process: The bare mass is converted to the Renormalization Group Invariant quark mass  $m_{\text{RGI}}$  which —as the name suggests— is independent of the renormalization scheme and scale. The non-perturbatively improved RGI quark mass relates to the AWI mass  $m_{\text{AWI}}$  as

$$m_{\text{RGI}} = Z_m [1 + (b_A - b_{\text{PS}}) a m_q] m_{\text{AWI}} \quad (3.14)$$

with  $Z_m$  given in [37] as

$$Z_m(g_0^2) = 1.752 + 0.321 (6/g_0^2 - 6) - 0.220 (6/g_0^2 - 6)^2 \quad (3.15)$$

and the bare quark mass  $a \cdot m_q = \frac{1}{2\kappa} - \frac{1}{2\kappa_c}$ . The improvement coefficients of the axial current and pseudoscalar density have been non-perturbatively computed in [38, 39] to

$$(b_A - b_{\text{PS}})(g_0^2) = -0.00093 g_0^2 \frac{1 + 23.3060 g_0^2 - 27.3712 g_0^4}{1 - 0.9833 g_0^2} \quad (3.16)$$

As a second step, the RGI-mass, now at the scale  $\mu_0 = 1/a$ , is converted to  $m_{\overline{MS}}(\mu = 2 \text{ GeV})$  by doing a scale evolution through perturbative renormalization group functions, known with four-loop accuracy and readily implemented in a package (RUNDEC.M) for the Mathematica software suite [40].

For this work, the complete analysis process has been automated, so quark masses are calculated as a by-product of the main analysis with only minor additional effort. In

### 3.4 Non-perturbative renormalization for the vector current

table 3.2 a summary of the results for all relevant couplings  $\beta$  and hopping parameters  $\kappa$  is given.

#### 3.3.2 Quark masses for staggered fermions

The quark mass in the staggered fermion action enters directly into eq. (1.36) as a bare mass  $\hat{m}_q$ . Again two steps are performed to arrive at a mass in the  $\overline{MS}$ -scheme:

A matching procedure between the lattice and continuum operators, allowing to convert between the bare mass  $\hat{m}_q$  and a continuum mass  $m_q(\mu = 1/a)$  is deduced in [41]

$$m_q(\mu = 1/a) = \left[ 1 - \frac{g_{\overline{MS}}^2(1/a)}{(4\pi)^2} \cdot 39.1414 \right] \cdot \hat{m}_q \quad (3.17)$$

As for the Wilson quark masses, the running coupling is promoted from  $\mu_0 = 1/a$  to  $\overline{MS}(\mu = 2 \text{ GeV})$  via the perturbative renormalization group functions, today known with four-loop accuracy and implemented in the `RUNDEC.M` package[40].

First, necessary values for  $g_{\overline{MS}}^2(1/a)$  are calculated from the plaquette measurements.  $\square_{\mu\nu}$  is given in eq. (1.14), allowing to obtain

$$u_0 = \left\langle \frac{1}{N_c} \sum_n \text{Re Tr } \square_{\mu\nu}(n) \right\rangle^{1/4} \quad (3.18)$$

entering in the calculation of  $g_{\overline{MS}}^2(1/a)$  given in [42]. Then,  $g_V$  in the intermediate  $V$ -scheme is obtained by solving

$$-\ln(u_0^4) = C_F g_V^2(\mu^*) \left[ 1 - \frac{g_V^2(\mu^*)}{4\pi} \left( \frac{11N_c}{12\pi} \ln\left(\frac{6.7117}{\mu^*}\right)^2 \right) \right] + \mathcal{O}(g_V^6(\mu^*)) \quad (3.19)$$

as given in [43], where also the matching scale  $\mu^*$  is given as  $\mu^* = 3.4018/a$ .  $C_F = 4/3$  is the value of the quadratic Casimir operator. Afterwards,  $g_V^2$  is rescaled to the  $\overline{MS}$ -scheme  $g_{\overline{MS}}^2$ . Values for  $u_0$  and  $g_{\overline{MS}}^2$  can be found in table 3.2,  $g_{\overline{MS}}^2(2 \text{ GeV}) = 2.4288$  is used for the reference scale.

A summary of the staggered quark masses used at different couplings and their values in  $\overline{MS}(\mu = 2 \text{ GeV})$  is given in table 3.3. Since the staggered action is only employed for the calculations of meson screening masses, no mass values for the two high couplings  $\beta = 7.554$  and  $7.793$ , that are only relevant for the thermal dilepton rate calculations have been selected.

### 3.4 Non-perturbative renormalization for the vector current

Local currents, as in eq. (1.41), have to be renormalized after being obtained from lattice QCD calculations. For all analyses in this work, the usage of renormalization constants has been minimized: Meson screening masses are by nature slopes of correlation functions and therefore the constants cancel.

### 3 Scale setting

$\beta$	$\hat{m}_q \cdot a$	$\hat{m}_q$	$m_q$ eq. (3.17)	$m_{\overline{MS}}(\mu = 2 \text{ GeV})$
6.338	$3.864 \cdot 10^3$	13.98	6.74	6.67
6.503	$2.200 \cdot 10^3$	9.94	5.14	5.20
6.640	$1.707 \cdot 10^3$	9.20	4.99	5.15
6.768	$2.000 \cdot 10^3$	12.62	7.10	7.53
6.872	$1.028 \cdot 10^3$	7.36	4.25	4.52
7.192	$4.530 \cdot 10^4$	4.71	2.91	3.18
7.457	$2.500 \cdot 10^4$	3.52	2.27	2.53

Table 3.3: Staggered bare quark masses  $\hat{m}_q$  and their value  $m_{\overline{MS}}$  in the  $\overline{MS}$ -scheme at  $\mu = 2 \text{ GeV}$ , obtained through eq. (3.17) and RUNDEC[40], given in MeV.

Anticipating the presentation in the corresponding chapter, for the thermal dilepton rate calculations ratios of vector correlations functions  $G_V(\tau T)/G_{00}$  and  $G_{ii}(\tau T)/G_{00}$  are selected. Here the same renormalization enters into the numerator and the denominator, so they cancel in the ratio.  $G_{00}$  is constant in Euclidean time and thus can be obtained with high precision. However, a continuum extrapolated value  $G_{00}[a \rightarrow 0]$  has to be found to reverse the ratio in the continuum. Apart from the Wilson quark mass determination in section 3.3.1, this extrapolation is the sole use for the vector channel renormalization constant  $Z_V$  throughout this work.

$Z_V$  has been calculated non-perturbatively in [44] for a wide range of  $\beta$ -values and is parametrised as

$$Z_V(g_0^2) = \frac{1 - 0.7663 g_0^2 + 0.0488 g_0^4}{1 - 0.6369 g_0^2}. \quad (3.20)$$

## 4 Meson screening masses

Meson screening masses are common observables for finite temperature QCD calculations. Along with this study of their thermodynamic and continuum limit in quenched lattice QCD, a range of work is available: Hard thermal loop calculations [45], approaches by dimensional reduction [46] and studies with dynamical (staggered) lattice simulations [47, 48].

The Wilson fermion action with non-perturbative clover improvement as well as the staggered action show discretization effects of the same order  $O(a^2)$ . These cause a deviation of observables (like meson masses) from their continuum limit  $a \rightarrow 0$ , which are introduced by the finite lattice spacing  $a$ . The actions only have in common that the dependence is over all quadratic, thus there is no reason for the discretization errors to share the same prefactors. Also, the effects of the finite lattice volume may differ between Wilson and staggered fermions, so the thermodynamic limit  $V \rightarrow \infty$  has to be taken. In fact, it is found that results on finite lattices differ between both actions when calculations are carried out at finite temperature. This motivated a systematic study of quenched meson screening masses in the thermodynamic and the continuum limit for both actions in the deconfined phase.

### 4.1 Extracting meson masses on finite size lattices

The meson correlator projected to zero momentum eq. (1.42) includes all energy eigenstates as

$$G(n_t) = \sum_k \langle 0 | \hat{O} | k \rangle \langle k | \hat{O}^\dagger | 0 \rangle e^{-n_t m_k} = A_0 e^{-n_t m_0} + A_1 e^{-n_t m_1} + \dots \quad (4.1)$$

The steepness of the exponential fall-off is given by the masses  $m_n$  of the different states. The ground state mass  $m_0$  dominates the correlator for large separations  $n_t$ , while higher mass states mix into the correlator for shorter separations  $n_t$ .

The masses given by the form  $G(n_t) = \sum_k A_k e^{-n_t m_k}$  are the so-called pole masses, where the euclidean correlator is evaluated along the time axis. However, the same expression can be evaluated along one of the spatial axes (axis  $z$  by convention), with

$$G(n_z) = \sum_k A_k^{(z)} e^{-n_z m_k^{(z)}}. \quad (4.2)$$

The resulting masses  $m_k^{(z)}$  are called screening masses, as they are a measure of the inverse of the screening length in the surrounding medium.

## 4 Meson screening masses

The meson screening masses are particularly suitable observables for this study: They are easy to obtain from the correlator with high precision, especially with current computing power, where the relevant spatial extent of quenched lattice calculations in the deconfined phase can easily be varied up to  $N_\sigma > 100$ . Since on a finite lattice with periodic boundary conditions the meson propagation is symmetric in  $n_z$  and  $N_\sigma - n_z$ , the correlator shows a cosh-form along  $n_z$  (the index  $z$  in  $m^{(z)}$  is from now on dropped and all following masses are understood to be screening masses):

$$G(n_z) = 2A_0 e^{-N_\sigma m_0/2} \cosh((N_\sigma/2 - n_z) \cdot m_0) + \dots \quad (4.3)$$

From this form as a general starting point, different methods can be chosen to extract the meson mass from a correlator that has been calculated on the lattice.

### 4.1.1 Effective meson masses

The effective mass is given by directly calculating the steepness of the correlator as a numerical derivative, so it is defined at each distance  $n_{t,z}$  in its most basic form as

$$m_{\text{eff.}}(n_{t,z}) = \log \left( \underbrace{\frac{G(n_{t,z})}{G(n_{t,z} + 1)}}_{\text{numerical derivative}} \right) \quad (4.4)$$

For separations that are large enough to be dominated by the ground state  $E_0$ , a plot of the effective mass, see fig. 4.1. shows a plateau. For smaller separation higher states enter into the correlator and the effective mass rises. For large separations, the cosh-form of the correlator on the lattice causes the mass to fall off<sup>1</sup>.

Unfortunately, on smaller lattices both regions tend to overlap, so finding a stable plateau might not be possible. A solution often implemented is to evaluate the mass at a fixed point, set as a certain ratio of the lattice extent  $N_\sigma$ , for example at  $\frac{1}{4}N_\sigma$  as used in this study: On larger aspect ratios, masses evaluated at  $\frac{1}{4}N_\sigma$  will be on the onset of the plateau. On smaller aspect ratios,  $\frac{1}{4}N_\sigma$  is closer to the source and more of the higher contributions  $m_1, m_2, \dots$  in the correlator are picked up into the effective mass.

These contributions are a form of finite volume effects, though a distinction should be kept in mind: The effect is generated by deliberately picking up relatively more contribution  $m_1, m_2, \dots$  on small lattices than on bigger ones, so they can be removed by extrapolation in the next analysis step. The ground state  $m_0$  itself could additionally be influenced by the finiteness of the lattice, but such an effect could not be found by this analysis.

The effective mass is a handy quantity for Wilson fermions, since it can be directly read off from the correlator. It can also be calculated for staggered fermions, though it has

---

<sup>1</sup> This effect could in principle be compensated by a form of eq. (4.4) including the cosh-term, removing the fall-off but replacing it with large errors at these distances. This would be equivalent to fitting eq. (4.5) to a dataset of two points  $n_z, n_z + 1$ . Moving  $n_z$  towards  $N_\sigma/2$ , the masses would no longer fall off, but the fits would become unstable due to the rising errors.

## 4.1 Extracting meson masses on finite size lattices

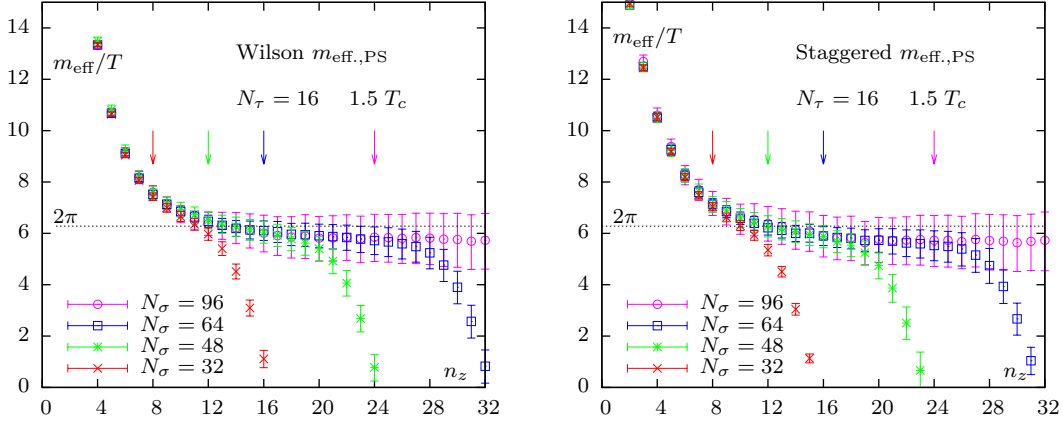


Figure 4.1: Effective pseudoscalar meson screening mass for Wilson (left) and staggered (right) fermions at  $1.5 T_c$  with  $N_\tau = 16$  and different  $N_\sigma$ . The arrows mark  $N_\sigma/4$  for the corresponding lattices, the dotted line marks the free theory mass  $2\pi T$ . On the larger lattices  $N_\sigma \geq 64$ , a clear plateau of the ground state mass is found as soon as  $n_z > N_\sigma/4$ . On the smaller lattice, no such clear plateau can be seen and the choice to evaluate the effective mass at  $N_\sigma/4$  is by convention.

a drawback for that action: Since an oscillating and a non-oscillating contribution enter into (all but one) staggered correlator channels, the effective mass picks up contributions from both particle states (see fig. 4.2). If the energies of both contribution differ enough between the oscillating and non-oscillating channel, they cause one contribution to fall off much steeper with  $n_{t,z}$  than the other. In this case, the effective mass can still be read off precisely enough. However, for channels in which the energies for the oscillating and non-oscillating contribution are similar, the fluctuations of the effective mass between even and odd points are too high. Here a more complex ansatz than eq. (4.4) is needed.

### 4.1.2 Masses extracted through a fit

A more convenient method to extract meson masses, especially from staggered correlators, is to fit eq. (4.3) to a correlator measured on the lattice. As mentioned, for large enough distances  $n_z$  the ground state dominates the correlator, so the first term in eq. (4.3)

$$G(n_z) = \underbrace{2A_0 e^{-N_\sigma m_0/2}}_{\text{Amplitude}} \cosh((N_\sigma/2 - n_z) \cdot m_0) = A'_0 \cosh((N_\sigma/2 - n_z) \cdot m_0) \quad (4.5)$$

with the two free parameters  $A'_0$  and  $E_0$  can be used in the fit.

Care has to be taken in selecting an appropriate fit window  $n'_z \dots N_\sigma - n'_z$ . A window that is too small will result in a bad signal, especially on lattices with small aspect ratios. A window that is too large will pick up much more than the ground state and result in masses that are too high.

#### 4 Meson screening masses

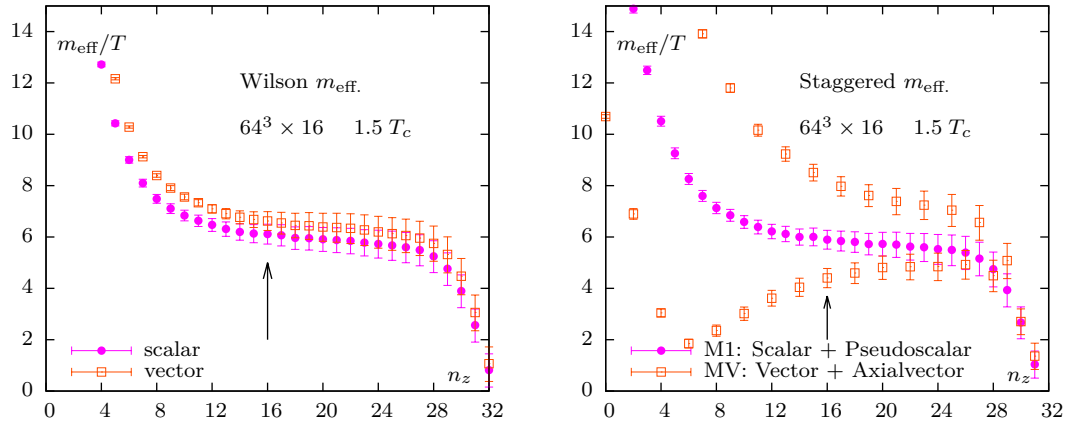


Figure 4.2: Effective screening mass on a  $64^3 \times 16$  lattice at  $1.5 T_c$ . The arrow marks the position  $N_\sigma/4$  as the onset of the ground state mass plateau. The Wilson scalar and vector channel are shown on the left. The staggered channel M1 (shown on the right) is clearly dominated by the scalar contribution, while an additional pseudoscalar contribution could enter as a parity partner. The staggered channel MV is dominated by the vector contribution but clearly picking up contributions from the axial-vector parity partner. The abbreviations refer to the staggered channels as given in table 1.2,  $MV$  denotes a summation of the channels  $MV = M6 + M7$  that are dominated by the vector contribution.

Varying the fit window can be used to find a plateau for screening masses on lattices with a large extent, e.g.  $N_\sigma = 64, 96, \dots$ , in the same way as for effective masses. The mass will level off and indicate that the fit has stabilized at one state as soon as a certain separation  $n'_{z,\min}$  from the source is reached.

In principle, this minimal separation necessary to sufficiently exclude higher contributions should hold on all lattices with the same spacing and temperature. However, an appropriate  $n'_{z,\min}$  fixed by this procedure on a large lattice will often be unusable on a smaller lattice, because it is too close to or even exceeds  $\frac{1}{2}N_\sigma$  on a small lattice. On these small aspect ratio lattices, it is therefore inevitable to pick up contributions from excited states in the fit.

In this sense the one-state fits mimic the behavior of the effective masses and the same solution can be applied: The contributions from higher states are removed in the next step of the analysis by extrapolating towards the thermodynamic limit. Now the requirement for  $n_z$  is to be chosen in a consistent way while ideally still reaching the ground state plateau for large  $N_\sigma$ . A common choice also employed in this analysis is to set  $n_z = N_\sigma/4$ , motivated by ground state plateau onset on larger lattices.

The fit-approach has a big advantage when analyzing staggered correlators that include oscillating and non-oscillating components: By including both ground states into eq. (4.3), two particles can be fitted simultaneously.

$$\begin{aligned}
 G^{\text{stagg.}}(n_z) &= \underbrace{2A_0^{\text{no}} e^{-N_\sigma E_0^{\text{no}}/2} \cosh((N_\sigma/2 - n_z) \cdot m_0^{\text{no}})}_{\text{non-oscillating}} \\
 &+ \underbrace{(-1)^{n_z} \cdot 2A_0^{\text{os}} e^{-N_\sigma m_0^{\text{os}}/2} \cosh((N_\sigma/2 - n_z) \cdot m_0^{\text{os}})}_{\text{oscillating}} + \dots \\
 &= A_0^{\prime,\text{no}} \cosh((N_\sigma/2 - n_z) \cdot m_0^{\text{no}}) + (-1)^{n_z} A_0^{\prime,\text{os}} \cosh((N_\sigma/2 - n_z) \cdot m_0^{\text{os}}) \quad (4.6)
 \end{aligned}$$

As for the Wilson case, care has to be taken in choosing the fit window, but the situation is now more complicated: On the one hand, small lattice extents  $N_\sigma$  still cause problems, even more so since the fit now has four free parameters,  $A_0^{\prime,\text{no}}, E_0^{\text{no}}, A_0^{\prime,\text{os}}, E_0^{\text{os}}$ . Additionally, since the  $m_0^{\text{no}}$  and  $m_0^{\text{os}}$  may differ, one state falls off steeper with  $n_z$  than the other. If the fit window is too small, one state is no longer picked up by the fit because its contribution is lost in the (statistical) noise of the state with the lower  $m_0$ . Both effects forbid using too narrow fit windows, so contributions from higher excited states again have to be removed in the infinite volume extrapolation. Fortunately, the generic choice of  $N_\sigma/4$  still works and thereby holds for these more involved staggered fits. In figure fig. 4.3 an example of a correlator fit is shown for the vector channel of both actions on a small lattice, where the oscillation can be observed very clearly.

### 4.1.3 Extracting the ground state mass by fitting multiple states

While it is possible to take the thermodynamic limit in order to extract the ground state, a second approach is to directly separate ground and excited states when fitting the correlator on the finite size lattices. On the one hand, this offers a cross-check: After

#### 4 Meson screening masses

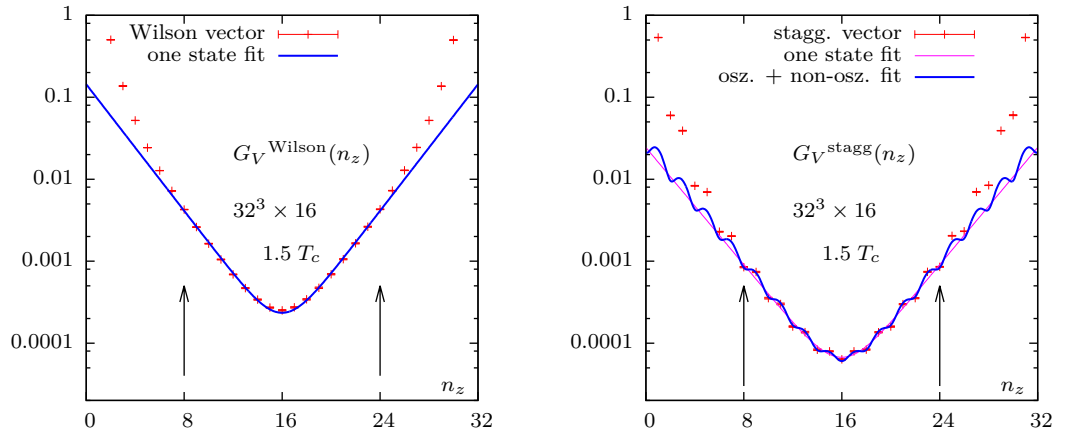


Figure 4.3: A fit to the vector correlation function measured on a  $32^3 \times 16$  lattice at  $1.5 T_c$ . Wilson correlator (left) fitted with eq. (4.5), and staggered correlator (right) with an additional oscillating ground state contribution through eq. (4.6). The arrows mark the fit window  $\frac{1}{4}N_\sigma \dots \frac{3}{4}N_\sigma$ .

reaching a certain physical volume that allows to extract the ground state, the result should no longer vary with raising lattice volume. On the other hand, a thermodynamic limit is often an expensive calculation in terms of computing costs, since large aspect ratios are needed to take the limit. Being able to extract correct ground state results on moderate aspect ratios will thus reduce computing times.

To perform the two-state fit, an additional term for an excited state is introduced to the ansatz as

$$G(n_z) = \underbrace{A'_0 \cosh((N_\sigma/2 - n_z) \cdot m_0)}_{\text{Ground state}} + \underbrace{A'_1 \cosh((N_\sigma/2 - n_z) \cdot m_1)}_{\text{First excited state}} \quad (4.7)$$

Now the fit window can be set to include much more data points of the correlator, e.g.  $[N_\tau/2, N_\sigma - N_\tau/2]$ : Varying the window still shows that with lower distances  $n_z$  contributions from higher excited states  $m_2, m_3, \dots$  enter into the correlator. However (see fig. 4.4), these contributions do not change the ground state mass, but are picked up as a contribution to  $m_1$ . This fit method is convenient especially for medium sized lattice extents  $N_\sigma/N_\tau \sim 4$ , where now a clear enough plateau for a ground state  $m_0$  can be found.

As a more technical side note, checks for correct convergence should be done when performing these fits. To automate the process, it is useful to start from a large enough fit window to extract sensible starting parameters, afterwards reducing the window step by step to its final size. Datasets like those shown in fig. 4.4 can then be extracted as a by-product of this algorithm.

For staggered fermions, an ansatz allowing an excited state for both the oscillating and the non-oscillating contribution would give eight free parameters and would need a

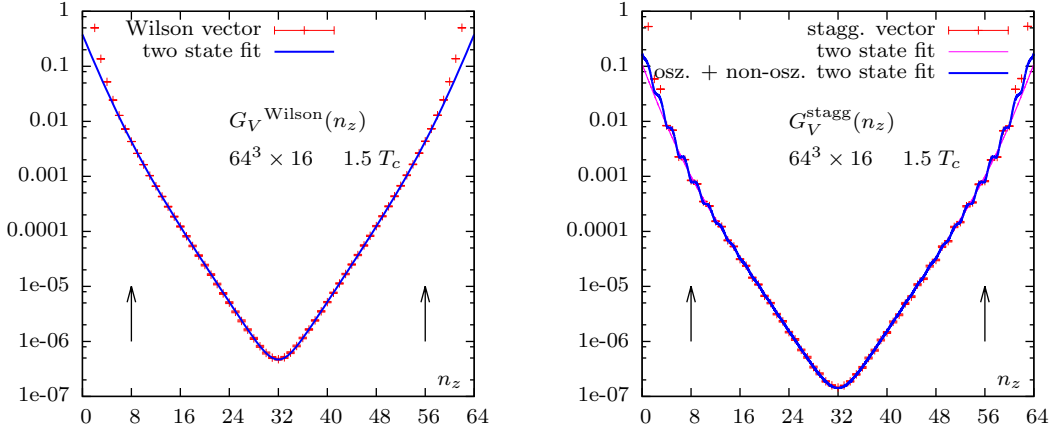


Figure 4.4: A two-state fit to the vector correlation function measured on a  $64^3 \times 16$  lattice at  $1.5 T_c$ . Wilson correlator (left) fitted with eq. (4.7), and staggered correlator (right) with an additional oscillating ground state contribution through eq. (4.9). The arrows mark the fit range  $N_\tau/2$  to  $N_\sigma - N_\tau/2$ .

very clean, noise-free dataset to be successfully fitted. Instead, it is useful to only allow an excited state for the dominating contribution in a correlator channel, reducing the number of parameters to six. For example, if the oscillating contribution dominates for larger distances  $n_z$ , the ansatz would be

$$G(n_z) = (-1)_z^n \left( \underbrace{A_0^{\prime, \text{os}} \cosh((N_\sigma/2 - n_z) \cdot m_0^{\text{os}})}_{\text{Oscil. ground state}} + \underbrace{A_1^{\prime, \text{os}} \cosh((N_\sigma/2 - n_z) \cdot m_1^{\text{os}})}_{\text{Oscil. first excited state}} \right) \quad (4.8)$$

$$+ \underbrace{A_1^{\prime, \text{no}} \cosh((N_\sigma/2 - n_z) \cdot m_0^{\text{no}})}_{\text{any non-oscillating state}} \quad (4.9)$$

In the following, fits only taking into account one ground state, given by eqs. (4.5) and (4.6) are referred to as *one-state fits*. Fits allowing for an additional excited state, given by eqs. (4.7) and (4.9) are referred to as *two-state fits*. This definition is important for the staggered action, as here *one* and *two* denote the number of states in the dominating channel, and an additional second or third state can enter for the parity partner.

## 4.2 A study at $1.5 T_c$ and $3.0 T_c$

Two temperatures in the deconfined phase  $1.5 T_c$  and  $3.0 T_c$  were chosen for this study. For the low temperature, a set of five aspect ratios  $N_\sigma/N_\tau = 2, 3, 4, 6, 8$  allows to take the thermodynamic limit, while four lattice extents  $N_\tau = 8, 10, 12, 16$  were picked for the continuum extrapolation. This yields 20 combinations  $N_\sigma \times N_\tau$ . For the high temperature, a reduced set of four aspect ratios  $N_\sigma/N_\tau = 2, 3, 4, 8$  and three extents

#### 4 Meson screening masses

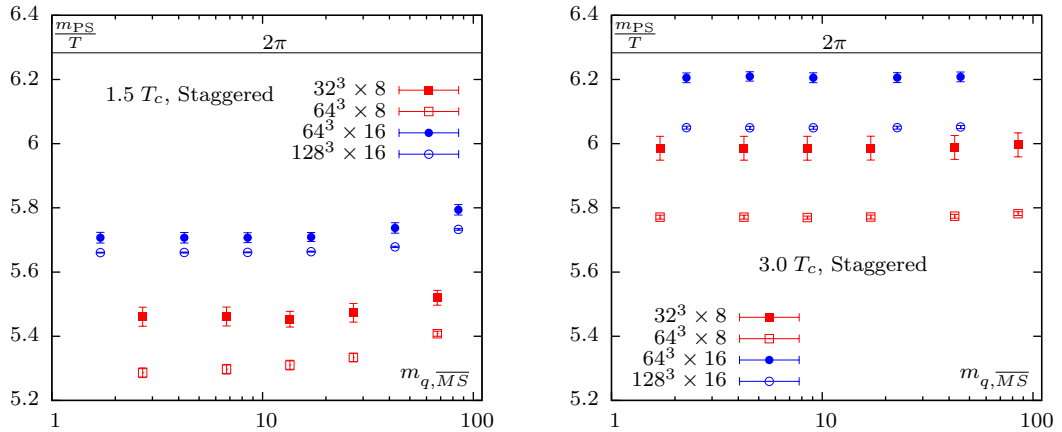


Figure 4.5: Staggered pseudoscalar screening masses for different quark masses  $m_{q, \overline{MS}}(\mu = 2 \text{ GeV})$  (see eq. (3.17)), at both  $1.5 T_c$  (left) and  $3.0 T_c$  (right) and for different lattice sizes. The masses are obtained by fits of eq. (4.6) with a fit range of  $\frac{1}{4} N_\sigma \dots \frac{3}{4} N_\sigma$ . Within errors, no dependence of the meson screening mass on the quark masses is found for  $m_{q, \overline{MS}}(\mu = 2 \text{ GeV}) < 25 \text{ MeV}$ .

$N_\tau$	$N_\sigma$	$\beta$	$\kappa_{\text{Wilson}}$	$C_{\text{SW}}$	$m_q^{\text{stagg}}$
8	16, 24, 32, 48, 64	6.338	0.13572	1.548725	0.003864
10	20, 30, 40, 60, 80	6.503	0.13554	1.493023	0.002190
12	24, 36, 48, 72, 96	6.640	0.13536	1.457898	0.001707
16	32, 48, 64, 96, 128	6.872	0.13495	1.412488	0.001028

Table 4.1: Simulation parameters for meson screening masses at  $1.5 T_c$ .

$N_\tau = 8, 12, 16$ , with a total of 12 lattice sizes  $N_\sigma \times N_\tau$ , proved to be sufficient for the analysis.

For each  $N_\tau$ , the  $\beta$ -value was tuned to match a lattice spacing corresponding to the temperature (see section 3.1). As a further parameter, the influence of the quark mass on the meson screening masses was checked. Light quark masses were used for both actions. The procedure of obtaining these masses, especially for the Wilson action, is laid out in section 3.3. For quark masses  $m_{q, \overline{MS}}(\mu = 2 \text{ GeV}) < 25 \text{ MeV}$  no noticeable effect on the meson screening masses could be found, see fig. 4.5. A summary of all simulation parameters can be found in tables 4.1 and 4.2.

The full analysis was carried out at a temperature of  $1.5 T_c$ , with one- and two-state fits performed for each lattice size. On the smaller dataset at  $3.0 T_c$ , only one-state fits were performed. For the staggered scalar and pseudoscalar channels, it is found that the contribution of the parity partner was suppressed enough so that it did not affect the fit. For the vector and axial-vector however, both the one- and the two-state fits had to allow for an additional contribution from an oscillating or non-oscillating state in the

$N_\tau$	$N_\sigma$	$\beta$	$\kappa_{\text{Wilson}}$	$C_{\text{SW}}$	$m_q^{\text{stagg}}$
8	16, 24, 32, 64	6.872	0.13495	1.412488	0.001028
12	24, 36, 48, 96	7.192	0.13440	1.367261	0.000453
16	32, 48, 64, 128	7.457	0.13390	1.338927	0.000250

Table 4.2: Simulation parameters for meson screening masses at 3.0  $T_c$ .

correlator.

### 4.2.1 The thermodynamic limit

Obtaining the screening masses from the one-state fits eqs. (4.5) and (4.6), with a fit window fixed to a certain ratio of the spatial lattice extent, for example  $\frac{1}{4}N_\sigma \dots \frac{3}{4}N_\sigma$ , the fit will not pick up a pure ground state. Instead contributions from higher states will enter into the fit, especially on lattices with smaller aspect ratios where  $\frac{1}{4}N_\sigma$  is in closer proximity to the source.

To compensate for this effect, the thermodynamic limit  $N_\sigma \rightarrow \infty$  has to be taken to arrive at the infinite volume ground state mass. The volume dependence is linear in the inverse aspect ratio  $N_\tau/N_\sigma$  for the free theory, while zero temperature simulations show the mass at finite volume to scale with the third power of the spatial lattice extend [49].

For finite temperature, it is therefore sensible to choose

$$m_{N_\sigma/N_\tau} = m_{N_\sigma \rightarrow \infty/N_\tau} (1 + b_{N_\tau} \cdot (N_\tau/N_\sigma)^c) \quad (4.10)$$

as an ansatz for the fit, with three free parameters  $m_{N_\sigma \rightarrow \infty/N_\tau}$ ,  $b_{N_\tau}$  and  $c$ . With a linear relation to the lattice volume for the free theory and a cubic dependence at zero temperature, the exponent  $c$  is to be expected to fall within 1 and 3 at finite temperature.

Since a continuum extrapolation  $a \rightarrow 0$  will also be carried out, the thermodynamic limit is taken separately for different lattice spacings  $a$ . At a fixed finite temperature these map to a set of temporal lattice extends, e.g.  $N_\tau = 8, 12, \dots$ . As indicated by the index,  $b_{N_\tau}$  is allowed to vary for different  $N_\tau$ , while the exponent  $c$  should only depend on the temperature and the fermion action. Performing the fit for the thermodynamic limit for all  $N_\tau$  in a combined fit, with one shared free parameter  $c$ , reduces the total number of free parameters and stabilizes the fit. A crosscheck of this assumption can be performed if enough points for a stable fit are available on single lattice spacings.

This technique is applied to the 1.5  $T_c$  dataset: All 20 data points from 5 aspect ratios at 4 different lattice spacings enter into a fit of the ansatz eq. (4.10), with a common exponent  $c$  for all lattice spacing. In fig. 4.7 the result of these fits for both actions are shown. It also holds (as thin lines) two fits in which the exponent  $c$  was determined with

$N_\tau$	Wilson	stagg.
12	2.47(50)	2.08(25)
16	2.31(36)	3.46(35)
all	2.06(23)	2.36(35)

Table 4.3:  $c$  for the pseudo-scalar at 1.5  $T_c$ , see eq. (4.10).

the 5 data points from  $N_\tau = 12$  and  $N_\tau = 16$  lattices only, to crosscheck if the procedure to fix the exponent as independent of the lattice spacing is correct.

Exemplary result for  $c$  obtained for the pseudo-scalar channel at  $1.5 T_c$  are provided in table 4.3. The staggered result limited to the  $N_\tau = 16$  dataset is an outlier. It is likely caused by a quite low mass on the  $64 \times 16$  lattice, with an underestimated error entering into the weighted fit. Otherwise all exponents all well compatible to the average  $c = 2.21(41)$ , which also lies in the expected region of  $c = 1 \dots 3$ .

#### 4.2.2 Ground state extracted from multiple state fits on finite lattices

The finite volume effects removed by taking this thermodynamic limit are (as laid out for the effective masses) in a sense artificially introduced: Most of the contribution enters due to the fact that the fit window is set to a fixed portion of the lattice,  $\frac{1}{4}N_\sigma \dots \frac{3}{4}N_\sigma$ . The fit will pick up more contributions from higher states  $E_1, E_2, \dots$  with decreasing aspect ratio, because  $N_\sigma/4$  moves closer to the source with decreasing  $N_\sigma$ .

This allows for an alternative: A ground state mass can be found by performing the two-state fits eqs. (4.7) and (4.9). The fit window of  $\frac{1}{2}N_\tau \dots N_\sigma - \frac{1}{2}N_\tau$  ensures that a constant distance to the source is maintained for all aspect ratios and lattice spacings, since for a constant temperature  $\frac{1}{2}N_\tau$  translates to a constant distance in physical units.

To test the procedure, the fit window is varied around  $\frac{1}{2}N_\tau$ . In fig. 4.6, masses for different fit window sizes for both the one-state and the two-state fits are shown. The mass found by one-state fits is clearly influence by the fit window size, where the mass raises towards the source. This is expected, as it is in agreement with the behaviour for effective masses. For the two-state fits, the second state seems to absorb the higher contributions, while the ground state is mostly unaffected and stable over a wider region of fit window sizes. Thus, the two-state fit procedure seems to be capable of extracting stable ground state masses.

This procedure fails for very small aspect ratios ( $N_\sigma/N_\tau = 2, 3$ ), where the system is too small to show a clear ground state. A minimal aspect ratio of  $N_\sigma/N_\tau = 4$  seems to suffice for larger  $N_\tau = 12, 16$ , while  $N_\sigma/N_\tau = 6, 8$  give more precise results, especially on coarse lattices  $N_\tau = 8, 10$ .

Fit results from the two-state fits show no clear dependence on the aspect ratio for  $N_\sigma/N_\tau \geq 4$ . Thus they are averaged, with results given in fig. 4.8. For the pseudo-scalar and scalar channels as well as all staggered channels, results from the two-state fits are compatible with the thermodynamic limit of one-state fits shown in fig. 4.7.

For the Wilson vector and axial-vector channel, results from the one-state fits are somewhat lower then from the two-state fits. Looking ahead on the final comparison of both actions, the Wilson two-state fits are compatible with the staggered results for the vector and axial-vector channel, while the one-state fits are too low. It can be assumed that the thermodynamic limit overestimated the finite volume contributions, thus the extrapolation reaches an infinite volume mass that is too low.

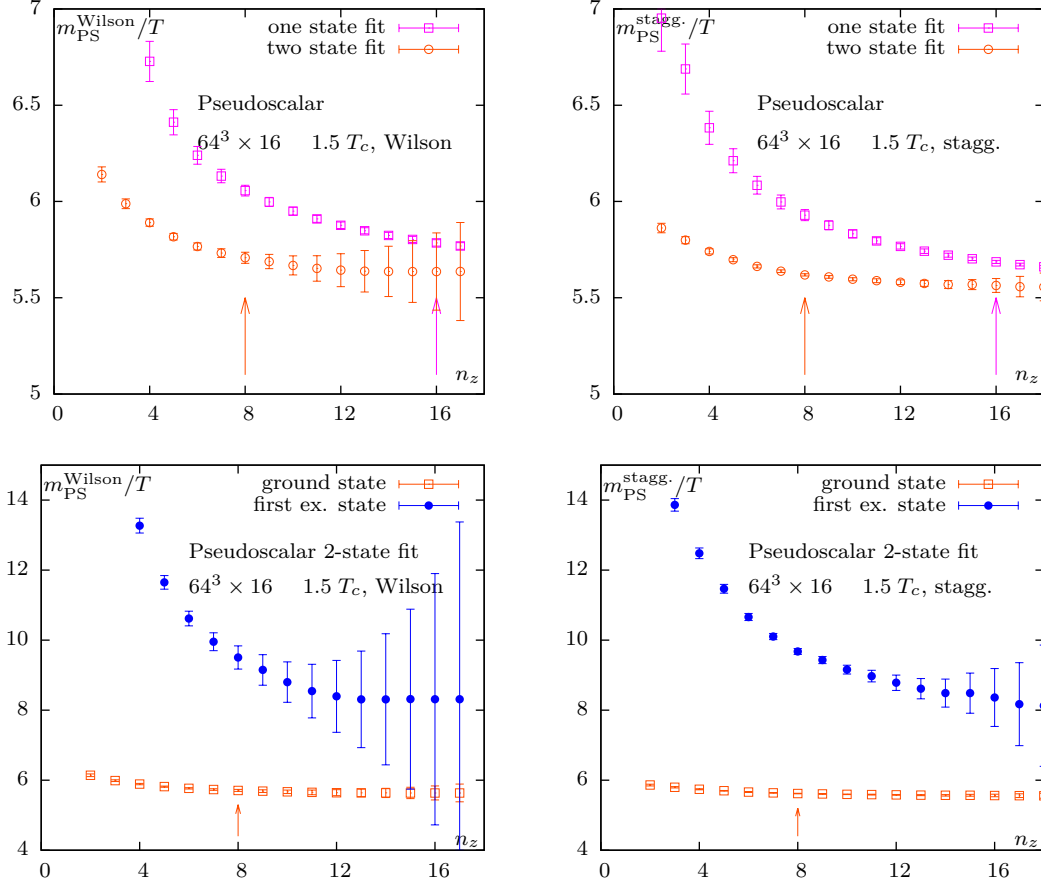


Figure 4.6: Wilson (left) and staggered (right) pseudo-scalar screening masses, obtained at  $1.5 T_c$  on  $64^3 \times 16$  lattices, for different sizes  $n_z \dots N_\sigma - n_z$  of the fit window. In the upper row, the ground state results of the one- and two-state fits are compared, where the one-state fits show a much higher dependence on the fit window size. In the lower row, the ground state and the excited state of the two-state fits are compared, showing that when increasing the fit window size, higher contributions mainly enter into the excited state, while the ground state is mostly unaffected. The arrows mark the fit window position  $n_z$  chosen for the analysis.

#### 4 Meson screening masses

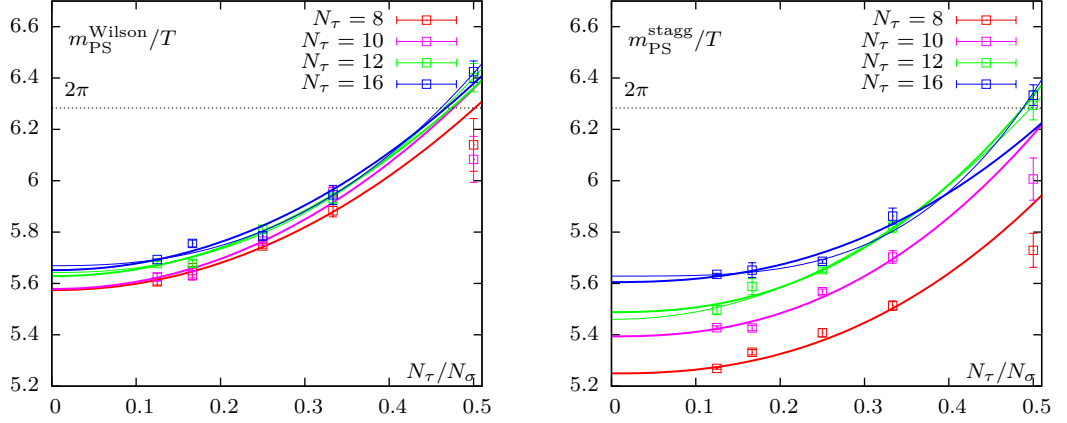


Figure 4.7: Thermodynamic limit obtained by fitting eq. (4.10) to Wilson (left) and staggered (right) pseudoscalar meson screening masses at  $1.5 T_c$ . The thick lines are obtained from a full fit with one shared exponent  $c$  for all lattice spacings. The thin lines are obtained by fits with a dataset limited to  $N_\tau = 12$  and  $N_\tau = 16$  to crosscheck the assumption that the exponent  $c$  is independent of the lattice spacing. The dotted line at  $2\pi$  marks the free theory limit.

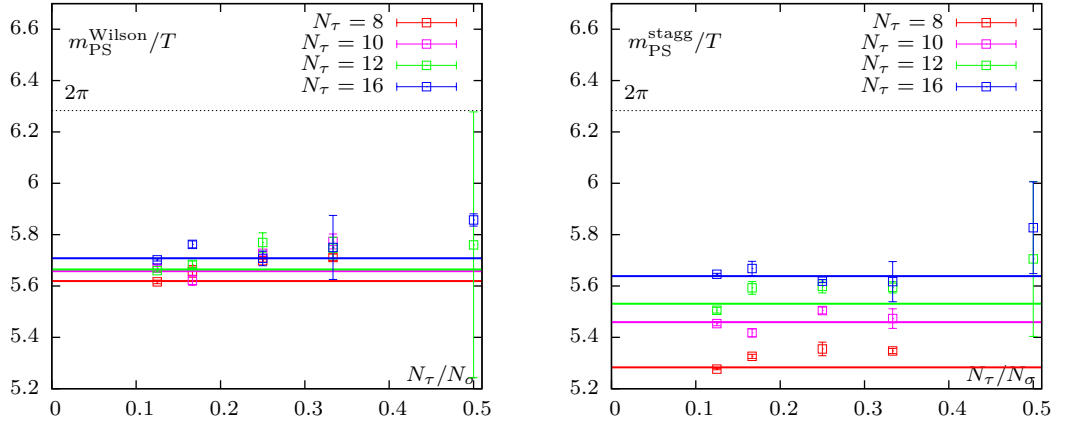


Figure 4.8: Results of the ground state pseudoscalar screening mass obtained from two-state fits (eq. (4.7), eq. (4.9)) for the Wilson (left) and staggered (right) action at  $1.5 T_c$ . The lines mark the masses obtained from weighted averages for  $N_\sigma/N_\tau \geq 4$  on each lattice spacing. The dotted line at  $2\pi$  marks the free theory limit.

### 4.2.3 The continuum limit

Both the clover-improved Wilson action as well as the standard staggered fermion action show  $O(a^2)$  discretization errors. At a fixed temperature, since  $T = 1/(a \cdot N_\tau)$ , the continuum is reached by extrapolating in  $1/N_\tau^2$ , so

$$m_{N_\tau} = m^{\text{cont.}} \cdot \left(1 + d \cdot \frac{1}{N_\tau^2}\right) \quad (4.11)$$

Higher orders as  $O(a^4)$  or  $O(a^2 \ln(a))$  could enter into eq. (4.11), but these contributions seem to be small enough to not influence the results.

As input for  $m_{N_\tau}$ , the y-axis intercepts in fig. 4.7 and fig. 4.8 give the thermodynamic limit of the meson masses for different temporal lattice extents  $N_\tau = 8, 10, 12, 16$ , corresponding to four different lattice spacings  $a$ . The extrapolation results are shown in fig. 4.9.

Comparing Wilson and staggered fermions in these plots, it becomes very apparent that the staggered action yields a much higher dependence on lattice spacing effects, while Wilson fermions seem much less affected. For the Wilson action, the slope  $d$  in ansatz eq. (4.11) is compatible with zero ( $d_S^{\text{Wilson}} = 1.5(6.0)$ ) for the (pseudo)scalar and quite low ( $d_{\text{AV}}^{\text{Wilson}} = -4.9(1.6)$ ) for the (axial)vector channel. For the staggered action, both slopes are much higher than for the Wilson action. Here, the (pseudo)scalar shows a higher lattice spacing dependence ( $d_S^{\text{stagg.}} = -29(1)$ ) than the (axial)vector ( $d_{\text{AV}}^{\text{stagg.}} = -16(4)$ ) channel.

### 4.2.4 Interchanging thermodynamic and continuum limit

The continuum limit can be taken either after performing the thermodynamic limit, reaching the full continuum, or at a fixed aspect ratio, e.g.  $N_\sigma/N_\tau = 3, 4, \dots$ . The thermodynamic limit  $N_\sigma \rightarrow \infty$  for a set of different temporal extents  $N_\tau$  is generally performed first, the continuum limit on the results of thermodynamic extrapolation is taken afterwards.

However, the result can be independent of the order in which the extrapolations are carried out: Varying  $N_\tau$ ,  $N_\sigma$  at a fixed aspect ratio and a fixed temperature keeps the lattices at a fixed physical size, thus in principle introducing the same finite volume effects while varying the discretization errors due to the change in lattice spacing  $a$ . The continuum extrapolation can then be performed on a series of fixed (physical) size lattices and afterwards be extrapolated to the thermodynamic limit.

This interchange of limits was tested on the 1.5  $T_c$  dataset: The continuum extrapolation eq. (4.11) was performed on sets of lattices with the same aspect ratios but varying lattice spacing, e.g. on a series  $N_\sigma/N_\tau = 4$  with  $32^3 \times 8$ ,  $40^3 \times 10$ ,  $48^4 \times 12$  and  $64^3 \times 16$ . Due to the fixed temperature, these lattices have the required constant physical extent. The results of these extrapolations should therefore be free of finite spacing effects, but still carry the finite volume effects introduced by their limited physical size.

In the next step, the volume dependence is removed by the same ansatz eq. (4.10) as above. For the one-state fits, this procedure interchanges both extrapolations. For the

#### 4 Meson screening masses

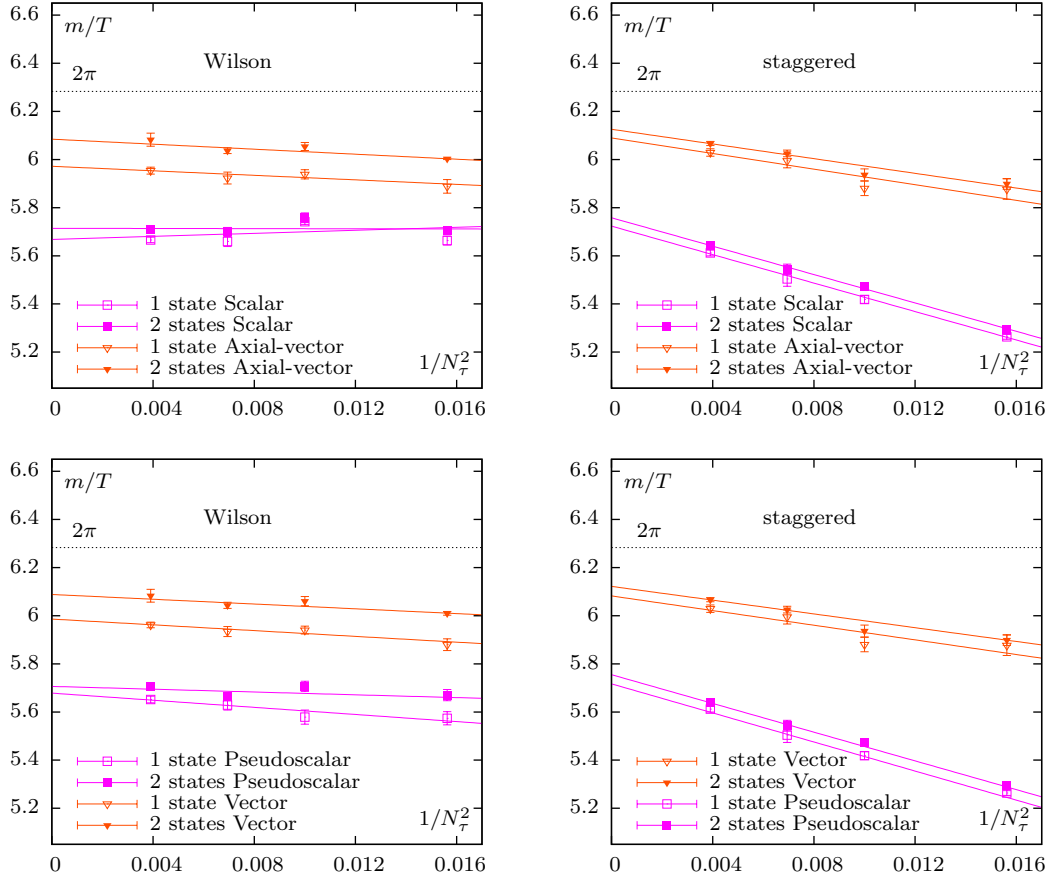


Figure 4.9: Continuum extrapolation using eq. (4.11) of the scalar and axial-vector channels (upper row) and the pseudoscalar and vector channels (lower row), for both Wilson (left) and staggered (right) fermions, at  $1.5 T_c$ . The data points are the result of the thermodynamic limit (infinite volume extrapolation of the one-state fits) and the ground state masses obtained from two-state fits. The dotted line marks the free theory mass of  $2\pi T$ .

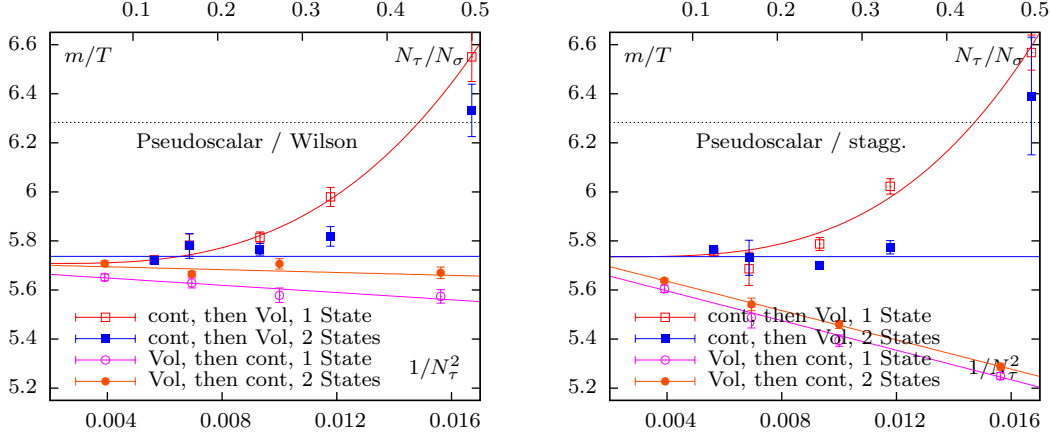


Figure 4.10: Continuum and thermodynamic limit interchanged for Wilson (left) and staggered (right) pseudoscalar screening masses at  $1.5 T_c$ . Data points marked "Vol, then cont." are results of the thermodynamic limit and continuum extrapolated through eq. (4.11) in this figure (lower x-axis). Data points marked "Cont, then Vol" are the results of continuum extrapolations on fixed aspect ratios and extrapolated to infinite volume through eq. (4.10) (upper x-axis).

two-state fits, no finite volume effects are expected as long as a minimal aspect ratio is maintained. Here the procedure interchanges averaging over the results on different aspect ratios and taking the continuum limit. A set of all extrapolations is summarized in fig. 4.10 for the pseudoscalar screening mass. It is found that, within errors, the interchanged limit yields compatible results.

#### 4.2.5 Results at $3.0 T_c$

A subset of the analysis presented so far was performed on the smaller dataset for a temperature of  $3.0 T_c$ . The masses were extracted by one-state fits, extrapolated to the thermodynamic limit through eq. (4.10) and the results were extrapolated to the continuum through eq. (4.11) afterwards. A summary of the results for the pseudoscalar channel. can be found in fig. 4.11 and table 4.5.

The shortened analysis of the  $3.0 T_c$  dataset was motivated by the fact that the  $3.0 T_c$  dataset proved much easier to analyse than the  $1.5 T_c$  dataset: The 3 lattice spacings with 4 aspect ratios each, resulting in 12 data points for the combined fit of eq. (4.10), are enough to provide a stable fit with conclusive result for every particle channel in both actions.

### 4.3 Final results and conclusion

The final results of this study are meson screening masses extrapolated to the thermodynamic and continuum limit, for the pseudo-scalar, scalar, vector and axial-vector

#### 4 Meson screening masses

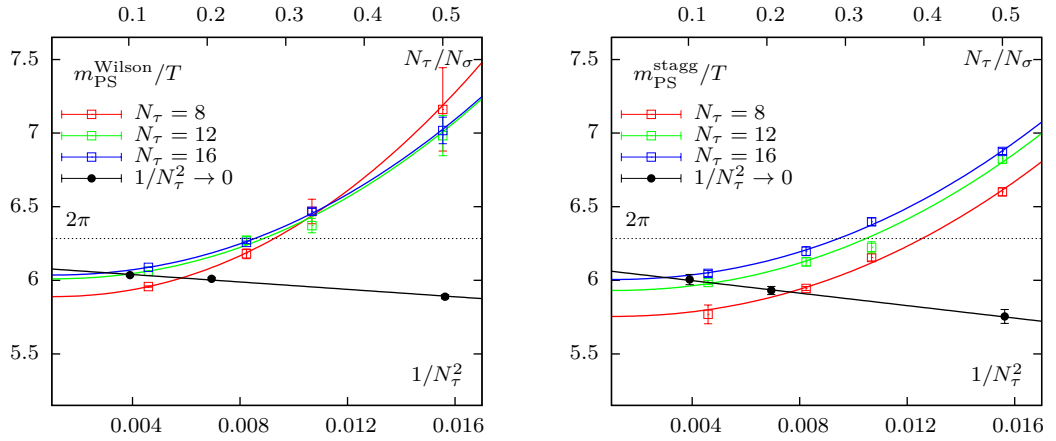


Figure 4.11:  $3.0 T_c$  results for the Wilson (left) and staggered (right) pseudoscalar screening mass. Colored (red, green, blue) lines denote the volume extrapolation eq. (4.10) for  $N_\tau = 8, 12, 16$ , with  $N_\tau/N_\sigma$  set on the lower x-axis. The y-axis intercepts correspond to the extrapolation results, and the black line represents their continuum extrapolation eq. (4.11) with  $1/N_\tau^2$  on the upper x-axis.

channel, for both the Wilson and the staggered action, and at both  $1.5 T_c$  and  $3.0 T_c$ . In fig. 4.12 and tables 4.4 and 4.5 all final data points are summarized, where they allow for a set of observations, concerning on one hand the method and technical details, and on the other hand conclusions about the physical interpretation.

A summary of findings concerning the methodology and the technical details involved can now be given:

- As the staggered action shows much more pronounced lattice spacing effects, the continuum limit is the crucial step in this process. The finite lattice volume has a similar effect in both actions, indicated by their similar exponents  $c$  in the fit of eq. (4.10).
- The thermodynamic limit is reached by extrapolation through ansatz eq. (4.10) or by fitting multiple states to a correlator on a reasonably sized lattice. For the vector and axial-vector in the Wilson action, the former method yields results that are somewhat too low, which indicates that the fit overestimates volume effects. For the staggered action and both actions in the pseudoscalar and scalar channel all results are consistent.
- The multiple state fits at larger  $N_\tau = 12, 16$  reach results compatible to the full thermodynamic limit already at aspect ratios of  $N_\sigma/N_\tau = 4$ . If this holds for other temperatures and actions, it might help to reduce the lattice sizes and thereby computing cost needed in screening masses studies. With the continuous increase in computing power, today dynamical calculations are becoming feasible on  $48^3 \times 12$

### 4.3 Final results and conclusion

Channel	$N_\tau$	Wilson		staggered	
		1 state	2 states	1 state	2 states
PS	8	5.574(27)	5.670(23)	5.250(13)	5.288(13)
	10	5.579(29)	5.707(21)	5.394(22)	5.460(16)
	12	5.629(20)	5.665(10)	5.488(42)	5.541(25)
	16	5.652(14)	5.708(10)	5.605(15)	5.638(7)
	$\infty$	5.678(13)	5.706(30)	5.717(16)	5.755(4)
S	8	5.663(18)	5.706(10)	5.263(9)	5.294(9)
	10	5.742(11)	5.758(1)	5.419(16)	5.472(10)
	12	5.660(20)	5.701(16)	5.504(30)	5.543(22)
	16	5.666(11)	5.710(11)	5.612(12)	5.641(8)
	$\infty$	5.668(57)	5.751(64)	5.723(8)	5.758(8)
V	8	5.883(39)	6.010(7)	5.877(42)	5.899(22)
	10	5.942(30)	6.060(19)	5.880(29)	5.937(24)
	12	5.942(35)	6.043(12)	5.995(29)	6.025(13)
	16	5.964(24)	6.083(26)	6.029(15)	6.067(8)
	$\infty$	5.991(13)	6.088(20)	6.090(33)	6.126(15)
AV	8	5.890(44)	6.003(3)	5.885(39)	5.904(22)
	10	5.943(33)	6.054(16)	5.887(28)	5.951(27)
	12	5.936(40)	6.037(11)	5.989(32)	6.032(17)
	16	5.961(27)	6.083(27)	6.027(15)	6.066(7)
	$\infty$	5.983(14)	6.085(21)	6.082(32)	6.122(10)

Table 4.4: Summary of the final extrapolation results at  $1.5 T_c$ .

4 Meson screening masses

Channel	$N_\tau$	Wilson	staggered
PS	8	5.889(13)	5.754(46)
	12	6.010(9)	5.931(27)
	16	6.036(8)	6.005(35)
	$\infty$	6.089(11)	6.083(9)
S	8	5.877(13)	5.756(32)
	12	6.006(9)	5.931(23)
	16	6.026(8)	6.006(29)
	$\infty$	6.083(16)	6.082(10)
V	8	6.060(39)	6.025(98)
	12	6.180(17)	6.134(58)
	16	6.204(16)	6.219(53)
	$\infty$	6.255(14)	6.272(34)
AV	8	5.982(26)	6.025(98)
	12	6.167(19)	6.134(58)
	16	6.190(18)	6.219(53)
	$\infty$	6.274(29)	6.272(34)

Table 4.5: Summary of the final extrapolation results at  $3.0 T_c$ .

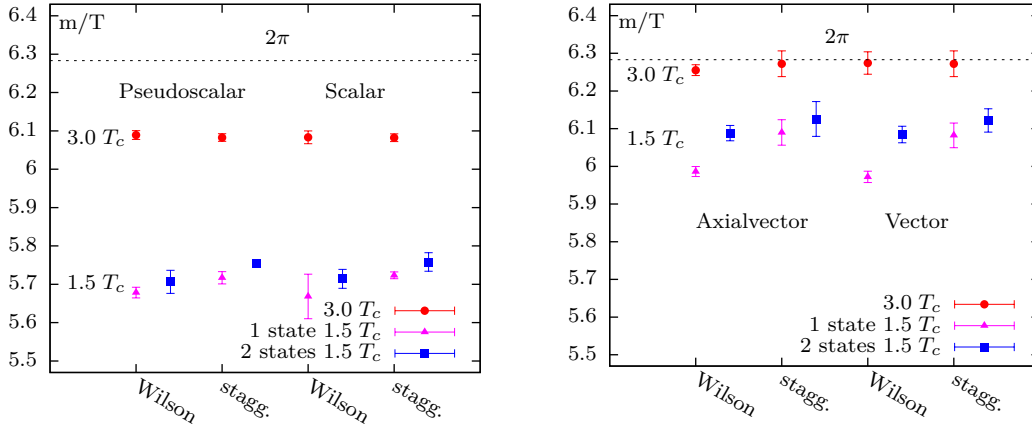


Figure 4.12: Final dataset after thermodynamic and continuum limits of the meson screening masses.

and even  $64^3 \times 16$  lattices, where  $N_\sigma/N_\tau \geq 4$  holds and this analysis might be carried out.

- The thermodynamic limit and the continuum limit can be interchanged, performing a continuum limit on a set of fixed aspect ratio lattices first and the extrapolation to infinite volume afterwards. This can serve as an important crosscheck in the analysis and also allows to calculate continuum extrapolated results at finite volumes. This method also seems to overestimate the volume effects for the Wilson vector and axial-vector channel.
- As more of a practical side-note than a quantifiable fact, it is also found that running this analysis became much more involved at the lower temperature of  $1.5 T_c$ , needing a larger set of lattice spacings, aspect ratios and overall statistics in the correlator analysis. The analysis at  $3.0 T_c$ , closer to the free theory, proved easier and more consistent at a much earlier point.

The meson masses acted as a suitable observable for answering the initial question of differences between Wilson and staggered fermions, and allowed to develop the framework introduced to extract consistent continuum results. There is also an important physical interpretation of these results:

- Differences between both actions on finite lattices vanish when the ground state masses are extracted (by taking the thermodynamic or performing a two-state fit) and the continuum limits are carried out.
- Both the pseudoscalar and the scalar masses as well as the vector and the axialvector mass are clearly degenerate at both temperatures  $1.5 T_c$  and  $3.0 T_c$ . This holds not only for the continuum extrapolation, but already for finite size lattices.

#### 4 Meson screening masses

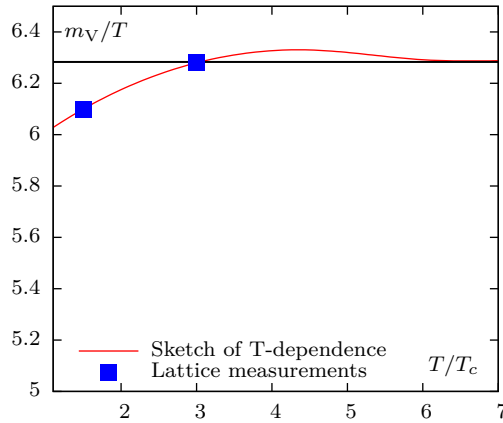


Figure 4.13: An illustrating sketch of an expected temperature dependence of meson screening masses. With increasing temperature, the masses start from below  $2\pi T$ , cross the  $2\pi T$  line at some point (here  $3.0 T_c$  for the vector channel), rise further, level off and finally approach  $2\pi T$  from above.

This degeneracy is expected in the  $U_A(1)$ -restored phase; the caveat here is that the Wilson action breaks chiral symmetry explicitly and the study is performed in the quenched approximation.

- Both HTL and dimensional reduction [45, 46] currently predict the free theory meson screening masses  $2\pi T$  to be reached from above, for both the (pseudo)scalar and the (axial)vector. At  $1.5 T_c$ , none of the masses reach this free theory limit, they are both clearly below. For  $3.0 T_c$ , all masses are closer to  $2\pi T$  and the vector and axial-vector are compatible with  $2\pi T$ . A sketch of a possible temperature dependence, where the masses rise further with growing temperature and then reach  $2\pi T$ , is given in fig. 4.13. However, the analytic results currently available are truncated, so higher order contributions might easily change the expected temperature dependence.
- The free theory also predicts a full degeneracy between scalar, vector, pseudoscalar and axialvector, so a common mass for all four channels should be seen when approaching the free limit. However, this is not observed at either temperature. Taking into account the last point and fig. 4.13, neither  $1.5 T_c$  nor  $3.0 T_c$  can be considered a temperature close to the free theory.

## 5 Thermal dilepton rates

Thermal dileptons are an important observable to study the strongly interacting medium of a quark-gluon-plasma near the phase transition temperature. As mentioned in the introduction, a QGP is produced in heavy ion collisions, thus allowing for experimental studies of its properties. Theoretical predictions of medium properties as transport coefficients and the dilepton rates studied in this work closely accompany these studies, so advancements in experimental and theoretical understanding are tightly linked. Therefore, a short overview of the experimental and theoretical state of heavy ion collisions and the role of dileptons is given below. As a starting point for more in-depth reading, a brief but very recent overview on heavy ion collisions and the theoretical considerations involved is provided in [50], and an extensive review of dilepton rates in heavy ion collision is found in [51].

### 5.1 Heavy ion collisions and thermal dileptons

The current heavy ion experiments at RHIC and LHC are able to produce a QGP with a temperature of  $T = 221(19)$  MeV at RHIC[54, 55] and  $T = 304(51)$  MeV at LHC[56], see fig. 5.2. The temperatures given here are determined from direct photon measurements, thus they pose a lower limit on the temperatures reached in the QGP. The initial temperatures of the QGPs will be higher, but cannot be probed directly. They have to be extracted from models of the QGP evolution, so their values largely depend on the choice of model parameters[55].

After the initial collision, the QGP is expected to then thermalize. Afterwards it cools down further till finally the hadrons bind and freeze out, see fig. 5.1 for a sketch. Whether the region marked *mixed phase* in the sketch exists is linked to the form of the QCD phase diagram, that is if it features a cross-over or a phase transition. This matter is subject to active research.

Dileptons and photons are produced in the QGP. They serve as an important experimental observable, as they escape the QGP mostly unaffected after being generated. Thereby they allow to study the medium properties, see [57, 58] and the sketch in fig. 5.1.

The dilepton rates measured by the two experiments PHENIX and STAR at the RHIC collider are given in fig. 5.3. The enhancement of the measured dilepton rate over the cocktail model predictions in the region  $M_{ll} = 150 \dots 750$  MeV is presumed to relate to QGP contributions. This motivates to find acquire in-depth understanding of the QGP properties, especially the contribution of the vector meson to the dilepton rate at different temperatures.

Different theoretical models are used to describe the evolution of the QGP and predict the rates for dileptons from different production processes, their yields and invariant

## 5 Thermal dilepton rates

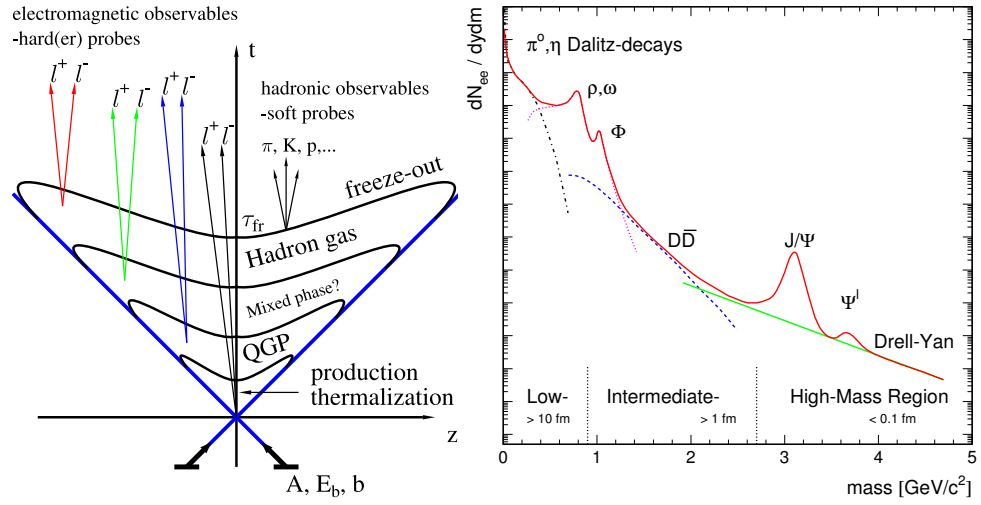


Figure 5.1: Sketch of the phases of a heavy ion collision (left, [52]). Sketch of the contribution of different dilepton production processes in relation to invariant masses (right, [53]).

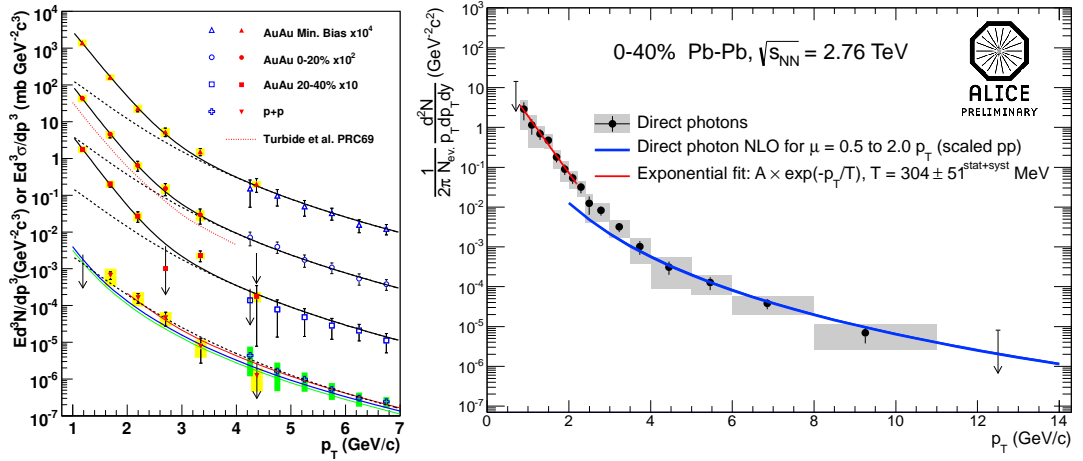


Figure 5.2: Direct photon measurements at the RHIC PHENIX experiment (left plot, [54]) and the LHC Alice experiment (right plot, [56]). The inverse slope of the exponential fits determines the temperature.

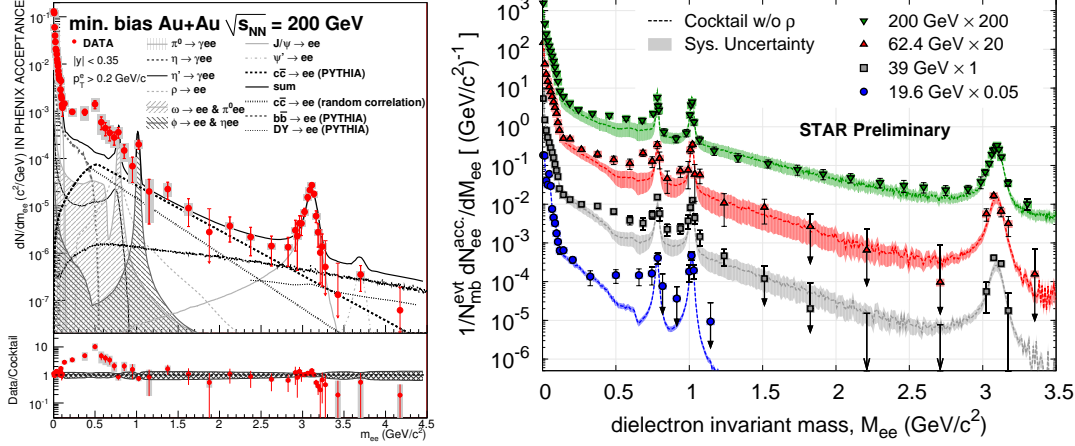


Figure 5.3: Dilepton rates measured by the PHENIX (left, [55]) and STAR (right, [59]) experiment, Au+Au heavy ion collisions.

masses. Today these models have become rather extensive and complex, for current reviews see [53, 60, 61].

These models depend on medium properties, e.g. transport coefficients, as input, so obtaining precise theoretical predictions of these parameters is worthwhile. At high temperatures, hard thermal loop (HTL) approaches, see e.g. [62], can be used to this end. However, they break down as the temperature approaches the phase transition, see [63] for a quantitative study. Thus, for lower temperatures near the phase transition, lattice QCD calculations are employed for ab-initio determination of transport coefficients.

The study at hand employs continuum extrapolated euclidean vector current correlation functions measured in quenched lattice QCD and an ansatz-based approach, developed and laid out in [7], to find vector meson spectral functions and thus dilepton rates in the deconfined phase at three temperatures  $1.1 T_c$ ,  $1.2 T_c$  and  $1.4 T_c$ .

First lattice studies of a more exploratory nature can be found in [64, 65, 66]. Nowadays, extracting transport coefficients and dilepton rates is an established objective for lattice QCD calculations. For recent studies see e.g. [67, 68, 69, 70], and for an extensive review [22]. However, the determination of these quantities is much more involved than for example the calculation of hadron masses: Spectral functions cannot directly be extracted from lattice calculations, they are only linked to measurable lattice observables through Laplace-like transformations.

## 5.2 Dilepton rates and the vector spectral function

The vector spectral function is a central quantity in this analysis: It directly relates to the dilepton rate as

$$\frac{dW}{d\omega d^3\vec{p}} = \frac{5\alpha^2}{54\pi^3} \frac{1}{(\omega^2 - \vec{p}^2)(e^{\omega/T} - 1)} \rho_{ii}(\omega, \vec{p}, T) \quad (5.1)$$

## 5 Thermal dilepton rates

Here and in the following,  $\rho_{ii}$  indicates a summation over all spatial components, while  $\rho_{00}$  marks the time-like component. The full vector spectral function is then given by  $\rho_V = \rho_{00} + \rho_{ii}$ .

Also, as already done for observables in previous chapters, the explicit temperature dependence of  $\rho_V$  is dropped and observables are quoted in matching units of the temperature  $T$ .

The electrical conductivity is connected to the spectral function by a Kubo formula[71]. Thus, extracting the spectral function also yields access to the electrical conductivity  $\sigma$ , by taking the limit  $\omega \rightarrow 0$  of  $\rho_{ii}(\omega)$  as

$$\frac{\sigma}{T} = \frac{C_{\text{em}}}{6} \lim_{\omega \rightarrow 0} \frac{\rho_{ii}(\omega)}{\omega T} \quad (5.2)$$

$C_{\text{em}}$  is given by the elementary charges  $Q_f$  of the quark flavors  $f$  as  $C_{\text{em}} = \sum_f Q_f^2$ .

Spectral functions like  $\rho_V$  are not directly accessible to lattice QCD calculations. Instead, their relation to the vector correlation function has to be used. A Laplace-like transformation of the form

$$G_H(\tau, \vec{p}, T) = \int_0^\infty \frac{d\omega}{2\pi} \rho_H(\omega, \vec{p}, T) \frac{\cosh(\omega(\tau - 1/2T))}{\sinh(\omega/2T)} \quad \text{with: } H = 00, ii, V. \quad (5.3)$$

provides the link of the spectral function to the vector correlation function  $G(\tau, \vec{p})$ , which is directly accessible in lattice QCD calculations. Unfortunately, transformations as eq. (5.3) cannot be inverted easily. Therefore, more involved methods have to be employed to reconstruct  $\rho_H$  from  $G_H$ .

The goal to obtain a spectral function through eq. (5.3) from a given correlator has motivated and initiated a lot of work, the results of which can be divided into two broad categories:

### 5.2.1 Bayesian techniques: Maximum entropy method

Bayesian techniques like the widely used maximum entropy method (MEM) have long been used to extract hadron spectral functions from lattice QCD calculation [72, 70, 65]. They are –in principle– capable of reproducing a spectral function from a given dataset of the correlator, with only a default model as small additional input.

The default model is used to set an initial form of the spectral function. Iteratively, this model is then modified to find the most probable spectral function that is in agreement with the data through eq. (5.3). On a precise, high resolution dataset, this process reaches a unique solution that is not influenced by any (reasonable) choice of the default model.

While in general Bayesian techniques are mathematically well understood, they have certain drawbacks when used for this purpose: Most lattice datasets do not meet the requirements of being precise and high in resolution to make the solution independent of the input default model and thus fully unique. In this case, systematic error estimates become involved, since the choice of a default model has to be motivated and taken into

account. Also, in these cases it can be hard to keep MEM from reaching results that are unphysical solutions for the spectral function, if these solutions fit the data well.

To date, improvements to MEM addressing these issues are on their way [73], adapting MEM to better cope with lattice QCD results.

### 5.2.2 Model-based ansatz

An alternative to Bayesian methods is to propose an ansatz for the spectral function and fit it to the given dataset by employing standard minimization techniques.

For this procedure, it is necessary to motivate and parametrize a form for the spectral function. In contrast to MEM, this model becomes a fixed, unmutable part of the analysis.

A previous study at  $1.4 T_c$  [67] laid the foundation for this technique as used in this work. Extracting a spectral function by an ansatz fitted to continuum extrapolated lattice data was, for the first time, successfully implemented there. Together with related results on the temperature dependence of the electrical conductivity [74], it motivated the systematic study of the temperature dependence of dilepton rates presented in this work.

By now, the same ansatz has also successfully been used to analyze results obtained from finite size dynamical lattices [69, 75].

## 5.3 Ansatz for the vector spectral function

The ansatz used to model the spectral function in this work has to be motivated. First, the spectral functions division into a time-like component  $\rho_{00}$  and a spatial component  $\rho_{ii}$  becomes important:

The time-like component of vector correlator  $G_{00}$  is a measure for the quark number susceptibility  $\chi_q$ . Since the quark number is a conserved quantity, the vector correlator is constant in Euclidean time:  $G_{00}(\tau T) = -\chi_q T$ . Its spectral representation, the corresponding component in the spectral function  $\rho_{00}$ , therefore has to be a delta peak:

$$\rho_{00}(\omega) = -2\pi\chi_q\omega\delta(\omega). \quad (5.4)$$

In the free field limit, the spatial component of the spectral function is known to increase quadratically for large  $\omega$ , so for massless quarks

$$\rho_{ii}^{\text{free}}(\omega) = 2\pi T^2\omega\delta(\omega) + \frac{3}{2\pi}\omega^2 \tanh(\omega/4T). \quad (5.5)$$

is obtained. For the full spectral function  $\rho_V = \rho_{00} + \rho_{ii}$ , the delta peaks in the time-like and in the spatial component cancel in the free field massless limit, and the free spectral function becomes

$$\rho_V^{\text{free}}(\omega) = \frac{3}{2\pi}\omega^2 \tanh(\omega/4T). \quad (5.6)$$

This form of the spectral function changes in the interacting case: The delta peak in the time-like component does not vanish, as it stems from the conserved quark number susceptibility. The form of  $\rho_{00}$  given in eq. (5.4) therefore does not change.

## 5 Thermal dilepton rates

However, the delta peak in the spatial component smears out when moving from free theory to finite temperature. It is expected to become a Breit-Wigner peak [64, 76, 77, 78], which motivates an ansatz for the interacting version of eq. (5.5) that reads

$$\rho_{ii}^{\text{interac.}}(\omega) = \chi_q c_{\text{BW}} \frac{\omega \Gamma}{\omega^2 + (\Gamma/2)^2} + (1 + \kappa) \frac{3}{2\pi} \omega^2 \tanh(\omega/4T). \quad (5.7)$$

The full spectral function  $\rho_V$  is still given by  $\rho_V = \rho_{00} + \rho_{ii}$ , but now holds a delta peak in the time-like component that is no longer canceled by a corresponding contribution in the spatial component.

The ansatz in eq. (5.7) now holds three parameters to match the spectral function to a given correlator: The strength ( $c_{\text{BW}}$ ) and width ( $\Gamma$ ) of the Breit-Wigner, modifying mostly the low frequency behavior, and  $\kappa$  to adjust the high frequency deviation from free theory with a constant factor, that is motivated from leading order perturbation theory. It was shown that at  $1.4 T_c$  this rather simple ansatz fits the data already very well [7, 67].

Taking the limit  $\omega \rightarrow 0$ , the electrical conductivity directly follows from the parametrization of the Breit-Wigner peak, as eq. (5.2) becomes

$$\frac{\sigma}{T} = \frac{C_{\text{em}}}{6} \lim_{\omega \rightarrow 0} \frac{\rho_{ii}(\omega)}{\omega T} \rightarrow \sigma(T)/C_{\text{em}} = 2\chi_q c_{\text{BW}}/(3\Gamma). \quad (5.8)$$

## 5.4 Setup of a temperature dependence study

The approach laid out in section 5.3 so far has been developed and employed in the previous study [7, 67], which provided a first dataset at  $1.4 T_c$  and motivated the systematic study of temperature dependence in the deconfined phase towards  $T_c$ .

The work presented here analyses two further temperatures  $1.1 T_c$  and  $1.4 T_c$ , where preliminary results on the first temperature  $1.1 T_c$  have been presented in [8].

The simulation parameters for the two new temperatures  $1.1 T_c$  and  $1.2 T_c$  have been set up with a certain set of constraints: Three couplings  $\beta = 7.192, 7.544$  and  $7.793$  were chosen with corresponding lattice spacings to allow for a continuum extrapolation. These  $\beta$ -values are picked in a way that at each coupling three temperatures  $1.1 T_c$ ,  $1.2 T_c$  and the original  $1.4 T_c$  can be realized with even values of  $N_\tau$ . The lattices extent  $N_\sigma$  is set to a fixed physical volume  $N_\sigma \cdot a$ , translating to one fixed aspect ratio per temperature. A summary of the simulation parameters for the temperatures  $1.1 T_c$  and  $1.2 T_c$  can be found in table 5.1, the parameters for the first dataset at  $1.4 T_c$  are quoted in table 5.2.

All calculations have been carried out with light quark masses tuned to  $m_{\overline{MS}}(\mu = 2 \text{ GeV}) < 25 \text{ MeV}$ . A short analysis on how the hopping parameter  $\kappa$  of the Wilson action has been tuned to obtain these masses can be found in the corresponding section 3.3.1.

#### 5.4 Setup of a temperature dependence study

$\beta$	$N_\sigma$	$1/a[\text{GeV}]$	$a[\text{fm}]$	$1.1 T_c$			$1.2 T_c$		
				$N_\tau$	$\kappa$	# conf	$N_\tau$	$\kappa$	# conf
7.192	96	10.4	0.0190	32	0.13440	314	28	0.13440	232
7.544	144	15.5	0.0125	48	0.13383	367	42	0.13382	417
7.793	192	20.4	0.0097	64	0.13345	242	56	0.13345	195

Table 5.1: Summary of simulation parameters, linking three different lattice spacings  $a$  (with corresponding couplings) and two temperatures  $T/T_c$ . The resulting lattices are set to a constant physical size  $N_\sigma \cdot a$ , which results in one constant aspect ratio per temperature. The physical scales are quoted from section 3.1, quark masses corresponding to the given  $\kappa$ -values can be found in section 3.3.1. Note that the temperature  $1.4 T_c$  of the preceding study could be realized by setting  $N_\tau = 24, 36, 48$ .

$\beta$	$N_\sigma$	$N_\tau$	$1.4 T_c$			
			$1/a[\text{GeV}]$	$a[\text{fm}]$	$\kappa$	# conf
7.192	128	24	10.4	0.0190	0.13440	340
7.458	128	32	14.1	0.0140	0.13383	255
7.793	128	48	20.4	0.0097	0.13340	451

Table 5.2: Summary of simulation parameters of the preceding study at  $1.4 T_c$ . Lattice spacings and the quoted temperature have been recalculated from the new results in sections 3.1 and 3.2.

## 5.5 Continuum correlators from the lattice

The vector correlation function  $G(\tau, \vec{p})$  on the left hand side of (5.3) can be calculated on the lattice, see section 1.5.2. These calculations are subject to a set of limitations:

- The finiteness of the lattice leads to a discrete and finite number of points  $N_\tau$  in the correlator. Increasing  $N_\tau$  at a constant temperature and on an isotropic lattice reduces the lattice spacing. To keep the volume constant,  $N_\sigma$  has to be increased by the same factor. The computing effort rises faster than linear with increasing the 4-volume  $N_\sigma^3 \times N_\tau$ , so higher  $N_\tau$  quickly lead to huge demands in computing power.
- The measurements have statistical errors due to the finite number of gauge configurations that sample the path integral. Sampling more contributions will of course lower the error, which scales with  $\sqrt{n}$  to the number of sampling points  $n$ . Therefore, doubling the precision will yield a factor of four in computing time.
- Finite volume effects can enter through the limited spatial lattice size  $N_\sigma \cdot a$ . A series of different lattice volumes  $N_\sigma$  at fixed spacing is usually used to check for finite volume effects and to choose a minimal lattice size where they are low enough. The lattice volume also influence which momenta  $\vec{p}$  are accessible, since they are linked to the lattice aspect ratio.
- Most importantly, the correlator is influenced by cutoff effects due to the finite lattice spacing  $a$ . A small spacing  $a$  helps to minimize the cutoff effects, but it also largely increases computing costs by raising  $N_\tau$ . A continuum extrapolation allows for a necessary improvement: The cutoff effects of non-perturbatively improved Wilson fermions scale with  $O(a^2)$  in the lattice spacings. By calculating correlators for (at least) three different lattice spacing  $a$ , a continuum extrapolation of these correlators can be performed.

### 5.5.1 Ratios to free continuum and lattice correlators

A few requirements have to be met for the continuum extrapolation to work, and some improvements can be introduced to make them more precise:

Lattice calculations have to be performed at fixed temperature  $T$  on a set of different extents  $N_\tau$ , where  $a$  is tuned to keep  $T = 1/(N_\tau \cdot a)$  constant. This yields a set of couplings  $\beta$ , since  $a$  is directly linked to the coupling, as laid out in section 3.1.

The spatial extent of the lattice also has to be checked. In any case, it has to be big enough for the results to be free of finite volume effects. It is also advisable to keep the extent in physical units  $N_\sigma \cdot a$  fixed, which translates to a fixed aspect ratio  $N_\sigma/N_\tau$ . On the one hand, this should ensure that any finite volume effects that are still left at a certain lattice size should be similar for each lattice spacing. On the other hand, and more importantly, constant aspect ratios are necessary when extrapolating for finite momenta  $G_V(\tau T, \vec{p} \neq 0)$ , as the aspect ratio sets the momenta available on the lattice.

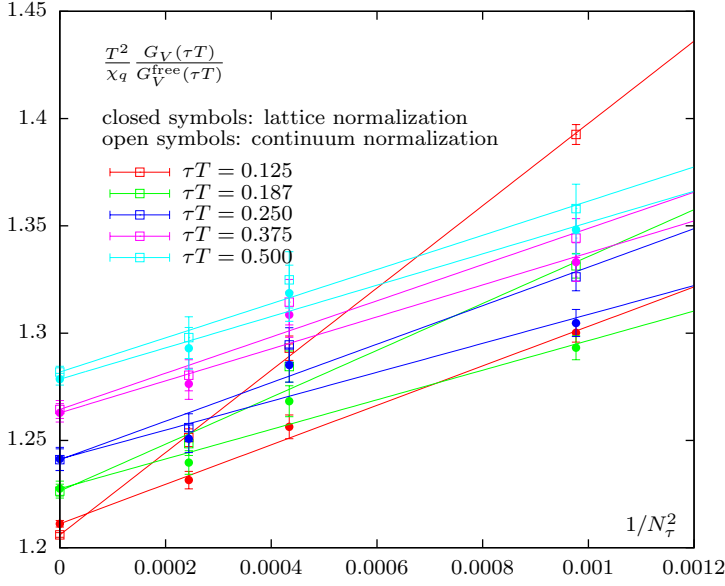


Figure 5.4: Extrapolation of  $G_V$  towards continuum  $a \rightarrow 0$ , for the 1.1  $T_c$  dataset, normalized by both  $G_V^{\text{free,cont.}}$  (closed symbols) and  $G_V^{\text{free,lat}}$  (open symbols) at different distances  $\tau T$ . As expected, especially for the normalization  $G_V^{\text{free,cont.}}$ , stronger cutoff effects can be observed towards lower distances  $\tau T$ .

When extrapolating a correlation function to the continuum, it has to be evaluated at a fixed distance  $\tau = a \cdot n_t$ . Only a few combinations where  $\tau = a^{\text{fine}} \cdot n_t^{(1)} = a^{\text{medium}} \cdot n_t^{(2)} = a^{\text{coarse}} \cdot n_t^{(3)}$  will be available on a set of finite lattice extents  $N_\tau$ . Even in the best case this number of common points will be limited to  $N_\tau$  on the coarsest lattice. To solve this problem, the correlation function has to be interpolated on all but the finest lattice spacings, such that an extrapolation towards the continuum is possible for all points  $N_\tau^{\text{fine}}$ .

Correlation functions usually fall off exponentially, making them not very suitable for interpolation when used directly. Normalizing them with the free correlation function  $G_H^{\text{free}}$  (that shares a similar exponential fall-off) yields a much smoother function that can easily be interpolated by, for example, a cubic spline. Two variations of this free correlation function can be chosen, either one in the continuum  $G_H^{\text{free,cont.}}(\tau T)$  or one on a matching (same  $N_\tau$ ) finite lattice  $G_H^{\text{free,lat.}}(\tau T)$ . When normalizing with the free lattice correlator, the portion of cutoff effects that is present in the free theory is divided out.

As a crosscheck, both normalizations have to produce compatible results in the continuum limit, because ideally both should remove the lattice cut-off effects in the same way. Differences emerge at smaller distances  $\tau T$ , where the extrapolation should no longer be considered valid. In fig. 5.4 this extrapolation is visualized for different distances  $\tau T$ .

A last point to consider is renormalization. Since different lattice spacings  $a$  correspond to different couplings  $\beta$ , the correlators would have to be renormalized as

## 5 Thermal dilepton rates

$G'_H = G_H^{\text{bare}} \cdot Z_H(\beta)$ , where  $Z(\beta)$  depends on the coupling. While non-perturbative results for the renormalization constant are available, a more precise method can be used: Since  $G_{00}$  is constant (see eq. (5.4)) and renormalized by the same constant  $Z_V(\beta)$ , the ratios  $G_V(\tau T)/G_{00}$  and  $G_{ii}(\tau T)/G_{00}$  are free of renormalization constants. The ratio to the free theory is not influenced, since  $G_{00}^{\text{free}} = 1/T^3$ .

### 5.5.2 A summary of the extrapolation procedure

To sum up the discussion laid out in the last section, the following procedure is employed to arrive at a continuum correlator:

- A double ratio to cancel renormalization constants and the exponential fall-off is calculated for each correlator. Both the free continuum and the free lattice correlation function can enter into the normalization:

$$R_{N_\tau}(\tau T) = \underbrace{\frac{G_{V,ii}(\tau T)}{G_{00}}}_{\text{cancels renormalization}} \cdot \underbrace{\frac{G_{00}^{\text{free}} = 1/T^3}{G_{V,ii}^{\text{free}}(\tau T)}}_{\text{cancels exponential fall-off}} \quad (5.9)$$

- A cubic spline interpolation is performed for the ratio eq. (5.9) on every spacing. This allows to calculate the correlator ratio at any arbitrary distance  $\tau T$ .
- Values for the correlator ratio eq. (5.9) are calculated on every distance  $\tau T$  accessible by points  $n_t$  on the finest lattice.

Using a fit of the relation

$$R_{N_\tau}(\tau T) = (1 + d(\tau T) \frac{1}{N_\tau^2}) \cdot R^{N_\tau \rightarrow \infty}(\tau T) \quad (5.10)$$

the results are extrapolated to the continuum. The parameter  $d$  depends on the distance and can be viewed as a measure of the cutoff effect. The extrapolation should be independent of the free normalization (continuum or lattice) used in eq. (5.9).

In fig. 5.5 the results of this procedure for  $G_{ii}(\tau T)$  and  $G_V(\tau T)$  at  $1.1 T_c$  and  $1.2 T_c$  can be found. For both temperatures, precise continuum extrapolations have been carried out in a range from  $\tau T = 0.5$  down to the same physical distance to the source  $n_t^{a=0.0097 \text{ fm}} = 8$ . For smaller distances, the extrapolation clearly breaks down due to rising cutoff effects. These distances translate to points  $n_t^{a=0.0125 \text{ fm}} = 6$  and  $n_t^{a=0.0190 \text{ fm}} = 4$  on the coarser lattices and to  $\tau T = 0.125$  at  $1.1 T_c$  as well as  $\tau T = 0.142$  at  $1.2 T_c$ .

While on finite lattices cutoff effects set in with lower  $\tau T$ , the continuum extrapolated correlator ratios have to converge towards  $T^2/\chi_q$  in the limit  $\tau T \rightarrow 0$ . As can be seen in the figures, this convergence is found for both  $1.1 T_c$  and  $1.2 T_c$ .

A continuum value for  $G_{00}$  can be found by extrapolating  $G_{00}$  using the same ansatz as for  $G_V, G_{ii}$ . Here, the non-perturbative renormalization constant  $Z_V(\beta)$ , see section 3.4,

## 5.5 Continuum correlators from the lattice

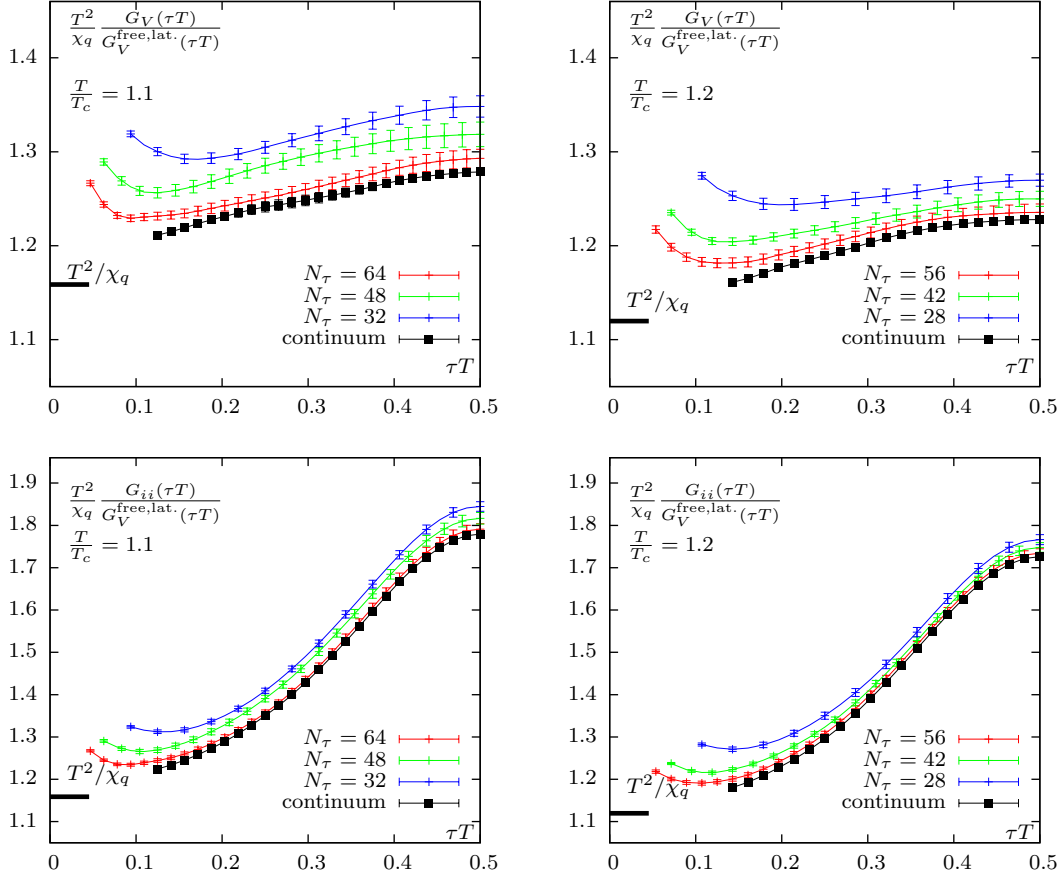


Figure 5.5:  $G_V(\tau T)/G_V^{\text{free,lat.}}(\tau T)$  (upper row) and  $G_{ii}(\tau T)/G_V^{\text{free,lat.}}(\tau T)$  (lower row) on finite lattices (red, blue, green), interpolated between points  $n_t$  and extrapolated to the continuum (black). Both new datasets at  $1.1 T_c$  (left) and  $1.2 T_c$  (right) are shown.

$\beta$	$Z_V(\beta)$	1.1 $T_c$		1.2 $T_c$	
		$N_\tau$	$\chi_q/T$	$N_\tau$	$\chi_q/T$
7.192	0.8421	32	0.8330	28	0.8538
7.544	0.8539	48	0.8431	42	0.8794
7.793	0.8612	64	0.8559	56	0.8894
		$\infty$	0.8590(8)	$\infty$	0.9001(30)

Table 5.3: Values of  $G_{00} = \chi_q/T$  for temperatures 1.1  $T_c$  and 1.2  $T_c$ , on all three lattice spacings and extrapolated to the continuum.  $Z_V(\beta)$  is given in eq. (3.20). At 1.4  $T_c$ ,  $\chi_q/T = 0.897(3)$  for  $a \rightarrow 0$ , see [7].

replaces the normalization by  $G_{00}$ . The continuum extrapolated value for  $G_{00}$  can be used to reverse the normalization through  $1/G_{00}$  on the other continuum extrapolated ratios. Values of  $G_{00} = \chi_q/T^2$  for both temperatures on finite lattices and in the continuum are given in table 5.3.

### 5.5.3 Error estimate of the continuum extrapolation

The correlators entering into the continuum extrapolation are subject to statistical errors. For the correlators on finite lattices, these errors are obtained by a jackknife analysis. The error of the resulting continuum correlators have been estimated in two different ways:

A weighted linear regression in  $a^2$  is used for the continuum extrapolation, taking the jackknifed averages and errors on each finite lattice as input. The variance and correlation of the linear regression is used as an error estimate denoted *standard error*.

Also, a re-sampling approach has been implemented: On each finite lattice, a subset of  $m$  randomly selected correlators is used to calculate a continuum extrapolated data set. This process is repeated  $n$  times, providing  $n$  samples of the continuum extrapolated correlator ratio. These samples are then used to calculate a continuum average and error. The number of randomly chosen correlators  $m$  and the number of samples  $n$  are set to be in the same order as the original dataset size, e.g.  $m = 200, 500$  and  $n = 200, 500$ .

In fig. 5.6 the resulting continuum error estimates are given. Also, the difference between the averages obtained with the standard method and the re-sampled correlators are shown. The errors are distributed differently for both methods: The re-sampled errors grow larger towards larger distances  $\tau T$ , where the correlator gets smaller and possibly more noisy. The errors obtained from the linear regression grow in regions of  $\tau T$  where the assumption of a linear behaviour in  $1/a^2$  does not hold as well as in other regions.

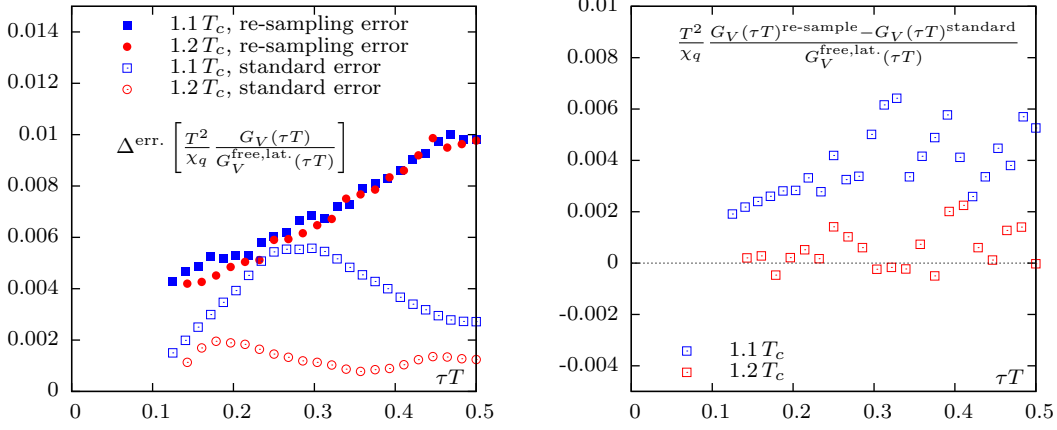


Figure 5.6: Error estimates using the standard error from a weighted linear regression and the error employing re-sampling (left). Difference between the average continuum extrapolated correlators using re-sampling to the standard continuum extrapolation (right). Re-sampling parameters, as given in section 5.5.3 are  $m = 200$  and  $n = 200$ .

## 5.6 Spectral function fit procedure

Now that an ansatz for the spectral function has been motivated and continuum correlators are available on the lattice, the next step is to perform fits to obtain the spectral function.

Following eq. (5.9) the ratio of the spatial correlator  $G_{ii}(\tau T)$  to the full free correlator  $G_V^{\text{free}}(\tau T)$  as  $T^2 \cdot G_{ii}(\tau T)/\chi_q \cdot G_V^{\text{free}}(\tau T)$  is used to serve as input to the fit. While all combinations are in principle equivalent descriptions of the system, this specific combination leads to spectral functions  $\rho_{ii}$  and  $\rho_V^{\text{free}}$  which are both free of delta peaks. This fact helps to perform numerical integrations for the fit.

For the implementation of the fit, substitutions

$$a' := 1 + \kappa, \quad g' := \Gamma/2, \quad c' := 2\chi_q c_{\text{BW}}/\Gamma \quad (5.11)$$

are used to write the ansatz in eq. (5.7) as

$$\begin{aligned} \rho_{ii}(\omega) &= \chi_q c_{\text{BW}} \frac{\omega \Gamma}{\omega^2 + (\Gamma/2)^2} + (1 + \kappa) \frac{3}{2\pi} \omega^2 \tanh(\omega/4T) \\ &= c' \frac{\omega}{\frac{\omega^2}{g'^2} + 1} + a' \frac{3}{2\pi} \omega^2 \tanh(\omega/4T). \end{aligned} \quad (5.12)$$

While  $a'$  and  $g'$  are only shorthands, the choice of  $c'$  introduces a fit variable that is directly proportional to the electrical conductivity, as  $3 \cdot \sigma(T)/(TC_{\text{em}}) = c'$ , see eq. (5.8).

The fit can be performed either to the ratio  $G_{ii}(\tau T)/G_V^{\text{free}}(\tau T)$ , found by multiplying out the quark number susceptibility from the data first, or directly to the data set  $T^2 \cdot G_{ii}(\tau T)/\chi_q \cdot G_V^{\text{free}}(\tau T)$ . In the second case, a factor of  $\chi_q$  is passed through the

## 5 Thermal dilepton rates

transformation and enters into the spectral function. Labeling the variables of a fit to  $T^2 \cdot G_{ii}(\tau T)/\chi_q \cdot G_V^{\text{free}}(\tau T)$  as  $a$ ,  $c$  and  $g$ , they relate to eq. (5.12) as

$$a = a'/\chi_q = (1 + \kappa)/\chi_q, \quad g = g' = \Gamma/2, \quad c = c'/\chi_q = 2c_{\text{BW}}/\Gamma \quad (5.13)$$

Two more components enter into the fit: Introducing thermal moments stabilizes the fit by imposing a further constraint and modifying the spectral function ansatz allows for a systematic error analysis.

### 5.6.1 Thermal moments

The low  $\omega$  behavior given by the Breit-Wigner contribution to eq. (5.7) is of high importance for the determination of the electrical conductivity. This low frequency region of the spectral function is most affected by the correlator at large distances  $\tau T$ .

A constraint on the spectral function fit can thus be introduced to make it more sensitive to large Euclidean distances  $\tau T$ . The thermal moments

$$G_H^{(n)} = \frac{1}{n!} \left. \frac{d^n G_H(\tau T)}{d(\tau T)^n} \right|_{\tau T=1/2} = \frac{1}{n!} \int_0^\infty \frac{d\omega}{2\pi} \left( \frac{\omega}{T} \right)^n \frac{\rho_H(\omega)}{\sinh(\omega/2T)} \quad \text{with } H = ii, V \quad (5.14)$$

are defined as the Taylor coefficients of the correlation function expanded around the midpoint

$$G_H(\tau T) = \sum_{n=0}^{\infty} G_H^{(2n)} \left( \frac{1}{2} - \tau T \right)^{2n}. \quad (5.15)$$

By calculating these moments for the free correlation function  $G_V^{\text{free}}$  analytically, they can also be used in ratios like eq. (5.9).

For the analysis, the ratios of the interacting to the free midpoint subtracted correlators

$$\Delta_V(\tau T) = \frac{G_V(\tau T) - G_V^{(0)}}{G_V^{\text{free}}(\tau T) - G_V^{(0),\text{free}}} = \frac{G_V^{(2)}}{G_V^{(2),\text{free}}} \left( 1 + (R_V^{(4,2)} - R_{V,\text{free}}^{(4,2)}) \left( \frac{1}{2} - \tau T \right)^2 + \dots \right) \quad (5.16)$$

are calculated, where  $R_V^{(n,m)} = G_V^{(n)}/G_V^{(m)}$ . A varying number of contributions, generally the first two terms (up to quadratic) are then obtained through a fit of eq. (5.16) to the correlator, see fig. 5.7 and table 5.4 for the results.

Restricting the spectral function fit to also reproduce the thermal moments allowed to obtain a stable fit in the preceding study at  $1.4 T_c$ . The same analysis is thus used for the new  $1.1 T_c$  and  $1.2 T_c$  datasets. Specifically, the ratio of the second to the zeroth thermal moment

$$\frac{G_{ii}^{(2)}}{G_{ii}^{(0)}} = \frac{G^{(2)}}{G^{(2),\text{free}}} \cdot \frac{G_{ii}^{(0),\text{free}}}{G_{ii}^{(0)}} \cdot \frac{G^{(2),\text{free}}}{G_{ii}^{(0),\text{free}}} = \Delta_{ii}(0.5) \cdot G_{ii}(0.5) \cdot \frac{28}{15} \pi^2 \quad (5.17)$$

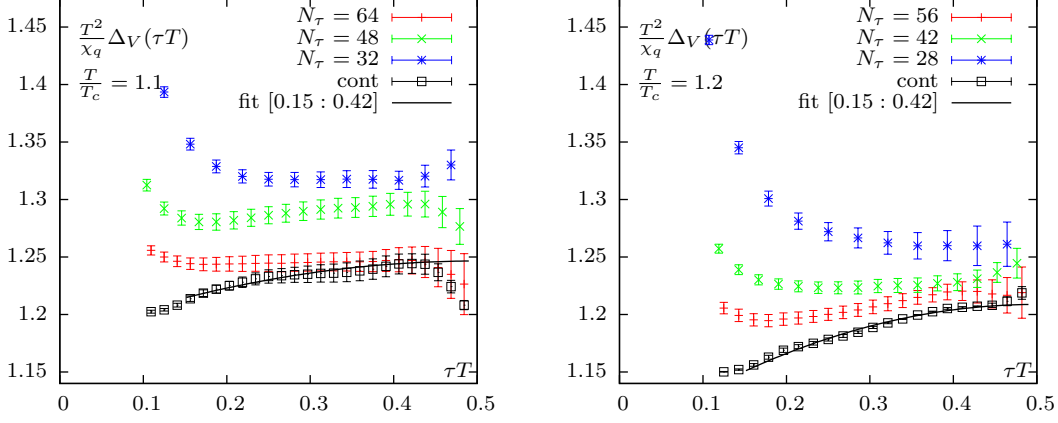


Figure 5.7: Midpoint subtracted correlator data and fits to obtain the thermal moments, eq. (5.16), up to quadratic order, with  $1.1 T_c$  on the left,  $1.2 T_c$  on the right. For large distances of  $\tau T \rightarrow 0.5$ , the continuum extrapolation of the  $1.1 T_c$  dataset becomes somewhat unstable. The errors quoted in table 5.4 take these uncertainties into account.

	$G_V^{(0)} / (\chi_q G_V^{(0),\text{free}})$	$G_{ii}^{(0)} / (\chi_q G_{ii}^{(0),\text{free}})$	$G_{V,ii}^{(2)} / (\chi_q G_{V,ii}^{(2),\text{free}})$	$G_{ii}^{(2)} / G_{ii}^{(0)}$
$1.1 T_c$	1.280(3)	1.189(2)	1.238(5)	19.188(50)
$1.2 T_c$	1.228(2)	1.151(1)	1.210(2)	19.366(36)
$1.4 T_c$	1.211(9)	1.142(9)	1.189(13)	19.215(180)

Table 5.4: Results for the thermal moments eq. (5.15), obtained by fitting eq. (5.16) to data, for temperatures  $1.1 T_c$  and  $1.2 T_c$ .  $G^{(0)}$  is given by the correlator at midpoint, needed to calculate the ratio of second to zeroth thermal moment. It is given in the last column  $G_{ii}^{(2)} / G_{ii}^{(0)}$  and used to constrain the fits. Values of  $\chi_q$  can be found in table 5.3. Values and errors for  $1.4 T_c$  are quoted from [7].

## 5 Thermal dilepton rates

is used as the constraint. The right hand side is found by fitting eq. (5.16) to obtain  $\Delta_{ii}$ , by evaluating the correlator itself at midpoint, since  $G_{ii}^{(0)} = G_{ii}(0.5)$ , and by the ratio of the free thermal moments. Contributions of  $\chi_q$  in the extrapolated correlators cancel in this ratio.

### 5.6.2 Systematic error estimates

Fitting the spectral function yields the standard error estimates for the fit parameters. However, these errors do not capture systematics, as the functional form of the spectral density is not mutable by the fit.

A modification of the low energy structure in eq. (5.7) is introduced to check if and how the high frequency region, dominated by the free spectral function, influences the low  $\omega$  region dominated by the Breit-Wigner peak.

A smeared heavy-side step function

$$\Theta(\omega_0, \Delta_\omega) = \left(1 + e^{(\omega_0^2 - \omega^2)/\omega\Delta_\omega}\right)^{-1} \quad (5.18)$$

parametrized with a cutoff position  $\omega_0$  and the strength of the falloff  $\Delta_\omega$  is used to smoothly cut off the continuum contributions in eq. (5.7) towards low frequencies. This extended spectral function now reads

$$\rho_{ii}^{\text{trunc.}}(\omega) = \chi_q c_{\text{BW}} \frac{\omega\Gamma}{\omega^2 + (\Gamma/2)^2} + (1 + \kappa) \frac{3}{2\pi} \omega^2 \tanh(\omega/4T) \Theta(\omega_0, \Delta_\omega) \quad (5.19)$$

where setting  $\omega_0 = 0$  and  $\Delta_\omega$  reproduces eq. (5.7). The fit of eq. (5.19) is now performed as before, with  $\omega_0$  and  $\Delta_\omega$  set to suitable values. Moving the cut-off  $\omega_0$  towards higher frequencies, the area of the Breit-Wigner-peak should increase, in most cases leading to a higher electrical conductivity. The influence of the strength  $\Delta_\omega$  is not as easy to predict.

The contributions of the Breit-Wigner and the truncated continuum, adding up to the full spectral function, are shown in fig. 5.8 for different choices of  $w_0$  and  $\Delta_\omega$  at  $1.1 T_c$ .

While the functional form of the ansatz eq. (5.19) is still rather simple, the fit procedure itself becomes more involved: For the original ansatz, the transformation of eq. (5.7) through eq. (5.3) can be rewritten, so only the Breit-Wigner-contribution has to be numerically integrated and the free continuum enters as a constant. For the truncated ansatz, the full spectral function eq. (5.19) has to be numerically integrated through eq. (5.3) to arrive at the correlator. Some care has to be taken that this integration is performed with adequate precision.

## 5.7 Fit of the spectral function ansatz

With the spectral function ansatz, continuum extrapolated correlators and the thermal moments in place, results of the fit procedure and therefore the spectral functions can now be discussed.

## 5.7 Fit of the spectral function ansatz

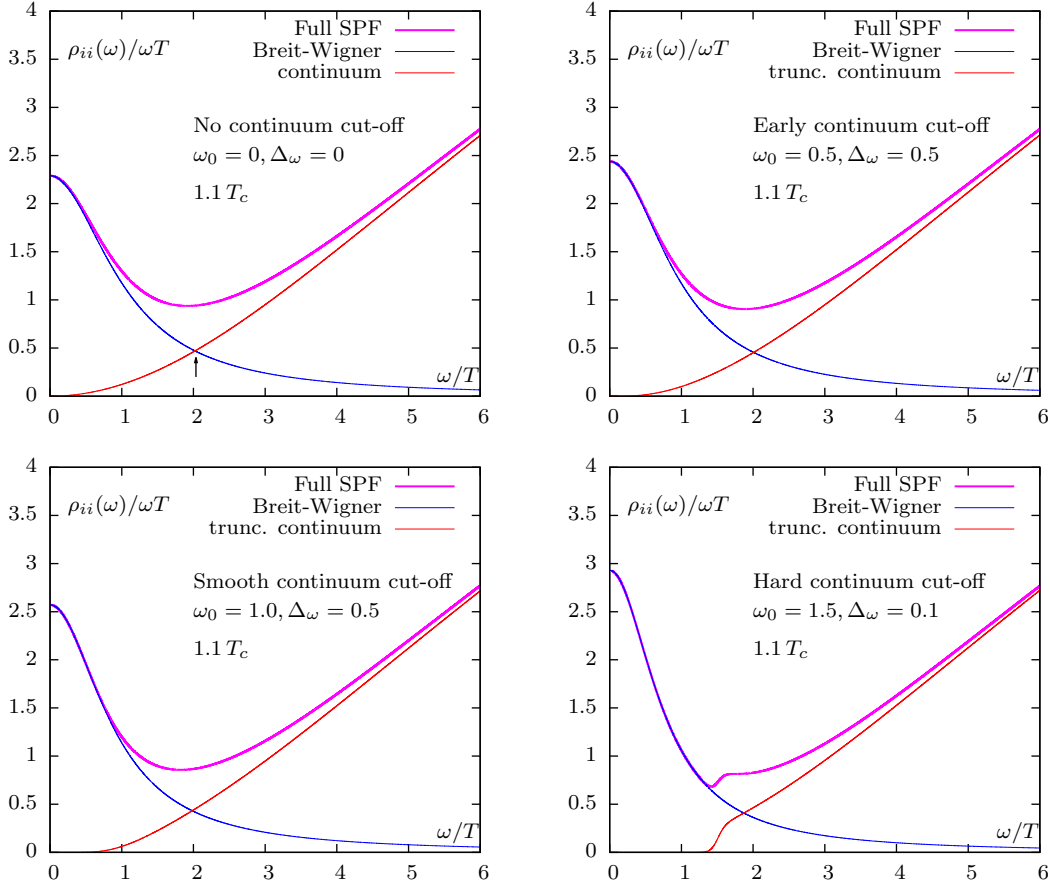


Figure 5.8: Contributions of the Breit-Wigner peak and the truncated continuum to the spectral function at  $1.1 T_c$ , for different values of  $\omega_0$  and  $\Delta_\omega$ . For the non-truncated spectral function ( $\omega_0 = 0, \Delta_\omega = 0$ ), the intersection of Breit-Wigner and continuum contribution is found at  $\omega \approx 2$ , marked by the arrow. Because of the steep falloff of the truncated continuum contribution, the hard cut-off at  $\omega_0 = 1.5$  with  $\Delta_\omega = 0.1$  is clearly visible in the full spectral function.

## 5 Thermal dilepton rates

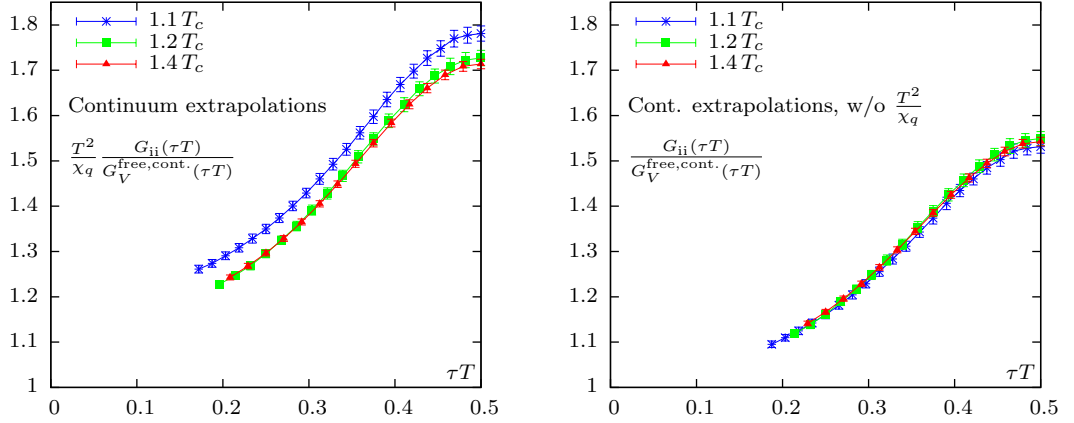


Figure 5.9: Correlator ratios as they enter into the spectral function fit procedure (left), for all three temperatures  $1.1 T_c$ ,  $1.2 T_c$ ,  $1.4 T_c$ . For comparison, the same data set free of the  $T^2/\chi_q$  contribution is shown, which is found by multiplying with values from table 5.3 (right).

Three temperatures were analyzed, the simulation setup for  $1.1 T_c$  and  $1.2 T_c$  is given in table 5.1. The dataset at  $1.4 T_c$  is taken from the previous study [7, 67]. The setup for  $1.4 T_c$  is quoted in table 5.2.

Before turning to the results of the spectral function fits, it is sensible to take another close look at the input dataset, the continuum extrapolated correlators  $G_{ii}(\tau T)/G_V(\tau T)$ . In fig. 5.9 these correlators are given as ratios  $G_{ii}(\tau T)/G_V(\tau T)$ , found by multiplying the extrapolated ratios with the continuum values of  $\chi_q$ , see table 5.3. This allows for a direct comparison between the correlators at different temperatures. All three data sets are very similar, as they are almost compatible within errors. This similarity is quite sensitive to the continuum extrapolated value of  $\chi_q$ . This effect should be kept in mind, as it shows the importance of obtaining precise values for  $\chi_q$ .

Spectral functions have been calculated from the continuum extrapolated correlators by using the analysis procedure as laid out in the previous sections.

To test the analysis and especially the systematic error estimates, two truncated spectral functions, with  $\omega_0 = 1.0$ ,  $\Delta_\omega = 0.5$  and  $\omega_0 = 1.5$ ,  $\Delta_\omega = 0.1$ , denoted smooth and hard continuum cut-off in fig. 5.8, have been fitted to the data set at all three temperatures. From the fit results, the correlators were then calculated by eq. (5.3). This allows for a direct comparison between the input dataset and the obtained results. In fig. 5.10 the spectral functions and a comparison of the obtained correlator is given, fig. 5.11 shows the same comparison applied to the older  $1.4 T_c$  dataset.

Using the ansatz without truncation of the continuum, a very good agreement between the correlators in the input dataset and the correlators obtained from the fitted spectral functions is found at all three temperatures. Thus, the ansatz is able to provide a valid description of the datasets.

## 5.7 Fit of the spectral function ansatz

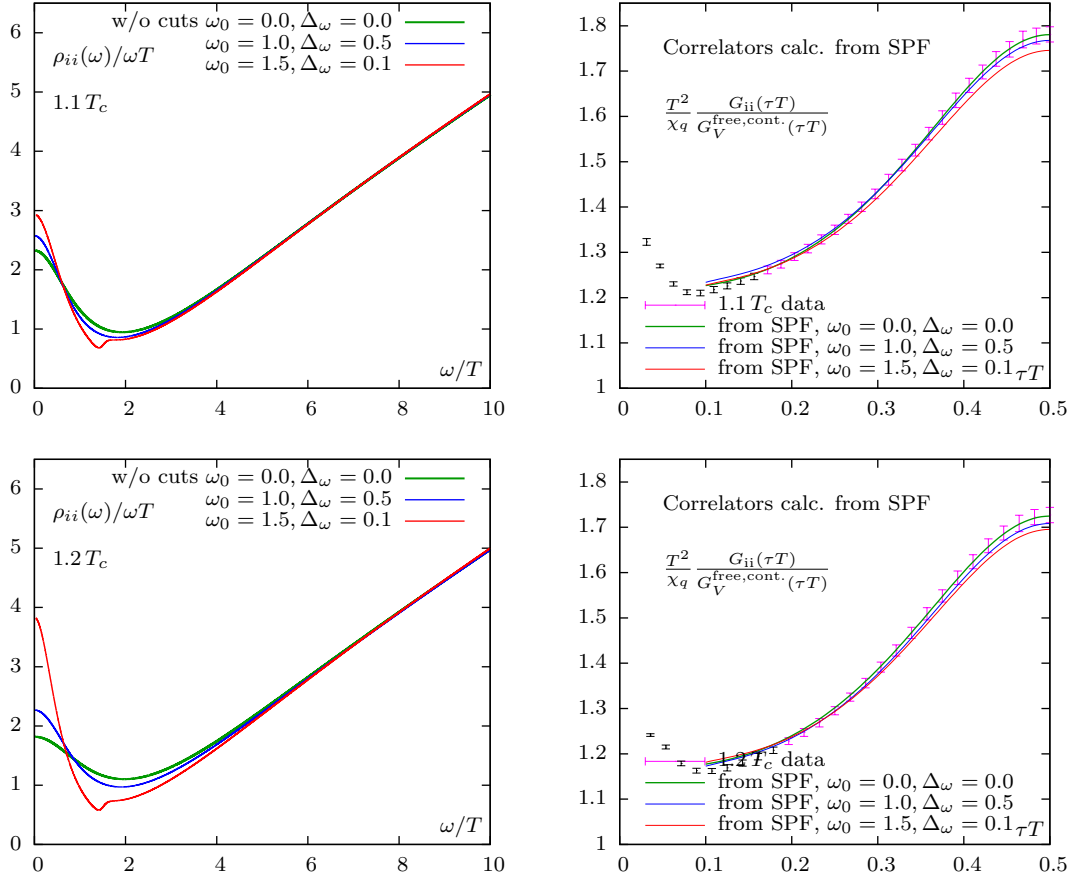


Figure 5.10: Temperatures  $1.1 T_c$  (upper row) and  $1.2 T_c$  (lower row): Spectral functions obtained through fits of eq. (5.19) to data, with different values of  $\omega_0$ ,  $\Delta_\omega$  as systematic error estimates (left). Correlators were calculated from these spectral functions through eq. (5.3) and input data (right). The black correlator data points did not enter into the fit.

## 5 Thermal dilepton rates

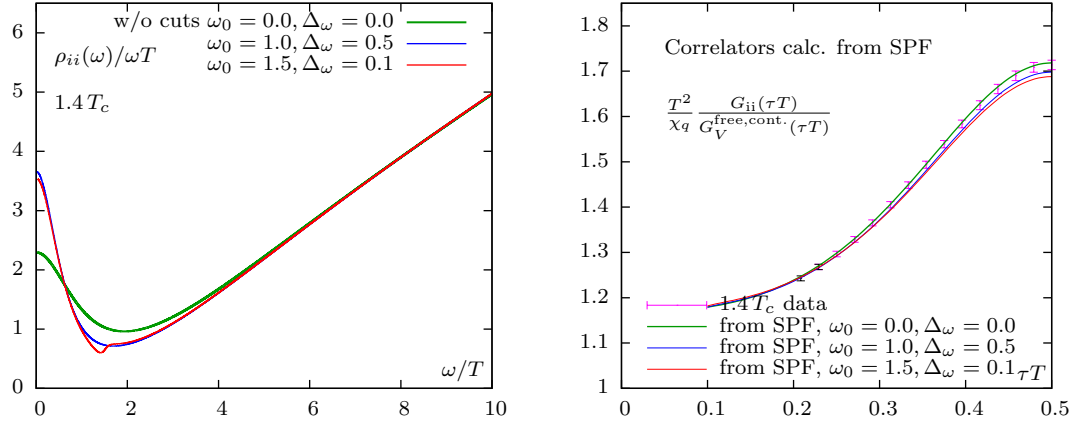


Figure 5.11: Spectral functions and correlators at  $1.4 T_c$ , see description at fig. 5.10

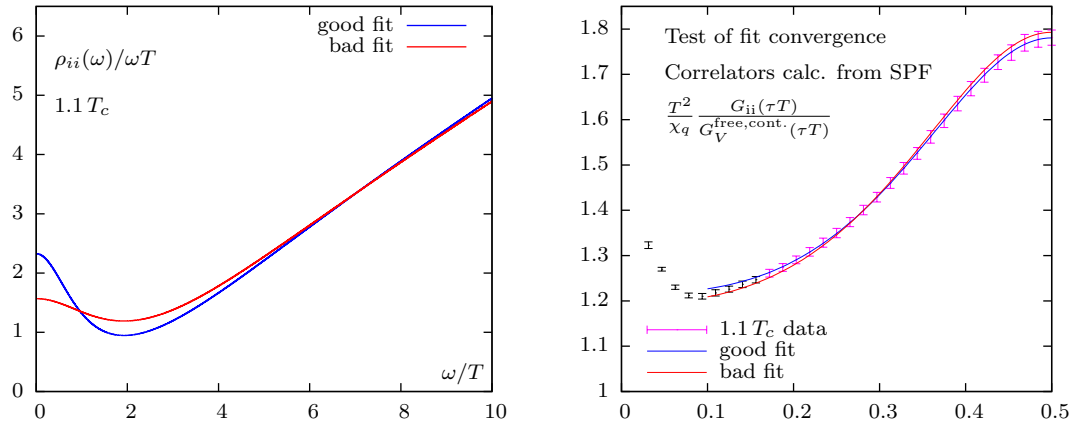


Figure 5.12: Spectral functions and correlators obtained from a fit that converged to a local minimum. The good matching fit has  $\chi/\text{d.o.f} = 0.52$ , the inferior fit has  $\chi/\text{d.o.f} \approx 1.2$ . The electrical conductivity found by the mismatching fit is  $\rho(T)/C_{\text{em}} = 0.260(8)$ .

### 5.7.1 Systematic error estimation

Turning to the systematic errors, the correlators calculated from the spectral function with a smooth continuum cut-off  $\omega_0 = 1.0$ ,  $\Delta_\omega = 0.5$  are within errors of the input dataset. For larger separations  $\tau T$ , a trend becomes apparent: Here the correlator relates most to the low  $\omega$  region of the spectral function. The contribution of the free spectral function to this region is cut away, and now the enhanced Breit-Wigner contribution can only partially compensate this effect. The resulting correlator becomes lower than the input dataset. The rise in the Breit-Wigner peak leads to a higher electrical conductivity. For the hard cut-off  $\omega_0 = 1.5$ ,  $\Delta_\omega = 0.1$ , this trend continues and the correlators, calculated from the spectral functions, are no longer fully within the errors of the input data. Since this is observed at all three temperatures, the cut-off at  $\omega_0 = 1.5$ ,  $\Delta_\omega = 0.1$  is set as an upper boundary to obtain systematic errors.

The procedure of calculating correlators from the fitted spectral function and comparing them with the input dataset also provides an important check of the fit convergence: The spectral function in fig. 5.12 was obtained from a fit with apparently good quality  $\chi/\text{d.o.f} \approx 1.2$ , but the fit converged to a local minimum, as it is very sensitive to a good initial choice of Breit-Wigner parameters. The comparison with the input dataset allows to easily find these mismatches, at least for the untruncated ansatz. The fits with truncated continuum contributions are harder to assess, as their results naturally deviate from the input data.

### 5.7.2 Results

Results for the spectral functions at all three temperatures are shown in fig. 5.13, together with the corresponding dilepton rates as calculated from eq. (5.1).

A summary of the fit results is given in tables 5.5 and 5.6. The fits have been performed for the three set of cut-off values motivated above, for both the re-sampled and the standard error estimates. Additional values for  $\omega_0, \Delta_\omega$  have been tested for the dataset with re-sampled error estimates: The full set of cut-off parameters as used in [67] was tested at  $1.1 T_c$ , and a selection of this set, up to and including the hard continuum cutoff motivated above, at  $1.2 T_c$ .

The error estimates for fit parameters of the  $1.2 T_c$  dataset are noticeably higher than for the  $1.1 T_c$  dataset. This is also reflected in the lower  $\chi/\text{d.o.f}$  obtained in these fits in comparison to  $1.1 T_c$ . While the errors between both correlators are similar, see fig. 5.6, the number of points in the  $1.2 T_c$  correlator that enters into the fit is decisively lower. A more precise determination of the correlator, as it was performed for  $1.4 T_c$ , might thus be worthwhile.

The current results do not allow to find a clear temperature dependence for the dilepton rate or the electrical conductivity in the range of  $1.1 T_c$  to  $1.4 T_c$ . For example, both a linear dependence as well as no temperature dependence at all is compatible with the current data within the systematic errors. An illustrating plot is provided by fig. 5.19 in the conclusion of this chapter, together with a short comparison to other current studies.

## 5 Thermal dilepton rates

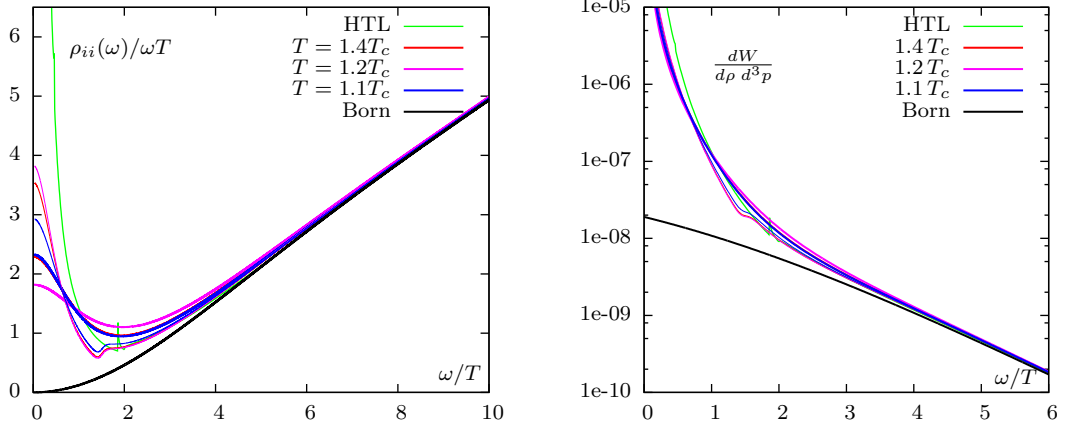


Figure 5.13: Spectral functions obtained by fitting eq. (5.19) to data (left) and dilepton rates (right) calculated by eq. (5.1) from the spectral functions. The thin lines represent the spectral function obtained with systematic error estimates as laid out in section 5.7. The free spectral function (Born) is given in eq. (5.6), the HTL results follow [62].

$\omega_0$	$\Delta_\omega$	$(1 + \kappa)/\chi_q$	$2c_{\text{BW}}/\Gamma$	$\Gamma$	$\frac{2}{3}\chi_q \frac{c_{\text{BW}}}{\Gamma}$	$\chi/\text{d.o.f}$	Data
—	—	1.216(5)	1.353(23)	2.058(85)	0.387(7)	0.52	RS
		1.215(3)	1.328(12)	2.110(34)	0.380(4)	0.65	ST
0.0	0.5	1.217(5)	1.399(20)	1.963(74)	0.401(6)	0.97	RS
		1.218(5)	1.420(19)	1.923(69)	0.406(6)	1.24	RS
		1.219(4)	1.497(15)	1.783(57)	0.429(5)	2.71	RS
		1.219(4)	1.595(8)	1.643(16)	0.456(3)	2.81	ST
		1.222(4)	1.609(12)	1.607(45)	0.461(4)	6.99	RS
1.5	0.1	1.222(4)	1.705(11)	1.506(39)	0.488(3)	4.71	RS
	0.1	1.213(2)	1.675(7)	1.528(14)	0.479(3)	5.50	ST
	0.25	1.222(4)	1.728(11)	1.481(38)	0.495(3)	5.37	RS
	0.5	1.222(4)	1.632(12)	1.572(43)	0.467(4)	8.27	RS
1.75	0.5	1.206(4)	2.139(8)	1.247(26)	0.612(2)	2.21	RS

Table 5.5: Results for fits of eqs. (5.7) and (5.19) to data, at  $1.1 T_c$ . Values  $\omega_0$  and  $\Delta_\omega$  in eq. (5.19) are motivated in the discussion of systematic errors.  $\frac{2}{3}\chi_q \frac{c_{\text{BW}}}{\Gamma}$  relates to the electrical conductivity as given in eq. (5.8). Columns 3 to 5 directly relate to fit variables, see eq. (5.12) and the discussion there. Abbreviations in the column *Data* denote the dataset used in the fit, where RS is the dataset with resampling error estimates, ST the dataset with standard errors, see section 5.5.3. Correlator data points with  $\tau T \geq 0.1875$  enter into the fit.

$\omega_0$	$\Delta_\omega$	$(1 + \kappa)/\chi_q$	$2c_{\text{BW}}/\Gamma$	$\Gamma$	$\frac{2}{3}\chi_q \frac{c_{\text{BW}}}{\Gamma}$	$\chi/\text{d.o.f}$	Data
–	–	1.166(5)	1.010(118)	2.947(347)	0.303(40)	0.11	RS
		1.165(3)	1.056(104)	2.807(386)	0.316(31)	5.56	ST
0.0		1.160(3)	1.049(173)	2.809(636)	0.315(57)	0.44	RS
0.5		1.159(5)	1.024(111)	2.904(405)	0.307(37)	0.23	RS
0.75	0.5	1.163(11)	1.159(137)	2.486(516)	0.348(45)	0.91	RS
1.0		1.166(9)	1.260(49)	2.212(190)	0.378(16)	0.04	RS
1.0		1.164(1)	1.143(12)	2.521(43)	0.343(4)	3.94	ST
1.5	0.1	1.176(7)	2.129(8)	1.152(35)	0.639(2)	0.74	RS
	0.1	1.174(1)	1.792(8)	1.398(3)	0.537(2)	10.34	ST
	0.25	1.170(7)	1.822(11)	1.404(48)	0.547(3)	0.08	RS
	0.5	1.163(8)	1.586(17)	1.683(69)	0.476(5)	0.22	RS

 Table 5.6: Results for fits of eqs. (5.7) and (5.19) to data, at  $1.2 T_c$ , legend see table 5.5.

Concerning the large  $\chi/\text{d.o.f.}$  of the data sets with standard error estimates, compare the errors given in fig. 5.6. Correlator data points with  $\tau T \geq 0.25$  enter into the fit.

### 5.7.3 Fit without thermal moments

The thermal moment were introduced as a constraint to the fit, making it more sensible to the low  $\omega$  region of interest for the electrical conductivity. As an additional crosscheck, the fits of the  $1.1 T_c$  dataset were also performed without this restriction.

The fit range for the  $1.1 T_c$  correlator has been set to  $\tau T \geq 0.1875$ , which leaves 20 points from  $T^2 \cdot G_{ii}(n_t)/\chi_q \cdot G_V^{\text{free}}(n_t)$  to enter into the fit. The fit converges without problems and the result is well compatible within errors to the one obtained with thermal moments, as the electrical conductivity is found as  $\sigma(T)/(TC_{\text{em}}) = 0.345(65)$ . The results are shown in fig. 5.14, the large error of the electrical conductivity is linked to the missing constraint through the thermal moment.

### 5.7.4 Modified ansatz for the spectral function

An analysis by Operator Product Expansion [79] of the ansatz eq. (5.7) suggests a different high frequency  $\omega \rightarrow \infty$  fall-off of the transport contribution. This motivated a modification of eq. (5.7)

$$\rho_{ii}^{\text{interac.}}(\omega) = \chi_q c_{\text{BW}} \frac{\tanh(\omega)\Gamma}{\omega^2 + (\Gamma/2)^2} + (1 + \kappa) \frac{3}{2\pi} \omega^2 \tanh(\omega/4T). \quad (5.20)$$

where  $\tanh(\omega)$  yields a  $\frac{1}{\omega^2}$  falloff for  $\omega \rightarrow \infty$ .

This ansatz is now used to study the systematic effect. The results, given in fig. 5.15, show only a minimal influence, the electrical conductivity is found as  $\sigma(T)/(TC_{\text{em}}) = 0.350(80)$  and thus well compatible with the main results.

## 5 Thermal dilepton rates

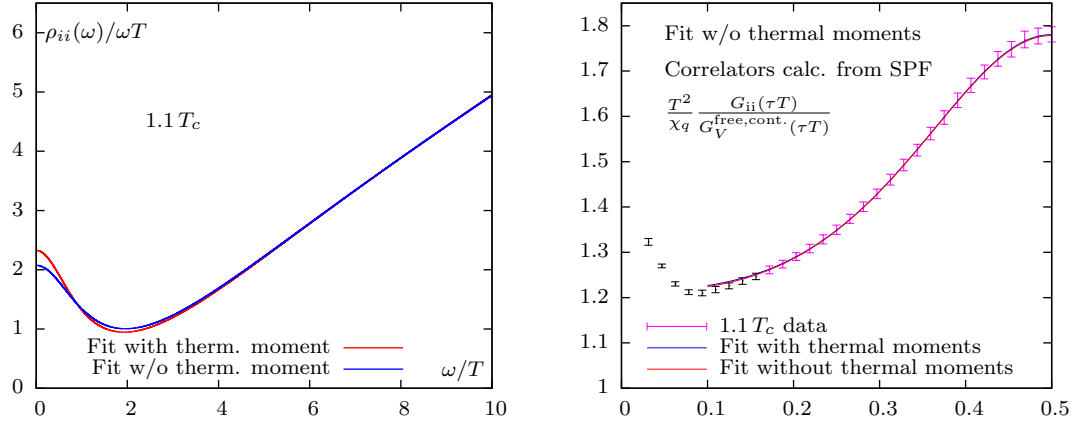


Figure 5.14: Fit of the spectral function with and without the additional constraint through the thermal moments (left), at  $1.1 T_c$ . The fit without thermal moments converges well. The correlator calculated from the spectral function (right) matches the input data. Within errors, the electrical conductivities are compatible.

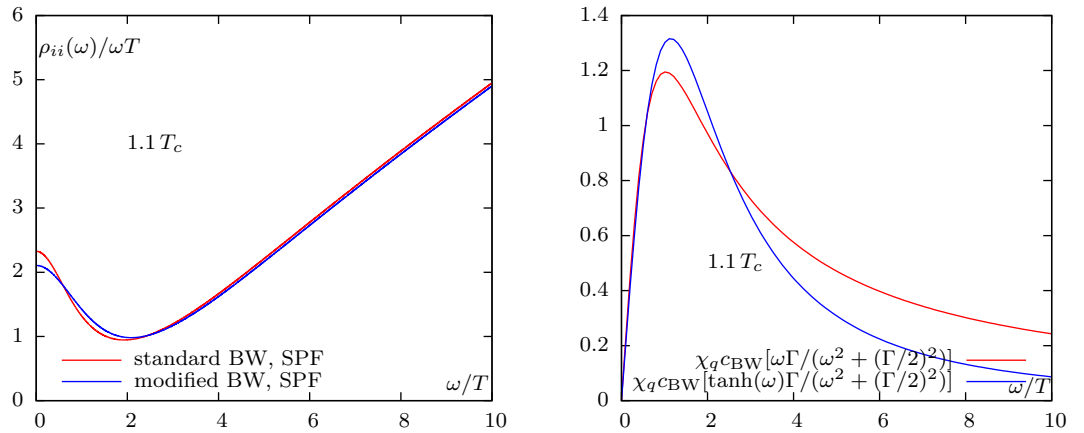


Figure 5.15: Fit of the spectral function with standard and modified Breit-Wigner contribution (left) and a comparison of the standard and the modified Breit-Wigner contribution (right), fitted to  $1.1 T_c$  data, comparing eq. (5.7) with the modified ansatz eq. (5.20). Within errors, the electrical conductivities obtained are compatible.

## 5.8 Continuum extrapolated correlators at finite momenta

The dilepton rates and the electrical conductivity are extracted from the spectral function at vanishing momentum  $\vec{p} = 0$ , corresponding to the vector correlator  $G_V(\tau T, \vec{p}) = 0$ .

Finite momenta  $G_V(\tau T, \vec{p}) \neq 0$  are also accessible to lattice calculation, see eq. (1.45). The vector correlator and the corresponding spectral function split into a longitudinal part  $V_L$  and a transversal part  $V_T$ . The transversal component of the spectral function  $\rho_T$  is related to the photon rate

$$\omega \frac{dR_\gamma}{d^3p} \sim \frac{\rho_T(\omega = |\vec{p}|, T)}{\exp(\omega/T) - 1}. \quad (5.21)$$

and thus extracting  $\rho_T$  from lattice calculations would be rewarding.

### 5.8.1 A momentum-dependent spectral function

It is much harder to motivate a parametrized ansatz for a momentum dependent spectral function  $\rho_L$  or  $\rho_V$  than it is for vanishing momentum, and such an ansatz would be necessary to follow a similar fit procedure as used for the dilepton analysis with  $\rho_V(\omega, \vec{p} = 0)$ . A Bayesian analysis on the continuum extrapolated finite momentum correlators might provide first insights.

Also, to extract photon rates, eq. (5.21) shows that the spectral function has to be known at one point,  $\omega = |\vec{p}|$ . Reproducing one point in the spectral function with high precision might require additional input extracted from the correlator prior to a fit or a Bayesian analysis, as spectral functions and correlators for finite momenta are linked through the same transformation eq. (5.3) as their zero momentum counterparts. However, a constraint similar to the thermal moments, which are used to increase precision at  $\omega = 0$  for spectral function at vanishing momentum, has not yet been found.

While finding an ansatz for the momentum-dependent spectral function proves difficult, continuum-extrapolated momentum-dependent correlators –that are an essential first step in the analysis– have successfully been calculated in the course of this work.

### 5.8.2 Finite momentum correlators

A discrete set of momenta  $\vec{p}$  in  $G_V(\tau T, \vec{p})$  is accessible on the lattice.  $\vec{p}$  is given by

$$\vec{p}/T = 2\pi \cdot \vec{k} \cdot \frac{N_\tau}{N_\sigma} \quad (5.22)$$

where  $\vec{k}$  is a vector of integer numbers.

The longitudinal contributions are given by  $\vec{k}$ -vectors with only one integer component different from zero, for example  $\vec{k} = (k_x, 0, 0, 0)$  when choosing to set  $V_L$  as  $V_x$ , corresponding to  $\rho_{11}$  and thus the vector channel linked to the  $\gamma_1$  matrix.

For the transversal contribution, two components in  $\vec{k}$  may be different from zero. Again as an example, choosing to evaluate  $V_T$  as  $V_z$  –corresponding to  $\rho_{33}$  and thus

$k_y$	$k_x = 0$	1	2	3	4
0	0.0000	2.0944	4.1888	6.2832	8.3776
1	–	2.9619	4.6832	6.6231	8.6354
2	–	–	5.9238	7.5514	9.3664
3	–	–	–	8.8858	10.4720
4	–	–	–	–	11.8477

Table 5.7: Momenta  $|p/T| = |\vec{k}| \cdot 2\pi \cdot N_\tau/N_\sigma$  accessible on a  $N_\sigma/N_\tau = 3$ . Choosing to evaluate  $V_T$  as  $V_z$  along the  $z$ -axes, the purely transversal momenta are obtained by keeping  $k_z = 0$  and varying  $k_x$  and  $k_z$ . Evaluating  $V_L$  as  $V_x$  along the  $x$ -axes, the purely longitudinal momenta are found by setting  $k_y = 0$  and  $k_z = 0$  while varying  $k_x$ , so they can be read off the first row of the table. Of course, other permutations of  $x, y, z$  are possible, the selection here is merely by convention.

the  $\gamma_3$  vector channel— $\vec{k}$  takes the form  $\vec{k} = (k_x, k_y, 0, 0)$ . The absolute values for the momentum here are  $|\vec{k}| = \sqrt{k_x^2 + k_y^2}$ , so non-integer momenta  $|\vec{k}|$  are accessible for the transversal, but not for the longitudinal channel.

For both examples,  $V_L$  as  $V_x$  and  $V_T$  as  $V_z$  are chosen by convention. Because of the rotational invariance, permutations of  $x, y, z$  yield equivalent momenta. In table 5.7 a summary of possible momenta for a  $N_\sigma/N_\tau = 3$  lattice can be found.

### 5.8.3 Continuum extrapolation at non-vanishing momentum

A fixed aspect ratio of  $N_\sigma/N_\tau = 3$  has been set for all three lattice spacings in the setup for the new datasets at  $1.1 T_c$  and  $1.2 T_c$ . This allows to perform a continuum extrapolation following eq. (5.10) in the same way as for correlators with vanishing momentum.

Though finite momentum correlators are available for  $1.4 T_c$ , their aspect ratios differ, so currently no continuum extrapolation can be performed at that temperature. A new set of correlators with  $N_\tau = 24, 36, 48$ , otherwise following table 5.1, would have to be recalculated to allow for this extrapolation.

Results of the extrapolation at  $|\vec{k}| = 2$  for both the longitudinal and the transversal correlator ratios are shown in fig. 5.17. A summary of only the continuum extrapolated results at different momenta is given in fig. 5.18.

The vector correlators with longitudinal momenta do not show a noticeable dependence on their momentum. The vector correlator is however influence by transversal momenta, where higher momenta  $\vec{k}$  cause a steeper fall-off of the ratio  $T^2 \cdot G_V(\tau T, \vec{p})/\chi_q \cdot G_V^{\text{free}}(\tau T)$  towards rising  $\tau T$ .

This behaviour can be qualitatively interpreted in the context of [78], where the transversal and longitudinal vector spectral functions were calculated for small  $\omega$  and small, non-vanishing momenta, in a leading order log Boltzmann Approximation. In

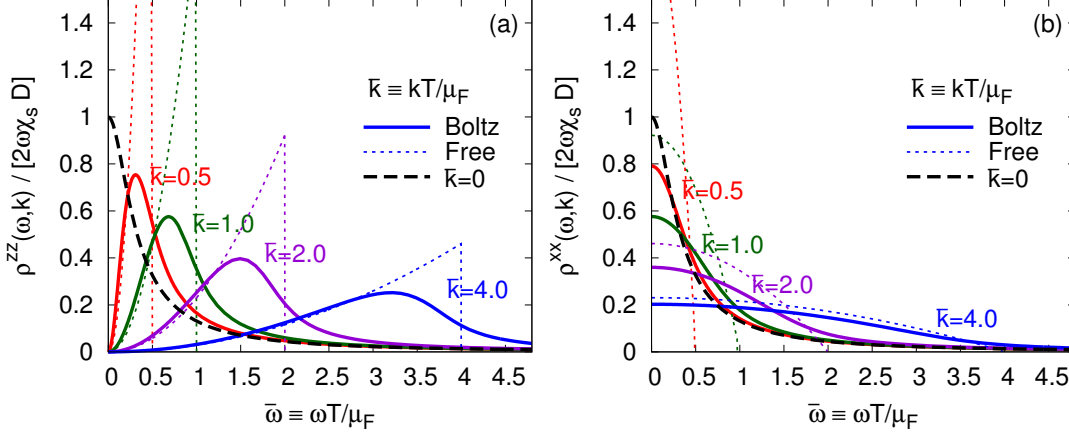


Figure 5.16: Leading order log Boltzmann calculation[78] of the finite momentum longitudinal (left) and transversal (right) vector spectral functions. The dotted lines denote the free spectral functions at the same momenta, highlighting the deviations between free and interacting spectral functions.

fig. 5.16 the obtained longitudinal and transversal spectral functions are shown for different momenta, together with dotted lines for the corresponding free spectral functions. The transversal spectral function is found to be finite and constant in  $\rho_T(\omega)/\omega$  for  $\omega \rightarrow 0$ , while the longitudinal spectral function  $\rho_L(\omega)/\omega$  becomes zero for  $\omega \rightarrow 0$ .

This relates to the observed behaviour of the correlators, as for the transversal part, free and interacting spectral functions deviate in the region of  $\omega \rightarrow 0$ . This region relates to large separations  $\tau T \rightarrow 0.5$  in the correlator, where also a deviation from the free correlator is observed. For the longitudinal part, the spectral functions deviate at larger values of  $\omega$ , but are compatible at  $\omega \rightarrow 0$ . This agrees with the observed behaviour of the longitudinal correlator, which shows no momentum dependence for  $\tau T \rightarrow 0.5$ .

This behaviour may contradict the findings in [80], where a non-zero intercept was found for both polarizations. A detailed study of the spectral function, based on the continuum extrapolated correlators at non-zero momentum, may clarify this in the future.

## 5.9 Conclusion

A systematic study of the temperature dependence was planned and set up: Calculations have been carried out at three temperatures above the phase transition,  $1.1 T_c$  and  $1.2 T_c$ , complemented by  $1.4 T_c$  from the preceding study [7]. At each temperature a set of three lattice spacings, see tables 5.1 and 5.2, allows for a continuum extrapolation. At  $1.1 T_c$  and  $1.2 T_c$  a constant aspect ratio at each lattice spacing enables this extrapolation also for finite momenta, at  $1.4 T_c$  a set of configurations matching these parameters is available.

Continuum extrapolations have been performed on a ratio of interacting to free lattice

## 5 Thermal dilepton rates

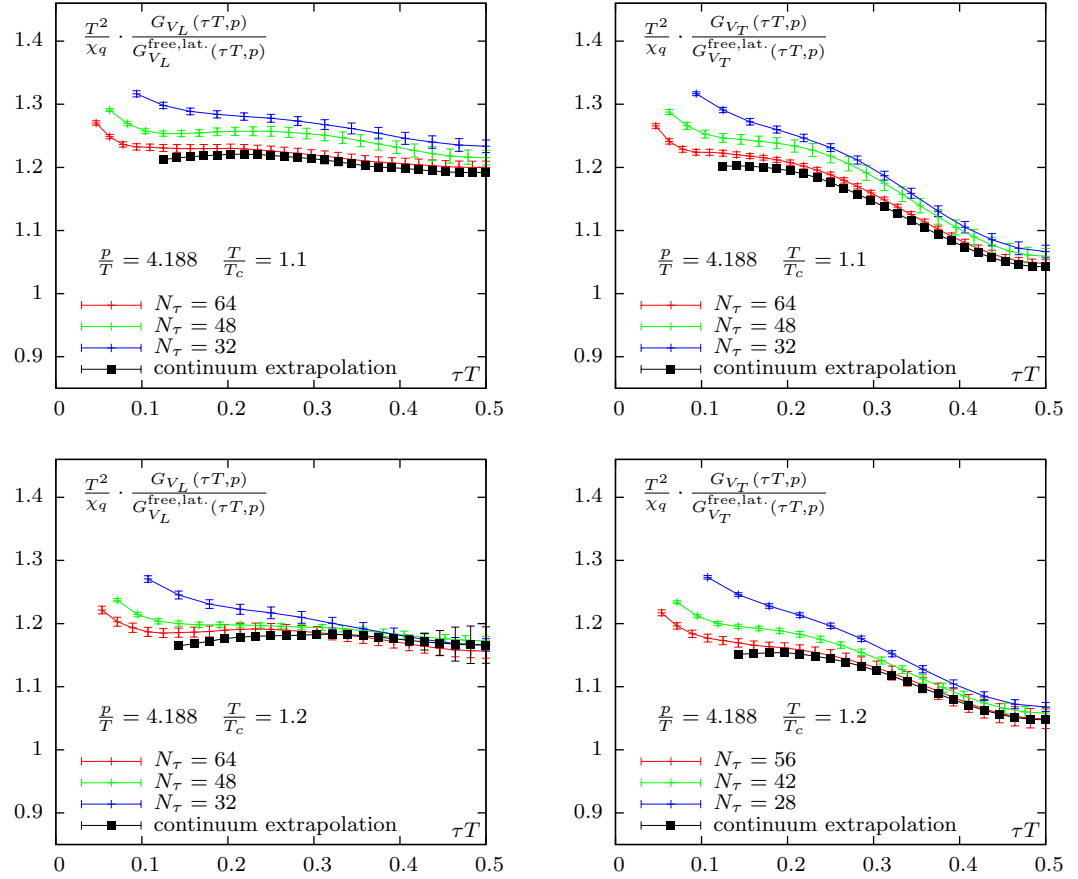


Figure 5.17: Longitudinal ( $V_L$ , left) and transversal ( $V_T$ , right) vector correlators at non-vanishing momentum  $|\vec{p}| = 4.188$  at  $1.1 T_c$  (upper row) and  $1.2 T_c$  (lower row). Results are on finite lattices (red, green, blue) and extrapolated to the continuum (black) via eq. (5.10).

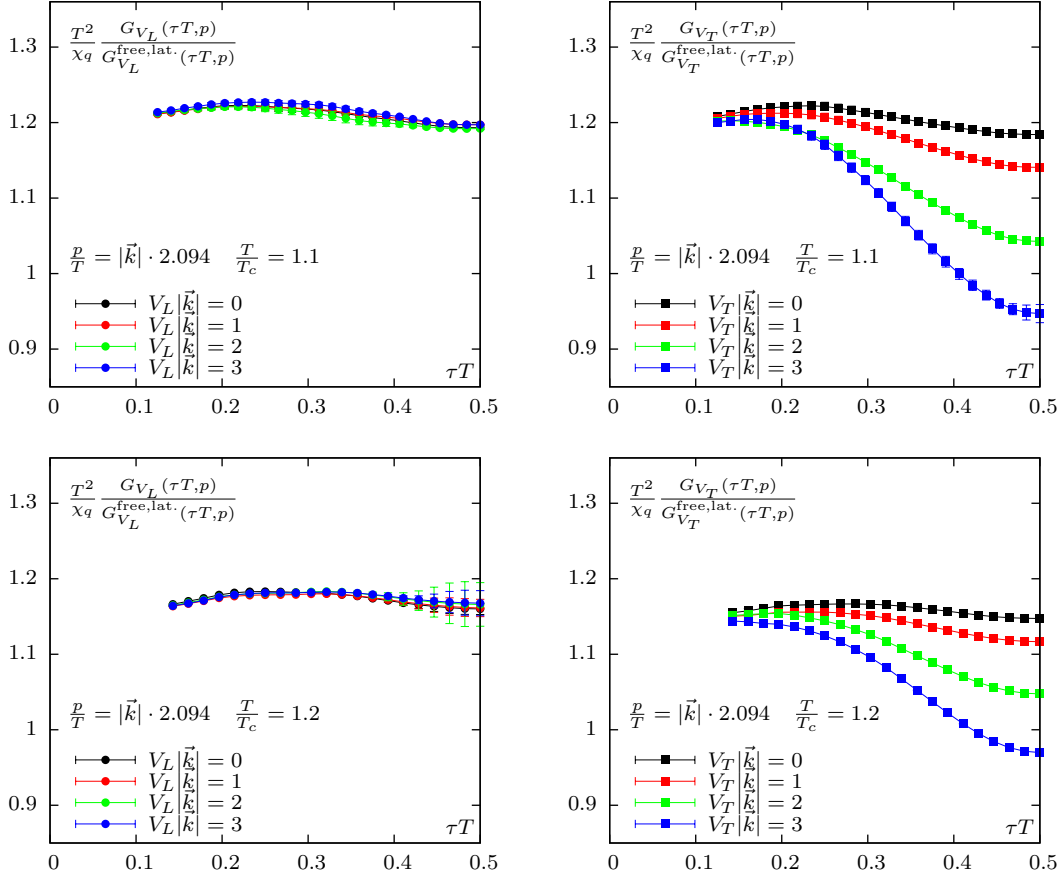


Figure 5.18: Continuum extrapolations for different momenta  $p/T = |\vec{k}| \cdot 2.094$  with  $|\vec{k}| = 0, 1, 2, 3$  of the longitudinal ( $V_L$ , left) and transversal ( $V_T$ , right) vector correlation function, at  $1.1 T_c$  (upper row) and  $1.2 T_c$  (lower row).

## 5 Thermal dilepton rates

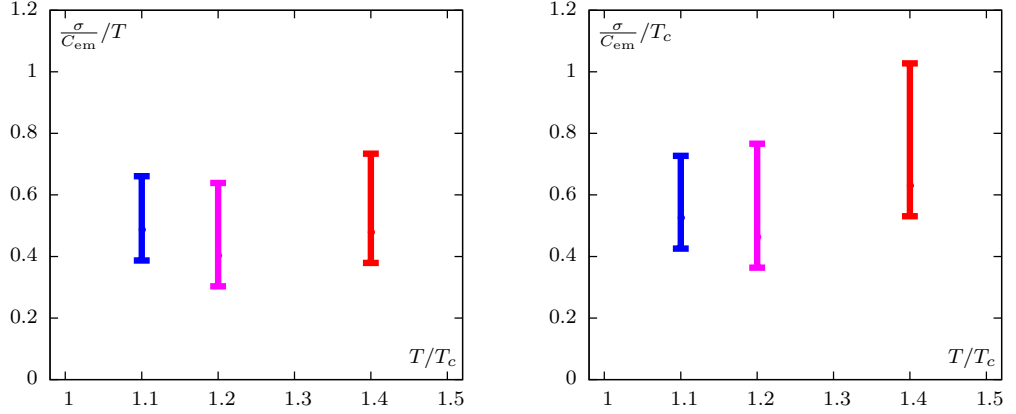


Figure 5.19: Electrical conductivity for temperatures  $1.1 T_c$ ,  $1.2 T_c$  and  $1.4 T_c$ , with systematic error estimates as laid out in section 5.6.2, with a maximal  $\omega_0 = 1.5$  and  $\Delta_\omega = 0.1$ , see also tables 5.5 and 5.6. To compare the temperature dependence, results are given in units of temperature  $T$  (left) and in units of the critical temperature  $T_c$  (right).

correlators normalized by the quark number susceptibility as  $T^2 \cdot G_{ii}(\tau T) / \chi_q \cdot G_V^{\text{free}}(\tau T)$ . The ratios are smooth so they allow for a cubic spline interpolation on the coarser lattices. The continuum extrapolation is well behaved and removes lattice cutoff effects down to distances  $\tau T = 0.125$  at  $1.1 T_c$  and  $\tau T = 0.142$  at  $1.2 T_c$ .

Spectral functions have been extracted successfully from the continuum extrapolated correlators at all three temperatures by using a phenomenologically motivated ansatz. This rather simple ansatz, consisting of a Breit-Wigner peak and a continuum contribution, see eq. (5.7), is found to provide a good descriptions of the data set at all three temperatures.

A systematic error analysis was performed via a parametrized modification of the ansatz, by truncating the continuum contributions, see eq. (5.19). It is found that an increasing continuum cutoff can not be fully compensated by an enhanced Breit-Wigner peak, thus the truncated ansatz yields an inferior description of the data set. This allows to find an upper limit for the Breit-Wigner contribution.

The spectral function is linked to the dilepton rate, which thus can be calculated for all three temperatures. A summarizing plot of the spectral functions and associated dilepton rates is provided in fig. 5.13.

In the low frequency limit, the spectral function also gives access to the electrical conductivity as an important transport coefficient. With the systematic error estimates in place, lower and upper bounds for the electrical conductivity have been calculated.

Within these limits, the conductivity shows no clear temperature dependence, see fig. 5.19. The systematic error analysis – as currently employed – implies a low limit for the electrical conductivity at each temperature. The upper limit is influence by

the choice of cut-off parameter. A consistent choice of these parameters for all three temperatures has been motivated.

At present, two current studies are published that allow for a direct comparison with the results for the electrical conductivity obtained in this work: A MEM analysis of calculation with dynamical clover fermions, on anisotropic lattices [68] and studying multiple temperatures, yields somewhat lower results for the electrical conductivity. Another analysis [69], also employing dynamical Wilson fermions, but using a modified version of the spectral function ansatz, yields a result at  $\approx 1.4 T_c$  that is compatible with this study. In an older study [70], where the electrical conductivity is obtained from a MEM analysis of quenched staggered fermions, a value of  $\sigma(T)/T = 0.4(1)$  is found, which is also in agreement with this work.

As an outlook, the continuum extrapolations for correlators at finite momenta  $\vec{p} \neq 0$  were successfully carried out. The results are promising and can hopefully serve as input to future studies of, for example, the photon rate in the quark-gluon-plasma.

Results obtained for the  $1.2 T_c$  dataset currently do not reach the precision of the  $1.1 T_c$  and  $1.4 T_c$  dataset. It is worthwhile to determine if the dataset should be extended, so the results for the electrical conductivity become more precise. In this case, they might allow for determination of the temperature dependence.



## 6 Conclusion

This general conclusion complements the introduction given in the front matter of this thesis. A short conclusion, highlighting the main results of each of the four topics discussed in this thesis is given here, while more in-depth discussions of the results and more specific conclusions are given in the (self-contained) chapters corresponding to each topic.

### 6.1 Parallel Lattice Code

In the course of this work, a software suite for lattice QCD calculations was developed. The code is designed to be modular and layered, allowing to easily tune, enhance and exchange its functionality.

The code is in successful productive use for multiple research efforts. Available functionality includes heatbath and overrelaxation code for pure gauge measurements and the generation of quenched configurations, standard and clover improved Wilson fermion actions and accompanying inverters, measurement routines for diffusion coefficients and Wilson loops, and an interface to specific routines of the QUDA framework.

The code is under constant development. Future plans include the implementation of interfaces to external lattice QCD libraries, such as a full interface to the QUDA framework and the SCIDAC suite. This will allow for speedups on more specialized supercomputing machines. Also, measurement routines for more observables and advanced inverters, like multi-grid techniques, can be implemented.

### 6.2 Scale setting

The precise determination of the lattice spacing and the critical temperature  $T_c$  is an important requisite for quenched lattice QCD studies.

New results for couplings  $\beta < 7$  were obtained for both the lattice spacing and the critical temperature, with

$$T_c \cdot r_0 = 0.7497(1)$$

found as a central result.

Especially for the critical temperature, these new datasets greatly improve the precision over previously used data, allowing for more precise extrapolation. Updated values for lattice spacings and temperatures  $T/T_c$  for all relevant couplings have been calculated and tabulated.

Quark masses for the clover-improved Wilson fermion action were also retuned and recalculated, updating older results and ensuring more constant quark masses among all lattice sizes.

## 6 Conclusion

This study will be extended with further values  $\beta_c(N_\tau)$  and  $[r_0/a](\beta)$ , or a similar observable more suited for  $\beta > 7$ . This will provide a check and further refinement of the extrapolations.

### 6.3 Meson screening masses

When calculating meson screening masses on finite lattices, differences in the results between the clover-improved Wilson and the standard staggered fermion actions are found. This study helps answering the question whether these differences vanish if appropriate thermodynamic and continuum limits are taken.

At two temperatures ( $1.5 T_c$  and  $3.0 T_c$ ) and for four different meson channels, the (pseudo)scalar and the (axial)vector, it is found that their screening masses become compatible if and only if both limits are carried out correctly. This agreement is easier to find at  $3.0 T_c$  than at  $1.5 T_c$ , where high statistics and an involved analysis procedure had to be used to obtain conclusive results.

It is also found that the pseudo-scalar and the scalar degenerate at both temperatures, as well as the vector and the axial-vector. This is expected for the deconfined phase of QCD. In the free theory limit, all four masses degenerate, which is neither observed for  $1.5 T_c$  nor for  $3.0 T_c$ . At  $3.0 T_c$ , the (axial)vector mass reaches the free theory limit of  $2\pi T$ , but it is not clear if the mass will rise further with increasing temperature and approach  $2\pi T$  from above, as suggested by HTL predictions.

The insights gained into extracting screening ground state masses and their thermodynamic and continuum limits are hopefully valuable for other studies, as currently the first simulations employing dynamical quarks reach lattice sizes where such an analysis might be feasible.

### 6.4 Thermal dilepton rates

The extraction of vector meson spectral functions from the vector current correlation functions on the lattice is a long-standing research effort.

An ansatz-based approach, developed and documented in the course of [7], was used to set up a systematic temperature dependence study of thermal dilepton rates in the deconfined phase near the phase transition.

The temperature of  $1.4 T_c$  from the previous study was complemented with two further temperatures closer to the phase transition,  $1.1 T_c$  and  $1.2 T_c$ . Lattice sizes and coupling were tuned to allow for a controlled continuum extrapolation of zero and finite momentum vector correlation functions.

Continuum extrapolations were carried out successfully at both new temperatures and compensate for the cut-off effects of the obtained correlation functions. This is an important requirement for the spectral function analysis.

Spectral functions and therefore the dilepton rates and the electrical conductivity have been extracted, passing the datasets of all three temperatures through a systematic

error analysis. Parameters for this analysis have been chosen consistently for all three temperatures.

The results put lower and upper boundary on the electrical conductivity in the quark gluon plasma at  $1.1 < T/T_c < 1.4$ , with

$$\frac{1}{C_{\text{em}}} \frac{\sigma}{T} = 0.303(40) \text{ to } 0.734(8)$$

within rather conservative systematic error estimates, see tables 5.5 and 5.6. Within these errors, no clear temperature dependence was found. The results are, for example, compatible with a linear as well as no temperature dependence at all, see fig. 5.19.

These results can directly be compared to three other recent lattice studies. The two most current employ dynamical fermions but lack a continuum extrapolation: A first study[68], using a MEM-based approach and anisotropic lattices, finds electrical conductivities that are somewhat lower and feature a stronger temperature dependence. A second study[69], using Wilson fermions and a modification of the ansatz-based approach, finds a conductivity at  $T/T_c \approx 1.4$  that is well compatible with the result presented here. An older study [70] obtains the electrical conductivity from a MEM analysis of quenched staggered fermions and finds a value of  $\sigma(T)/T = 0.4(1)$ , which is also in agreement with this work.

Lattices with constant aspect ratios at all lattice spacings were used in this study. Thus, continuum extrapolations of finite momentum correlation functions are possible and were successfully obtained for both new temperatures. Eventually, an ansatz for a momentum-dependent vector spectral function, allowing for an analysis analog to the one performed at zero momentum, would be very rewarding. However, finding such an ansatz is a major effort.

Over all, two prospects emerge: A study employing dynamical fermions, where – with advancements in algorithms and computing power – also continuum extrapolations may become feasible, and the study of finite momentum spectral functions, giving access to the photon rate from lattice QCD calculations.



# Bibliography

- [1] M. Gell-Mann, *Symmetries of baryons and mesons*, *Phys.Rev.* **125** (1962) 1067, [DOI: [10.1103/PhysRev.125.1067](https://doi.org/10.1103/PhysRev.125.1067)].
- [2] J. A. Carlson, ed., *The millenium prize problems*. Clay Mathematics Institute, Cambridge, Mass., 2006. Available online at [www.claymath.org/publications/Millennium\\_Problems](http://www.claymath.org/publications/Millennium_Problems).
- [3] D. J. Gross and F. Wilczek, *Ultraviolet behavior of non-abelian gauge theories*, *Phys. Rev. Lett.* **30** (Jun, 1973) 1343, [DOI: [10.1103/PhysRevLett.30.1343](https://doi.org/10.1103/PhysRevLett.30.1343)].
- [4] E. Iancu, *QCD in heavy ion collisions*, [arXiv:1205.0579](https://arxiv.org/abs/1205.0579).
- [5] K. G. Wilson, *Confinement of Quarks*, *Phys.Rev.* **D10** (1974) 2445, [DOI: [10.1103/PhysRevD.10.2445](https://doi.org/10.1103/PhysRevD.10.2445)].
- [6] P. Petreczky, *Lattice QCD at non-zero temperature*, *J.Phys.* **G39** (2012) 093002, [[arXiv:1203.5320](https://arxiv.org/abs/1203.5320)].
- [7] A. Francis, *Thermal dilepton rates from quenched lattice QCD : a study of thermal spectral functions in the continuum limit of quenched lattice QCD, at vanishing and finite momentum*. PhD thesis, Universität Bielefeld, 2011. [[urn:nbn:de:hbz:361-24032911](https://nbn-resolving.org/urn:nbn:de:hbz:361-24032911)].
- [8] O. Kaczmarek, E. Laermann, M. Müller, F. Karsch, H. Ding, et al., *Thermal dilepton rates from quenched lattice QCD*, *PoS ConfinementX* (2012) 185, [[arXiv:1301.7436](https://arxiv.org/abs/1301.7436)].
- [9] O. Kaczmarek and M. Müller, *Temperature dependence of electrical conductivity and dilepton rates from hot quenched lattice QCD*, *PoS LATTICE2013* (2013) [[arXiv:1312.5609](https://arxiv.org/abs/1312.5609)]. Submitted.
- [10] C. Gattringer and C. B. Lang, *Quantum chromodynamics on the lattice. An introductory presentation*. Lecture notes in physics 788. Springer, 2010, [DOI: [10.1007/978-3-642-01850-3](https://doi.org/10.1007/978-3-642-01850-3)].
- [11] H. J. Rothe, *Lattice gauge theories : an introduction*, vol. 74 of *World Scientific lecture notes in physics*. World Scientific, Hackensack, NJ, 3. ed., 2005, [DOI: [10.1142/9789812567826\\_fmatter](https://doi.org/10.1142/9789812567826_fmatter)].
- [12] I. Montvay and G. Münster, *Quantum fields on a lattice*. Cambridge monographs on mathematical physics. Cambridge Univ. Press, Cambridge, 1. paperback ed., 1997, [DOI: [10.1002/phb1.19950510219](https://doi.org/10.1002/phb1.19950510219)].

## Bibliography

- [13] H. B. Nielsen and M. Ninomiya, *Absence of Neutrinos on a Lattice. 1. Proof by Homotopy Theory*, *Nucl.Phys.* **B185** (1981) 20, [DOI: [10.1016/0550-3213\(81\)90361-8](https://doi.org/10.1016/0550-3213(81)90361-8)].
- [14] B. Sheikholeslami and R. Wohlert, *Improved Continuum Limit Lattice Action for QCD with Wilson Fermions*, *Nucl.Phys.* **B259** (1985) 572, [DOI: [10.1016/0550-3213\(85\)90002-1](https://doi.org/10.1016/0550-3213(85)90002-1)].
- [15] M. Luscher, S. Sint, R. Sommer, P. Weisz, and U. Wolff, *Nonperturbative  $O(a)$  improvement of lattice QCD*, *Nucl.Phys.* **B491** (1997) 323, [[hep-lat/9609035](https://arxiv.org/abs/hep-lat/9609035)].
- [16] **CP-PACS Collaboration** Collaboration, S. Aoki et al., *Quenched light hadron spectrum*, *Phys.Rev.Lett.* **84** (2000) 238, [[hep-lat/9904012](https://arxiv.org/abs/hep-lat/9904012)].
- [17] N. Cabibbo and E. Marinari, *A New Method for Updating  $SU(N)$  Matrices in Computer Simulations of Gauge Theories*, *Phys.Lett.* **B119** (1982) 387, [DOI: [10.1016/0370-2693\(82\)90696-7](https://doi.org/10.1016/0370-2693(82)90696-7)].
- [18] A. Kennedy and B. Pendleton, *Improved Heat Bath Method for Monte Carlo Calculations in Lattice Gauge Theories*, *Phys.Lett.* **B156** (1985) 393, [DOI: [10.1016/0370-2693\(85\)91632-6](https://doi.org/10.1016/0370-2693(85)91632-6)].
- [19] S. L. Adler, *An Overrelaxation Method for the Monte Carlo Evaluation of the Partition Function for Multiquadratic Actions*, *Phys.Rev.* **D23** (1981) 2901, [DOI: [10.1103/PhysRevD.23.2901](https://doi.org/10.1103/PhysRevD.23.2901)].
- [20] M. Creutz, *Overrelaxation and Monte Carlo Simulation*, *Phys.Rev.* **D36** (1987) 515, [DOI: [10.1103/PhysRevD.36.515](https://doi.org/10.1103/PhysRevD.36.515)].
- [21] A. Meister, *Numerik linearer Gleichungssysteme : Eine Einführung in moderne Verfahren*. Vieweg+Teubner Verlag / Springer Fachmedien Wiesbaden GmbH, Wiesbaden, 4. ed., 2011, [DOI: [10.1007/978-3-8348-8100-7](https://doi.org/10.1007/978-3-8348-8100-7)].
- [22] H. B. Meyer, *Transport Properties of the Quark-Gluon Plasma: A Lattice QCD Perspective*, *Eur.Phys.J.* **A47** (2011) 86, [[arXiv:1104.3708](https://arxiv.org/abs/1104.3708)].
- [23] M. Clark, R. Babich, K. Barros, R. Brower, and C. Rebbi, *Solving Lattice QCD systems of equations using mixed precision solvers on GPUs*, *Comput.Phys.Commun.* **181** (2010) 1517, [[arXiv:0911.3191](https://arxiv.org/abs/0911.3191)].
- [24] USQCD / SciDac, *Lattice gauge theory software research and development*, 2013. [www.usqcd.org](http://www.usqcd.org).
- [25] Message Passing Interface Forum, University of Tennessee, Knoxville, Tennessee, *MPI: A Message-Passing Interface Standard, Version 3.0*. Available [online](https://www.mpi-forum.org) on the MPI Forum website [www.mpi-forum.org](http://www.mpi-forum.org).

- [26] A. Francis, O. Kaczmarek, M. Laine, M. Müller, T. Neuhaus, et al., *Towards the continuum limit in transport coefficient computations*, *PoS LATTICE2013* (2013) [[arXiv:1311.3759](#)]. Submitted.
- [27] S. Sharma, V. Dick, F. Karsch, E. Laermann, and S. Mukherjee, *Investigation of the  $U_A(1)$  in high temperature QCD on the lattice*, *PoS LATTICE2013* (2013) [[arXiv:1311.3943](#)]. Submitted.
- [28] R. Sommer, *A New way to set the energy scale in lattice gauge theories and its applications to the static force and alpha-s in SU(2) Yang-Mills theory*, *Nucl.Phys.* **B411** (1994) 839, [[hep-lat/9310022](#)].
- [29] S. Durr, Z. Fodor, C. Hoelbling, and T. Kurth, *Precision study of the SU(3) topological susceptibility in the continuum*, *JHEP* **0704** (2007) 55, [[hep-lat/0612021](#)].
- [30] ALPHA Collaboration, M. Guagnelli, R. Sommer, and H. Wittig, *Precision computation of a low-energy reference scale in quenched lattice QCD*, *Nucl.Phys.* **B535** (1998) 389, [[hep-lat/9806005](#)].
- [31] S. Necco and R. Sommer, *The  $N(f) = 0$  heavy quark potential from short to intermediate distances*, *Nucl.Phys.* **B622** (2002) 328, [[hep-lat/0108008](#)].
- [32] B. Beinlich, F. Karsch, E. Laermann, and A. Peikert, *String tension and thermodynamics with tree level and tadpole improved actions*, *Eur.Phys.J.* **C6** (1999) 133, [[hep-lat/9707023](#)].
- [33] S. Necco, *Universality and scaling behavior of RG gauge actions*, *Nucl.Phys.* **B683** (2004) 137, [[hep-lat/0309017](#)].
- [34] H.-T. Ding, *Charmonium correlation and spectral functions in quenched lattice QCD at finite temperature*. PhD thesis, Universität Bielefeld, 2010. [[urn:nbn:de:hbz:361-17732](#)].
- [35] M. Bochicchio, L. Maiani, G. Martinelli, G. C. Rossi, and M. Testa, *Chiral Symmetry on the Lattice with Wilson Fermions*, *Nucl.Phys.* **B262** (1985) 331, [[DOI: 10.1016/0550-3213\(85\)90290-1](#)].
- [36] A. Skouroupathis and H. Panagopoulos, *Two-loop renormalization of vector, axial-vector and tensor fermion bilinears on the lattice*, *Phys.Rev.* **D79** (2009) 094508, [[arXiv:0811.4264](#)].
- [37] ALPHA Collaboration, S. Capitani, M. Luscher, R. Sommer, and H. Wittig, *Nonperturbative quark mass renormalization in quenched lattice QCD*, *Nucl.Phys.* **B544** (1999) 669, [[hep-lat/9810063](#)].
- [38] G. de Divitiis and R. Petronzio, *Nonperturbative renormalization constants on the lattice from flavor nonsinglet Ward identities*, *Phys.Lett.* **B419** (1998) 311, [[hep-lat/9710071](#)].

## Bibliography

- [39] **ALPHA** Collaboration, M. Guagnelli et al., *Nonperturbative results for the coefficients  $b(m)$  and  $b(a) - b(P)$  in  $O(a)$  improved lattice QCD*, *Nucl.Phys.* **B595** (2001) 44, [[hep-lat/0009021](#)].
- [40] K. Chetyrkin, J. H. Kuhn, and M. Steinhauser, *RunDec: A Mathematica package for running and decoupling of the strong coupling and quark masses*, *Comput.Phys.Commun.* **133** (2000) 43, [[hep-ph/0004189](#)].
- [41] G. Kilcup, R. Gupta, and S. R. Sharpe, *Staggered fermion matrix elements using smeared operators*, *Phys.Rev.* **D57** (1998) 1654, [[hep-lat/9707006](#)].
- [42] M. Luscher and P. Weisz, *Two loop relation between the bare lattice coupling and the  $\overline{MS}$  coupling in pure  $SU(N)$  gauge theories*, *Phys.Lett.* **B349** (1995) 165, [[hep-lat/9502001](#)].
- [43] T. R. Klassen, *The (Lattice) QCD potential and coupling: How to accurately interpolate between multiloop QCD and the string picture*, *Phys.Rev.* **D51** (1995) 5130, [[DOI: 10.1103/PhysRevD.51.5130](#)].
- [44] M. Luscher, S. Sint, R. Sommer, and H. Wittig, *Nonperturbative determination of the axial current normalization constant in  $O(a)$  improved lattice QCD*, *Nucl.Phys.* **B491** (1997) 344, [[hep-lat/9611015](#)].
- [45] W. Alberico, A. Beraudo, A. Czerska, P. Czerski, and A. Molinari, *Meson Screening Masses in the Interacting QCD Plasma*, *Nucl.Phys.* **A792** (2007) 152, [[hep-ph/0703298](#)].
- [46] M. Laine and M. Vepsalainen, *Mesonic correlation lengths in high temperature QCD*, *JHEP* **0402** (2004) 004, [[hep-ph/0311268](#)].
- [47] M. Cheng, S. Datta, A. Francis, J. van der Heide, C. Jung, et al., *Meson screening masses from lattice QCD with two light and the strange quark*, *Eur.Phys.J.* **C71** (2011) 1564, [[arXiv:1010.1216](#)].
- [48] S. Gupta and N. Karthik, *Hadronic Screening in Improved Taste*, *Phys.Rev.* **D87** (2013) 094001, [[arXiv:1302.4917](#)].
- [49] M. Fukugita, H. Mino, M. Okawa, G. Parisi, and A. Ukawa, *Finite size effect for hadron masses in lattice QCD*, *Phys.Lett.* **B294** (1992) 380, [[DOI: 10.1016/0370-2693\(92\)91537-J](#)].
- [50] B. Müller, *Investigation of Hot QCD Matter: Theoretical Aspects*, [arXiv:1309.7616](#).
- [51] R. Rapp, *Dilepton Spectroscopy of QCD Matter at Collider Energies*, [arXiv:1304.2309](#).
- [52] K. Eskola, *High-energy nuclear collisions*, [hep-ph/9911350](#).

- [53] R. Rapp, J. Wambach, and H. van Hees, *The Chiral Restoration Transition of QCD and Low Mass Dileptons*, in *Landolt-Börnstein*, vol. I-23, 4-1. Springer-Verlag, 2010. [arXiv:0901.3289](#).
- [54] **PHENIX Collaboration** Collaboration, A. Adare et al., *Enhanced production of direct photons in Au+Au collisions at  $\sqrt{s_{NN}} = 200$  GeV and implications for the initial temperature*, *Phys.Rev.Lett.* **104** (2010) 132301, [[arXiv:0804.4168](#)].
- [55] **PHENIX Collaboration** Collaboration, A. Adare et al., *Detailed measurement of the  $e^+e^-$  pair continuum in  $p + p$  and Au+Au collisions at  $\sqrt{s_{NN}} = 200$  GeV and implications for direct photon production*, *Phys.Rev.* **C81** (2010) 034911, [[arXiv:0912.0244](#)].
- [56] **ALICE Collaboration** Collaboration, M. Wilde, *Measurement of Direct Photons in pp and Pb-Pb Collisions with ALICE*, *Nucl.Phys.A904-905* **2013** (2013) 573c, [[arXiv:1210.5958](#)].
- [57] R. Rapp and J. Wambach, *Chiral symmetry restoration and dileptons in relativistic heavy ion collisions*, *Adv.Nucl.Phys.* **25** (2000) 1, [[hep-ph/9909229](#)].
- [58] G. David, R. Rapp, and Z. Xu, *Electromagnetic Probes at RHIC-II*, *Phys.Rept.* **462** (2008) 176, [[nucl-ex/0611009](#)].
- [59] **STAR Collaboration** Collaboration, F. Geurts, *The STAR Dilepton Physics Program*, *Nucl.Phys.A904-905* **2013** (2013) 217c, [[arXiv:1210.5549](#)].
- [60] U. W. Heinz and R. Snellings, *Collective flow and viscosity in relativistic heavy-ion collisions*, *Annu. Rev. Nucl. Part. Sci.* **63** (2013) 123, [[arXiv:1301.2826](#)].
- [61] C. Gale, S. Jeon, and B. Schenke, *Hydrodynamic Modeling of Heavy-Ion Collisions*, *Int.J.Mod.Phys.* **A28** (2013) 1340011, [[arXiv:1301.5893](#)].
- [62] E. Braaten and R. D. Pisarski, *Soft Amplitudes in Hot Gauge Theories: A General Analysis*, *Nucl.Phys.* **B337** (1990) 569, [[DOI: 10.1016/0550-3213\(90\)90508-B](#)].
- [63] S. Mogliacci, J. O. Andersen, M. Strickland, N. Su, and A. Vuorinen, *Equation of State of hot and dense QCD: Resummed perturbation theory confronts lattice data*, [arXiv:1307.8098](#).
- [64] G. Aarts and J. M. Martinez Resco, *Transport coefficients, spectral functions and the lattice*, *JHEP* **0204** (2002) 053, [[hep-ph/0203177](#)].
- [65] F. Karsch, E. Laermann, P. Petreczky, S. Stickan, and I. Wetzorke, *A Lattice calculation of thermal dilepton rates*, *Phys.Lett.* **B530** (2002) 147, [[hep-lat/0110208](#)].
- [66] S. Gupta, *The Electrical conductivity and soft photon emissivity of the QCD plasma*, *Phys.Lett.* **B597** (2004) 57, [[hep-lat/0301006](#)].

## Bibliography

- [67] H.-T. Ding, A. Francis, O. Kaczmarek, F. Karsch, E. Laermann, et al., *Thermal dilepton rate and electrical conductivity: An analysis of vector current correlation functions in quenched lattice QCD*, *Phys.Rev.* **D83** (2011) 034504, [[arXiv:1012.4963](#)].
- [68] A. Amato, G. Aarts, C. Allton, P. Giudice, S. Hands, et al., *Electrical conductivity of the quark-gluon plasma across the deconfinement transition*, [arXiv:1307.6763](#).
- [69] B. B. Brandt, A. Francis, H. B. Meyer, and H. Wittig, *Thermal Correlators in the  $\rho$  channel of two-flavor QCD*, [arXiv:1212.4200](#).
- [70] G. Aarts, C. Allton, J. Foley, S. Hands, and S. Kim, *Spectral functions at small energies and the electrical conductivity in hot, quenched lattice QCD*, *Phys.Rev.Lett.* **99** (2007) 022002, [[hep-lat/0703008](#)].
- [71] L. P. Kadanoff and P. C. Martin, *Hydrodynamic equations and correlation functions*, *Annals of Physics* **24** (Oct., 1963) 419, [[DOI: 10.1016/0003-4916\(63\)90078-2](#)].
- [72] M. Asakawa, T. Hatsuda, and Y. Nakahara, *Maximum entropy analysis of the spectral functions in lattice QCD*, *Prog.Part.Nucl.Phys.* **46** (2001) 459, [[hep-lat/0011040](#)].
- [73] Y. Burnier and A. Rothkopf, *A novel Bayesian approach to spectral function reconstruction*, [arXiv:1307.6106](#).
- [74] A. Francis and O. Kaczmarek, *On the temperature dependence of the electrical conductivity in hot quenched lattice QCD*, *Prog.Part.Nucl.Phys.* **67** (2012) 212, [[arXiv:1112.4802](#)].
- [75] B. B. Brandt, A. Francis, H. B. Meyer, and H. Wittig, *Two-flavour lattice QCD correlation functions in the deconfinement transition region*, *PoS ConfinementX* (2012) 186, [[arXiv:1302.0675](#)].
- [76] G. D. Moore and J.-M. Robert, *Dileptons, spectral weights, and conductivity in the quark-gluon plasma*, [hep-ph/0607172](#).
- [77] P. Petreczky and D. Teaney, *Heavy quark diffusion from the lattice*, *Phys.Rev.* **D73** (2006) 014508, [[hep-ph/0507318](#)].
- [78] J. Hong and D. Teaney, *Spectral densities for hot QCD plasmas in a leading log approximation*, *Phys.Rev.* **C82** (2010) 044908, [[arXiv:1003.0699](#)].
- [79] Y. Burnier and M. Laine, *Towards flavour diffusion coefficient and electrical conductivity without ultraviolet contamination*, *Eur.Phys.J.* **C72** (2012) 1902, [[arXiv:1201.1994](#)].
- [80] G. Aarts, C. Allton, S. Hands, J. Foley, and S. Kim, *Polarised correlators at finite temperature*, *PoS LATTICE2010* (2010) 166, [[arXiv:1007.4897](#)].

# Acknowledgements

I wish to thank Olaf Kaczmarek, Frithjof Karsch and Edwin Laermann for the supervision of this thesis and the constant support throughout my years in Bielefeld.

I want to thank Anthony for all the long and fruitful conversations, providing me with a deeper understanding of thermal dilepton rates.

The Parallel Lattice Code would not be in its current state without the help of Markus and Viktor, who joined the long discussions and extensive planning of software development.

I thank Christian, Florian, Hiroshi, Matthias, Nirupam, Sayantan and all other members of the high energy physics workgroup, for providing an enjoyable environment for scientific discourse.

This work would not have been possible without the constant support throughout the years from Jana, Johanna, Lena, Carolin, Andreas, Andreas, and all other friends.

I thank my parents for enabling me to follow this path in my life.



# Eigenständigkeitserklärung Declaration of Originality

Zur Dissertation mit dem Titel

**Meson correlations and spectral functions in the deconfined phase  
A systematic analysis in lattice QCD**

Hiermit erkläre ich die vorliegende Arbeit selbständig und ohne fremde Hilfe verfasst und nur die angegebene Literatur und Hilfsmittel verwendet zu haben.

---

Marcel Müller